

# Geodätisch-geophysikalische Arbeiten in der Schweiz

(Fortsetzung der Publikationsreihe  
«Astronomisch-geodätische Arbeiten in der Schweiz»)

herausgegeben von der

Schweizerischen Geodätischen Kommission  
(Organ der Akademie der Naturwissenschaften Schweiz)

**Neunzigster Band**  
**Volume 90**

**Improvement of the  
Kinematic Model of  
Switzerland (Swiss 4D II)**

Arturo Villiger

2014

Adresse der Schweizerischen Geodätischen Kommission:

Institut für Geodäsie und Photogrammetrie  
Eidg. Technische Hochschule Zürich  
ETH Zürich  
8093 Zürich  
Switzerland

Internet: <http://www.sgc.ethz.ch>

ISBN 978-3-908440-36-9

Redaktion des 90. Bandes:  
Dr. A. Villiger, J. Müller-Gantenbein, Prof. A. Geiger  
Druck: Print-Atelier ADAG, Zürich

## VORWORT

Die seismische Gefährdung in der Schweiz ist verglichen mit aktiven Erdbebenregionen wie Griechenland klein. Nichts desto trotz können grössere Erdbeben auch in der Schweiz nicht ausgeschlossen werden. In den Regionen Wallis und Basel traten auch schon Erdbeben mit einer Magnitude über sechs auf.

Die Entwicklung der geodätischen Mess- und Satellitentechnologie stellt den Forschern Werkzeuge zur Verfügung, die es erlauben, selbst kleine zeitliche Änderungen von geospezifischen Parametern festzustellen; so lassen sich Kontinentalverschiebungen, Krustendeformationen und der Strainaufbau mit geodätischen Mitteln nachweisen. Diese Nachweise allerdings sind im Bereich der Schweiz nicht ohne weiteres zu erbringen, da die kleinen Bewegungen auch zu sehr kleinen jährlichen Verzerrungsraten führen. Sie liegen im Bereich von maximal 25 nstrain pro Jahr oder 2.5 mm pro Jahr auf einer Basislinie von 100 Kilometern.

Seit etlichen Jahren führt die swisstopo schweizweite GNSS Messkampagnen auf ihrem 1. Ordnungsnetz durch. Die daraus resultierenden Koordinatenzeitreihen dienen neben den langjährigen Nivellement-Zeitreihen als Datengrundlage für die Schätzung eines kohärenten kinematischen Verschiebungs- und Verzerrungsfeldes innerhalb der Schweiz.

Dank der Weiterentwicklung der am Institut für Geodäsie und Fotogrammetrie ausgearbeiteten Methode der ‚Adaptive Least-Square Collocation (ALSC)‘ und der Berücksichtigung eines physikalischen Krustenmodells konnten erstmals GPS (Lage)- und Nivellement Daten (Hebung) gemeinsam ausgewertet und Felder von dreidimensionalen Verzerrungstensen direkt berechnet werden. Die so berechneten Verzerrungstensen zeigen eine gute Übereinstimmung mit Herdflächenlösungen aus der Seismologie. So entspricht z.B. die berechnete ‚GNSS-Verzerrung‘ in der Gegend um St. Gallen den kürzlich dort ausgelösten Erdbebenmechanismen.

Die erarbeiteten Resultate stellen einen wichtigen Fortschritt für das Verständnis der Deformationsvorgänge in der Schweiz dar. Es ist ein Novum, dass anhand kleiner Deformationen, Herdflächen potentieller Erdbeben aus rein geodätischen Daten erstellt werden konnten.

Die Schweizerische Geodätische Kommission (SGK) dankt Herrn Dr. Villiger für den wertvollen Beitrag im Bereich der Geowissenschaften. Dem Schweizerischen Nationalfonds (SNF) und dem CCES (Competence Center Environment and Sustainability des ETH Bereichs), das im Rahmen des Projektes COGEAR einen Teil der Projektfinanzierung übernommen hat, spricht die SGK ihren grossen Dank aus. Viel Dank geht an die swisstopo, deren hochwertige Daten diese Untersuchungen erst ermöglichten und deren Projekt ‚swiss 4D‘ einen Grossteil des finanziellen Bedarfs abgedeckt hat. Der Schweizerischen Akademie für Naturwissenschaften (SCNAT) danken wir für die Übernahme der Druckkosten.

**Prof. Dr. M. Rothacher**  
Institut für Geodäsie und Photogrammetrie  
ETH Zürich

**Prof. Dr. A. Geiger**  
ETH Zürich  
Präsident der SGK

## PREFACE

Comparée à des régions sismiquement actives, comme la Grèce, par exemple, la Suisse est relativement calme. Néanmoins, de forts tremblements de terre n'y peuvent être exclus. Dans les régions de Bâle et du Valais des tremblements de terre de magnitudes supérieures à six ont déjà eu lieu.

Le développement de la métrologie géodésique et de la technologie satellitaire ont permis la mise à disposition des chercheurs d'outils permettant la détermination de petits changements temporels de certains paramètres terrestres. La dérive des continents, les déformations de la croûte terrestre et l'accumulation de tensions peuvent être déterminées et vérifiées par des moyens géodésiques. Cependant, ceci n'est pas aisé à prouver, particulièrement dans une région comme la Suisse à cause des très petits mouvements annuels générant de très petites distorsions, avec un maximum de 25 nstrain ou 2.5 mm pour une ligne de base de 100 kilomètres.

Le service topographique fédéral conduit depuis plusieurs années des mesures GNSS répétées sur son réseau de premier ordre. La série temporelle des coordonnées résultante, combinée avec la longue série temporelle des nivellements forment une base de données pour une estimation cohérente des déformations cinématiques en Suisse.

Grâce au développement, conduits au GGL, de l' »Adaptive Least-Square Collocation » (ALSC) et en considérant un modèle physique de la croûte terrestre il est devenu possible de calculer directement un champ tensoriel tridimensionnel des tensions et cela à partir d'une combinaison des mesures de surface comme, par exemple, le GPS et le nivellement. Les tenseurs des contraintes ainsi obtenus montrent une très bonne concordance avec les mécanismes focaux déterminés à partir des données sismiques. Par exemple, le mécanisme du récent tremblement de terre induit de St Gall est en agrément complet avec les tenseurs des tensions déterminé par GPS.

Ces résultats représentent un pas important en direction d'une connaissance plus approfondie des processus sous-jacents des déformations de la croûte terrestre en Suisse.

C'est une nouveauté qui a montré sa capacité de prédire les mécanismes focaux à l'aide de données GNSS ceci par la mise en évidence de minuscules déformations à long terme.

Le présent travail fait partie des activités du GGL et de la CGS dans le domaine de la détection des déformations récentes de la croûte terrestre.

La CGS remercie l'auteur, le Dr Arturo Villiger, pour cette précieuse contribution à la géodésie et à la tectonique.

Nous exprimons aussi notre gratitude au Fond National Suisse de la Recherche (SNF) et au CCES (Competence Center Environment and Sustainability du domaine des EPF) pour avoir, dans le cadre du projet COGEAR, partiellement financé ce travail.

Nous sommes reconnaissant au service topographique fédéral d'avoir mis à notre disposition leur excellent ensemble de données GPS et avoir financé le projet « Swiss 4D », dans le cadre duquel le présent travail a été mené. C'est grâce à cette aide que ce projet a pu être réalisé.

La CGS remercie l'Académie Suisse des Sciences Naturelles (SCNAT) pour avoir couvert les coûts d'impression du présent fascicule.

**Prof. Dr. M. Rothacher**  
Institut de Géodésie et Photogrammetrie  
ETH Zürich

**Prof. Dr. A. Geiger**  
ETH Zürich  
Président de la CGS

## FORWORD

Compared to seismically active regions like Greece the seismogenic hazard in Switzerland is relatively small. Nevertheless, larger earthquakes can't be excluded also in Switzerland. In the regions of Valais and Basel seismic events with a magnitude above six have occurred.

The development of the geodetic metrology and satellite technology have made tools available to the researchers allowing for the precise determination of even small changes of any earth related parameters. Continental drift, crustal deformations and the strain accumulation can be determined and verified by geodetic means. However, this prove is not easy to be given in the region of Switzerland, because of the very small yearly movements generating equivalently small yearly distortions at a maximum of 25 nstrain per year corresponding to 2.5 mm on a baseline of 100 km.

Since many years the Swiss office of topography is carrying out repeated GNSS measurements on its first order network. The resulting time-series of coordinates together with the long-standing levelling time-series form the data base for the estimation of a coherent kinematic deformation field of Switzerland.

Thanks to the further development of the ,Adaptive Least-Square Collocation (ALSC)‘, which was devised at GGL, and the consideration of a physical crustal model it became possible to directly calculate a three dimensional strain tensor field from the combined surface measurements, e.g. GPS and levelling. Straintensors thus obtained reveal a very high conformity with focal mechanisms determined from seismological data. For example the recently induced earthquake mechanism in the region of St. Gallen is in a complete agreement with the strain tensors determined by GPS-data.

The results represent an important step towards a deeper understanding of the processes underlying the crustal deformation in Switzerland. It is a novelty having shown the ability to predict focal mechanisms by GNSS data of very tiny long-term deformations.

The presented work is part of GGL's and SGC's activities in the domain of detection of recent crustal deformations.

The SGC thanks the author, Dr Arturo Villiger, for his valuable contribution to geodesy and tectonics. We also express our gratitude to the Swiss National Science Foundation and the Competence Center Environment and Sustainability of the ETH Domain (CCES) for partially funding the project in the frame of the project COGEAR.

We are very grateful to swisstopo, who enabled the project by contributing their excellent, high quality GPS datasets and by financing the project ,swiss 4D‘ in whose frame the present work has been carried out. The SGC thanks the Swiss Academy of Sciences (SCNAT) for covering the printing costs of this volume.

**Prof. Dr. M. Rothacher**  
Institut für Geodäsie und Photogrammetrie  
ETH Zürich

**Prof. Dr. A. Geiger**  
ETH Zürich  
Präsident der SGK



# Abstract

Switzerland is a region with relatively low seismicity compared to other lithospheric subduction zones. However, from historic earthquakes it is known that events with large magnitudes, above 6, have occurred. A major task was to extract the tectonic pattern of the velocity field based on Global Navigation Satellite Systems (GNSS) campaign type data (CHTRF 2010 solution) given the fact that the noise level and local influences are within the same order of magnitude as the deformation occurring.

The introduction of the adaptive least-squares collocation (ALSC) and its enhancement to determine the tectonically driven deformation field allowed to extract a reliable kinematic model for Switzerland. The final solution consists of the velocity field and its derivative, the strain rate field. Due to the relatively high density of measurement points, re-measured three or more times, the field could be retrieved from the data set. The horizontal velocities are mostly below 1 mm/yr and the uplift rates, determined from precise levelling, between 0 and 1.5 mm/yr. The deformation rates deduced amount to 25 nstrain/yr.

The thin plate model allowed to estimate also the vertical strain rate which was not possible to retrieve by the collocation technique alone. This is due to the lack of missing measurements within the crust since all levelling and GNSS measurements are performed on the surface.

The comparison of the strain rate field with seismological data showed a good accordance. The horizontal strain field confirms a compression of 15 nstrain/yr perpendicular to the Alpine chain. In the canton Valais seismic recordings observed extensional stress regimes. The collocation technique could reproduce the extension and retrieved a strain rate of 20 nstrain/yr. At the boundary of the study area uncertainties exist because of missing data outside Switzerland. This is a particular problem in the city of Basel, which lies at the southern end of the Upper Rheingraben. The 3-D strain rate tensor, using the thin plate model, has shown mostly similar fault plane solutions as the one obtained from earthquake analysis. The same is valid for the strain rate energy compared with the seismic energy released by earthquakes. The highest strain energy density is found in the eastern and western part of the Swiss Alps.

This project has been funded by swisstopo and the Geodesy and Geodynamics Lab, ETH Zurich. The work which was carried out for the project COGEAR was financed by the Competence Center Environment and Sustainability of the ETH Domain (CCES).



# Zusammenfassung

Die seismische Gefährdung in der Schweiz ist verglichen mit aktiven Regionen wie Griechenland klein. Grössere Erdbeben können jedoch nicht ausgeschlossen werden. Die Regionen Wallis und Basel weisen eine erhöhte Erdbebengefährdung innerhalb der Schweiz auf. In der Vergangenheit konnten verschiedene Erdbeben in diesen Gebieten, mit einer Magnitude über sechs, gemessen oder aus historischen Aufzeichnungen rekonstruiert werden. Um die tektonischen Vorgänge, welche zu Spannungsaufbau und Erdbeben führen können, zu eruieren, wurden GNSS-Kampagnenmessungen von der swisstopo durchgeführt und ausgewertet. Die dabei zu detektierenden Deformationswerte liegen bei 25 nanostrain (25 mm pro 1000 km) und die tektonisch verursachten Verschiebungen weisen eine ähnliche Grössenordnung wie die lokalen Bewegungen (z.B. Hangrutschung) oder das Messrauschen auf. Daher ist es eine grosse Herausforderung, den tektonischen Anteil in der CHTRF-2010-Lösung, welche GPS-Kampagnen von 1988 bis 2010 beinhaltet, zu identifizieren.

Für die Bestimmung des tektonischen Bewegungsfeldes wurde die Adaptive Least-Square Collocation (ALSC) Methode erweitert, um anschliessend GPS- (Lage) und Nivellement-Daten (Hebung) gemeinsam auszuwerten. Das daraus resultierende tektonische Geschwindigkeitsfeld sowie dessen räumliche Ableitung, das Deformationsfeld, konnte aus dem dichten Messnetz trotz der lokalen Einflüsse und des Messrauschens extrahiert werden. Da die Messungen auf der Erdoberfläche stattfinden, können aus der Kollokation heraus keine sinnvollen Strain-Werte für die vertikale Achse bestimmt werden. Um dennoch einen 3-D-Tensor zu bestimmen braucht es Modelle welche das Verhalten des Untergrundes beschreiben. Das dafür verwendete Modell besteht aus der Annahme einer dünnen Platte (Kirchhoff), welche gebogen wird. Aus der Biegung sowie der Volumenänderung kann ein 3-D-Tensor berechnet werden.

Die erzielten Deformationsfelder haben eine gute Übereinstimmung mit Erkenntnissen aus der Seismologie. Entlang der Alpenfront wies das Deformationsfeld Kompression senkrecht zur Front aus. Die Kompressionsrichtungen weisen ebenfalls gute Übereinstimmung mit den p-Achsen aus seismologisch bestimmten Herdlösungen auf. Im Wallis zeigen sich jedoch gewisse Divergenzen zwischen den beiden Achsen. Die Extension nördlich der Rhone wird jedoch von beiden Messarten bestätigt.

Diese Projekt wurde von der swisstopo und dem Geodesy and Geodynamics Lab, ETH Zurich, finanziert. Die Arbeiten welche im Zusammenhang mit dem Projekt COGEAR durchgeführt wurden sind vom Competence Center Environment and Sustainability des ETH Bereichs (CCES) finanziert worden.



# Contents

<b>1</b>	<b>Introduction</b>	<b>1</b>
1.1	Scope of work . . . . .	1
1.2	Research tasks . . . . .	2
1.3	Tectonic setting . . . . .	2
1.4	Geodetic strain determination in Switzerland . . . . .	4
<b>2</b>	<b>Data and data analysis</b>	<b>9</b>
2.1	Data sources . . . . .	9
2.1.1	Permanent GNSS stations . . . . .	9
2.1.2	GNSS campaign data . . . . .	10
2.1.3	Levelling data . . . . .	11
2.2	Regional effects . . . . .	13
2.2.1	Common mode . . . . .	13
2.2.2	Correlation analysis . . . . .	16
2.2.3	Conclusion . . . . .	19
2.3	Local effects . . . . .	19
2.3.1	Seasonal trend . . . . .	21
2.3.2	Monumentation stability . . . . .	27
2.3.3	Conclusion . . . . .	27
2.4	Multipath . . . . .	29
2.4.1	Multipath estimation . . . . .	29
2.4.2	Results . . . . .	31
2.5	Uplift rates from GNSS and levelling . . . . .	32
<b>3</b>	<b>Block detection</b>	<b>39</b>
3.1	Automatic block detection using a genetic algorithm . . . . .	39
3.1.1	Introduction . . . . .	39
3.1.2	Test field . . . . .	40
3.1.3	Application to the AGNES network . . . . .	42
3.1.4	Application to the CHTRF 2010 . . . . .	45
3.2	Manual block definition based on geological information . . . . .	47
3.2.1	Introduction . . . . .	47
3.2.2	AGNES: Horizontal components . . . . .	47
3.2.3	AGNES: Uplift component . . . . .	50
3.3	Conclusion . . . . .	50

---

<b>4</b>	<b>Adaptive least-squares collocation: Theory</b>	<b>53</b>
4.1	Theory . . . . .	54
4.2	Dilatation . . . . .	56
4.2.1	Determination of the dilatation parameters . . . . .	58
4.2.2	Dilatation definition . . . . .	59
4.3	Parameter estimation . . . . .	59
4.3.1	Velocity and strain estimation . . . . .	59
4.3.2	Trend and strain error estimation . . . . .	60
4.4	Thin plate model . . . . .	62
4.5	Strain energy density . . . . .	64
4.6	Fault planes from strain . . . . .	66
<b>5</b>	<b>Adaptive least-squares collocation: Results</b>	<b>69</b>
5.1	Generic example . . . . .	69
5.2	CHTRF 2010 . . . . .	72
5.2.1	Trend correlation length . . . . .	73
5.2.2	Scale . . . . .	73
5.2.3	Final solution . . . . .	81
<b>6</b>	<b>Comparison of the strain rate field with geophysical findings</b>	<b>87</b>
6.1	Kinematic Model of Switzerland . . . . .	87
6.2	Strain Energy . . . . .	91
6.2.1	2-D model . . . . .	91
6.2.2	3-D model . . . . .	91
6.2.3	Conclusion . . . . .	91
6.3	Strain rate tensor comparison . . . . .	94
6.4	Comparison with seismic findings . . . . .	96
6.4.1	Stress regimes . . . . .	96
6.4.2	Comparison of fault plane solutions . . . . .	96
6.4.3	Comparison with p-axis from earthquake solutions . . . . .	97
6.5	Comparison with world wide models . . . . .	99
<b>7</b>	<b>Dense GNSS network for small scale tectonic analysis in the Canton of Valais</b>	<b>101</b>
7.1	Introduction . . . . .	101
7.1.1	Tectonic in the Valais (TECVAl) . . . . .	102
7.1.2	Coupled seismogenic geohazards in Alpine regions (COGEAR) . . . . .	103
7.2	GNSS network . . . . .	106
<b>8</b>	<b>Conclusion and outlook</b>	<b>109</b>
	<b>Bibliography</b>	<b>112</b>

---

<b>Appendix A Data analysis</b>	<b>119</b>
A.1 Common mode results . . . . .	119
A.2 Monumentation stability . . . . .	123



# Acronyms

<b>AGNES</b>	Automated GNSS Network Switzerland
<b>ALSC</b>	Adaptive Least-Squares Collocation
<b>CGPS</b>	Continuous GPS
<b>CHTRF</b>	Swiss Terrestrial Reference Frame
<b>COGEAR</b>	Coupled Seismogenic Geohazards in Apline Regions
<b>FME</b>	Finite Element Modeling
<b>FFT</b>	Fast Fourier transform
<b>GGL</b>	Geodesy and Geodynamics Lab
<b>GMT</b>	Generic Mapping Tool
<b>GNSS</b>	Global Navigation Satellite Systems
<b>GPS</b>	Global Positioning System
<b>LSC</b>	Least-Squares Collocation
<b>SED</b>	Swiss Seismological Service
<b>SLR</b>	Satellite Laser Ranging
<b>TECVAl</b>	Tectonic in the Valais



# 1 Introduction

## 1.1 Scope of work

Earthquakes in Switzerland - the greatest natural hazard [*Federal Department of Environment, Transport, Energy and Communications*, 2006]

The objective of this thesis is to detect and assess tectonic movements using modern geodetic methods and correlate them with techniques of the adjacent disciplines of geology and geophysics. The threshold for geodetic detection of co-seismic motion has decreased to a few millimetres and will, therefore, significantly constrain the boundary conditions for modelling crustal deformations in regions with low deformation rates.

Before the advent of space-based geodetic methods in the early 1990, the determination of crustal deformation relied on terrestrial methods including triangulation networks, distance measurements, and levelling data. There exist several publications which try to determine the crustal deformation from the ground-based measurements as before 1990 the space borne techniques were not available for the detection of local deformation. The first deformation analyses for Switzerland were based on these techniques. Crustal uplift rates were analysed in e.g. [Gubler *et al.*, 1981; Geiger *et al.*, 1986] and the horizontal strain in [Reilly and Gubler, 1990]. Elmiger *et al.* [1995] focused on the Alp traverse which was observed by triangulation and distance measurements. Elmiger *et al.* [1995] state that the deformation rates are within the same order of magnitude as the estimated point coordinate accuracy and it is not possible to make any final statement on the deformation. However, the most plausible interpretation of their calculations is a compression in the northern part of Switzerland and extension in the South of the Swiss Alps along the traverse. The advent of the space based geodetic methods, mainly the GNSS and in particular the Global Positioning System (GPS), introduced the possibility to observe the intra-plate deformation in Switzerland which is mostly below 1 millimetre per year.

The data sources for this project are GNSS measurements and high-precision levelling data. The measurements are compiled and analysed. Methods to combine GNSS measurements [Brockmann and Schlatter, 2011] and levelling data [Schlatter, 2005] have been developed to form a coherent deformation field. Strain and stress parameters are deduced from an integrated model, which contribute to the seismic hazard assessment within Switzerland. The expected small deformation rates, up to 25 nano strain per year, necessitate sophisticated analysis and detection methods to be developed, tested, and applied.

## 1.2 Research tasks

*Egli et al.* [2007] presented the Adaptive Least-Squares Collocation (ALSC), an extended version of the well known least-squares collocation technique. They introduce a method to separate tectonic deformation from a dense and noisy data set and add a new approach to model the tectonic setup based on the measurements itself.

The predecessor of this work (project *Swiss 4D*), a cooperation between Geodesy and Geodynamics Lab (GGL) and swisstopo, introduced the ALSC method to adjust the correlation length between two points based on the extracted gradient field. The main idea behind this approach is that regions with high strain rates belong to tectonically active regions. Therefore, points lying on different sides of these regions belong to two different movement regimes and are (almost) un-correlated. Examples of such zones are, among others, plate boundaries and major faults. *Egli et al.* [2007] described and applied this method for each component (North, East, and Up) individually.

The ALSC method has been extended during this thesis to handle different measurement types and to combine all three axes in the collocation process. The correlation is modified during this process and used for all three components simultaneously. Strain and stress parameters are deduced from it, which contribute to the seismic hazard assessment within Switzerland.

The expected tectonic velocities with respect to the Swiss Molasse Basin are below 1 millimetre per year for the horizontal velocities and up to 1.5 millimetres per year for the uplift rates. The point of origin for the horizontal motion is located in Zimmerwald and the corresponding point for the uplift rates is located in Aarburg. Local influences may have a huge impact on the measured displacements. Local effects, regional (non-tectonic) phenomena and other disturbances (e. g. multipath) have to be considered when using GPS-based velocities. The Automated GNSS Network Switzerland (AGNES) of the federal office of topography (swisstopo) with its long time series (the oldest site is running since 1997) is ideal to determine the local influences and regional effects. Therefore, these time series are analysed to find seasonal and regional deformations and to derive statements on their possible influences on the final solution (i. e., the velocities).

## 1.3 Tectonic setting

The extraction of the tectonic deformation field of Switzerland is challenging due to small deformation rates. The tectonic motion is mainly driven by two different processes. The first part is caused by the de-glaciation of the last glacial epoch (17000 BP, [*Hinderer*, 2001]) and erosion transporting material to the Alp's border and causing rebound effects; the mass loss causes an uplift of the Alps to reach equilibrium (isostatic effect). The second part is driven by plate tectonics: the collision between the Eurasian plate and the Adriatic microplate [*Weissert and Stössel*, 2009; *Leddra*, 2010].

The origin and evolution of our continents is an ongoing research topic. In the Middle Age the origin and age of our world were explained consistently with the Bible. The scientists began to uncouple their theories from the theological interpretation [Leddra, 2010] and came up with better ideas on the processes affecting our continents. Around 1900 several ideas about the deformation processes were developed. *Wegener* [1912] introduced his theory of moving plates based on sediments, rock coherence on different continents, and the continental contours. It was competing with the geosyncline theory. In the middle of the 20th century the theory of plate tectonics got widely accepted in the scientific community and the geosyncline theory was rejected. New observations such as the discovery of ocean floor spreading proved the plate tectonic model to be appropriate [Frisch *et al.*, 2011; Weissert and Stössel, 2009]. The advent of new geodetic space based measurement techniques such as Satellite Laser Ranging (SLR) or TRANSIT (later GPS) enabled measuring the relative motion between continents and intra-plate deformations, leading to new global plate motion models.

The geodetic measurement techniques and other methods, such as rock dating, allow to reconstruct the past and present development of the Earth's surface. The processes leading to today's continents can be reconstructed from the Pangea continent in the Triassic era (230 million years ago), containing all today's continents, to the present state [Weissert and Stössel, 2009; Frisch *et al.*, 2011].

Figures 1.1 and 1.2 show the current plate motion calculated from the NUVEL-1A model [Argus and Gordon, 1991]. It is based on transform fault azimuths, earthquake slip vectors, and spreading rates from magnetic anomalies describing a global plate motion model distinguishing, among others, between the Nubian and Eurasian plate. However, it describes the plate motions on a large scale without using input data from geodetic techniques. Studies focusing on the Eurasian-Nubian collision zone come to the conclusion that there is a microplate, called Adriatic microplate, between Europe and Africa. Analysis of GNSS, seismic and geologic information confirms the existence of the Adriatic microplate with its borders in the Alps, Dinarics and Apennines [Nocquet and Calais, 2004; Battaglia *et al.*, 2004]. Calais *et al.* [2002] propose a rotation pole at 9.1 degree longitude, 45.3 degree latitude and a rotation rate of 0.5 degree per 1 million years. Nocquet and Calais [2004] conclude from the counterclockwise rotation that about 1 millimetre extension per year and right-lateral shear may be expected within the Swiss Alps (see Figure 1.3). The other major tectonic structures affecting Switzerland are, apart from the collision between the Adriatic microplate and Europe, the Bresse Graben and the Upper Rhinegraben [Frisch *et al.*, 2011].

The major fault structures within Switzerland are, among others, the Rhone-Simplon line, the Engadiner line, and the Insubric line (see Figure 1.4). The Rhone-Simplon line divides two different stress regimes [Maurer *et al.*, 1997] where strike-slip earthquakes have been observed in the Helvetic nappes (located North of the line) and normal fault mechanism in the southern part (Penninic naps) driven by a North-South extension. This is one of the most seismic active region within the country. The Insubric line is a major boundary

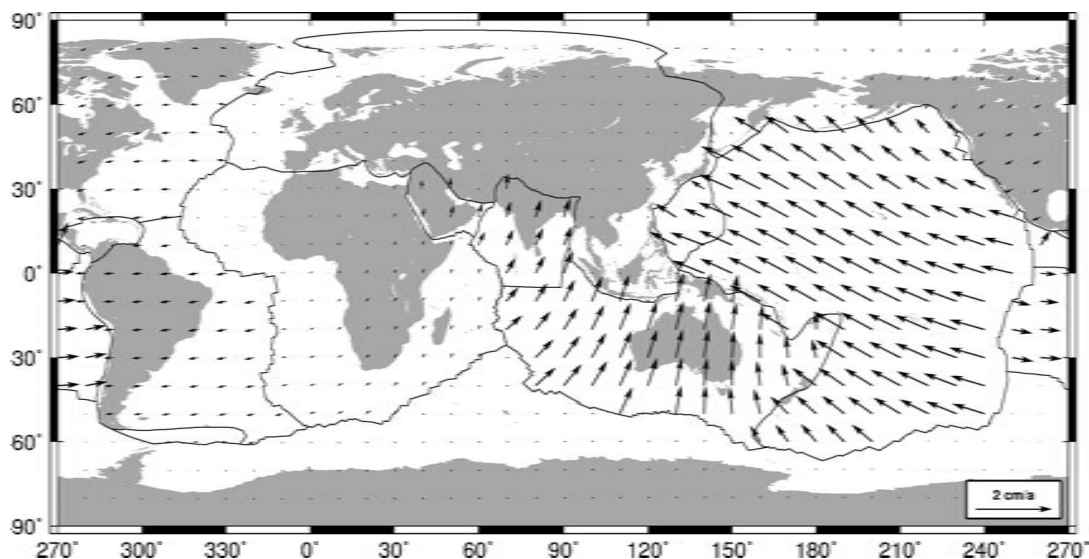


Figure 1.1: Global plate motion (NUVEL-1A) relative to Eurasia.

between the crystalline Alps on the Eurasian plate and southern Alps built on the Adriatic microplate [Schmid and Kissling, 2000; Giardini *et al.*, 2004]. The Engadiner line is located in the Canton of Graubünden and has a sinistral strike-slip mechanism [Labhart, 2009; Schmid and Fritzscheim, 1993].

## 1.4 Geodetic strain determination in Switzerland

The collision between the Nubian and Eurasian plate and the resulting orogeny leading to the Alps is still a matter of research. Geological information is analysed to reconstruct the exact process of the collision. With geodynamic modelling it is possible to obtain a deeper understanding of the process [Pfiffner *et al.*, 2000; Maurer *et al.*, 1997; Pfiffner *et al.*, 1997]. The data refers to the long-term deformations from the past. To study the ongoing processes recent data is required. A possibility is to study the earthquake mechanisms [Marschall *et al.*, 2013; Kastrup, 2002; Kastrup *et al.*, 2004] or using geodetic techniques to detect the ongoing surface deformation rates.

The observation of deformations with geodetic techniques is an important task in geodesy. It can be applied to small structures such as buildings or local phenomena (land slides or rockfalls) and allows to alert the local population in case of an emergency. It can also be used to understand the physical properties of the observed objects. The observation of large areas, such as whole continents or parts of them, allows to extract intra-plate deformations and plate motions. In the case of Switzerland, the intra-plate deformation has been analysed by triangulation methods [Elmiger *et al.*, 1995] and later by GNSS observations. This thesis focuses on the Swiss intra-plate deformation where one of the major obstacles is the low deformation rate (between zero and one millimetre per year).

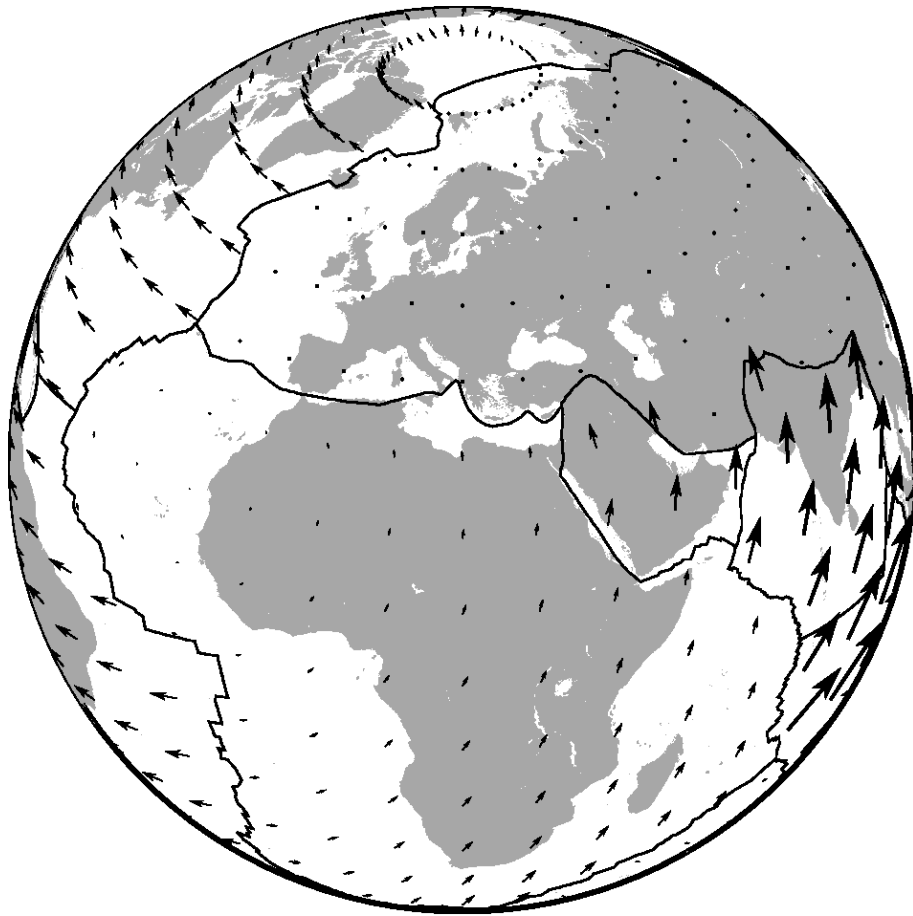


**Figure 1.2:** Global plate motion (NUVEL-1A) relative to Eurasia, perspective view.

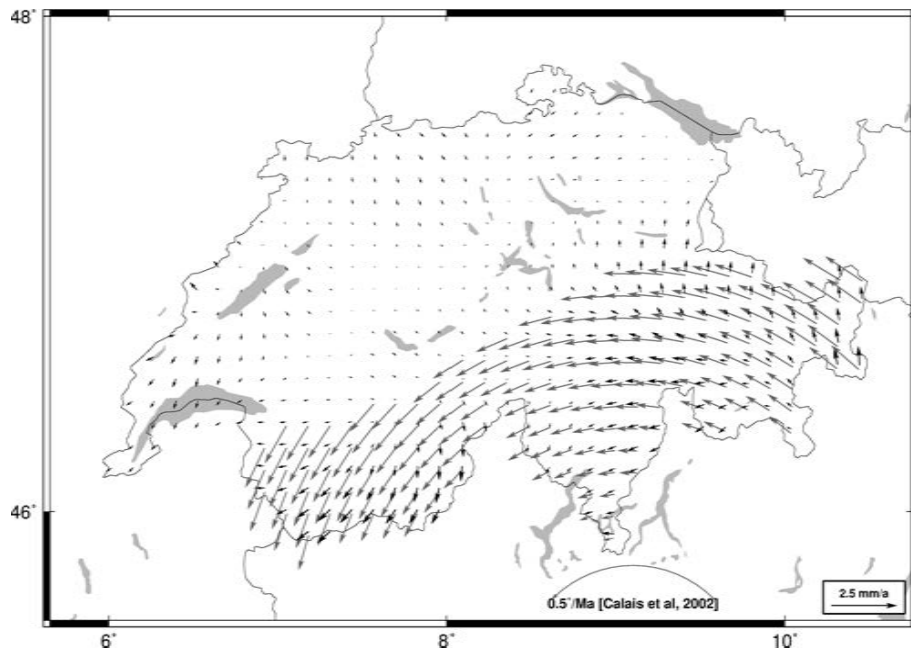


**Figure 1.3:** Rotation of the Adriatic microplate relative to Eurasia (grey arrows, pole:  $45.36^\circ$  N /  $9.10^\circ$  E [Calais et al., 2002]) and interpolated velocity field (CHTRF 2010, black arrows).

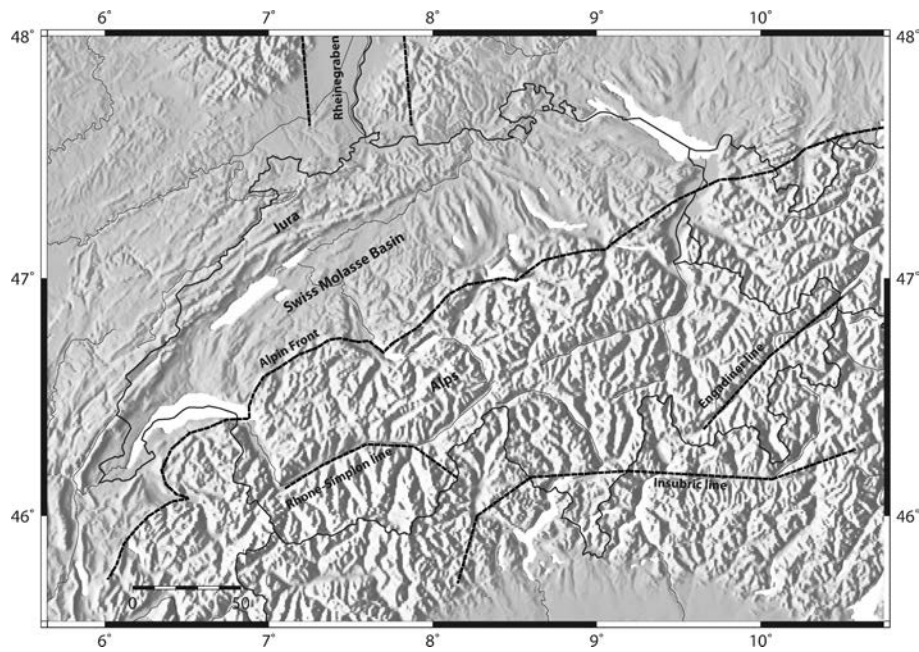


**Figure 1.4:** Simplified tectonic structures within Switzerland.

Before the advent of space-based geodetic methods, the strain determination relied on levelling and triangulation methods. The determination of the uplift rates within Switzerland using levelling data has been analysed in several publications (e.g. [Gubler *et al.*, 1981; Geiger *et al.*, 1986; Elmiger *et al.*, 1995]). The horizontal strain from triangulation networks was studied in [Reilly and Gubler, 1990], describing a heterogeneous strain field from triangulation measurements (1854 – 1971). They derive a shear strain of  $0.1 \pm 0.02$   $\mu\text{rad}/\text{year}$  for central Switzerland with an orientation of the compressional axis towards NW-SE.

A straight-forward method to analyse the intra-plate strain rates is using a triangulation method and deriving the strain rates. Its weaknesses are that it does not deliver a continuous strain field and it does not use sites nearby to account for additional local influences affecting the velocities. When dealing with small deformation rates, local effects may have a huge impact on the measured velocity. Other approaches use Finite Element Modeling (FME) to calculate the surface deformations based on various models. The models include, among others, the simplified tectonic structure, the boundary conditions and velocities, and the rheology parameters. Comparing the results with the measured surface deformations allows then to select the most feasible model. This approach has been used in various studies (e.g. [Heidbach and Drewes, 2003; Bauchau and Craig, 2009; Müller *et al.*, 2013]). Another method is using collocation techniques [Moritz, 1973] leading to a continuously interpolated field. It allows to calculate the deformation rates based on the surrounding points using the distance to weight their influences. Therefore, a common signal within a region can be separated from local effects (affecting one station). This method has been applied to various regions such as Greece and Turkey [Straub and Kahle, 1994; Hollenstein, 2007; Müller *et al.*, 2013].

Existing software implementations handle the strain extraction differently. The software SSPX [Cardozo and Allmendinger, 2009] allows to process the data in either ellipsoidal or Cartesian coordinate systems. The strain determination can be obtained with various methods. They are based on the Delaunay triangulation, Grid-Nearest Neighbour or Grid-Distance weighting. SSPX does not support the collocation technique which allows to extract a smooth strain field. Another implementation of the strain extraction is given by the software *strain* using the collocation technique in an ellipsoidal coordinate system. It has been used by the GGL for strain extraction in Greece [Hollenstein, 2007; Müller *et al.*, 2013].

The interpolation with the collocation approach is steered by the correlation function. In conventional collocation it is not possible to include discontinuities, such as tectonic structures, into the correlation functions. This feature is introduced with the ALSC approach developed by Egli *et al.* [2007]. It uses the given measurements to change the correlation between points based on the extracted deformation rates. This is achieved by deforming the metric used to determine the correlation. In this study, the method is enhanced to use only one correlation between two points for all three components.



## 2 Data and data analysis

The permanent GNSS stations deliver unique information about their displacements. As the Automated GNSS Network Switzerland (AGNES) network is operating since 1998, time series with more than 10 years of continuously recorded observations are available. The time series cover long-term displacements and may contain artifacts from the processing (reference sites, atmosphere, ionosphere, etc.). One of the challenges of data analysis is to separate the measured total deformation into short-term local, and long-term global parts. The final deformation field is derived from campaign data which has a much higher spatial density (more than 230 stations) than the permanent stations. Additionally, they cover a longer time span including campaign data from 1988 to 2010, but may be affected by a higher error budget.

### 2.1 Data sources

#### 2.1.1 Permanent GNSS stations

The Swiss Federal Office of Topography (swisstopo) maintains a permanent GNSS network of 30 sites (2013), the Automated GNSS Network Switzerland (AGNES) [Brockmann *et al.*, 2002a, 2006] (see Figure 2.1). It is used for commercial services delivering virtual reference stations to GNSS users in real-time or for post-processing purposes. The network is, apart from commercial application, also used for scientific purposes such as water vapor tomography [Troller *et al.*, 2006; Perler *et al.*, 2011] and geodynamic applications [Brockmann *et al.*, 2002b, 2012]. One of the major scientific goals is the continuously recording of GNSS observations delivering long-term time series. The establishment of the network began in 1998 and the full network is operational since more than 10 years.

Time series with more than 10 years of continuous observations allow to extract the network's deformation over the recorded time span. These deformations are caused by different local and global processes. They include tectonic deformations, local instabilities, and monumentation influences as they are located on buildings or on top of pillars (10 sites, up to a height of 9 meters) mounted on a concrete foundation. Small instabilities might cause motions at the sub-millimeter range. With a mean inter-station distance of roughly 60 kilometres the separation between tectonic and non-tectonic motions is difficult because the tectonic velocities might change between the different sites.



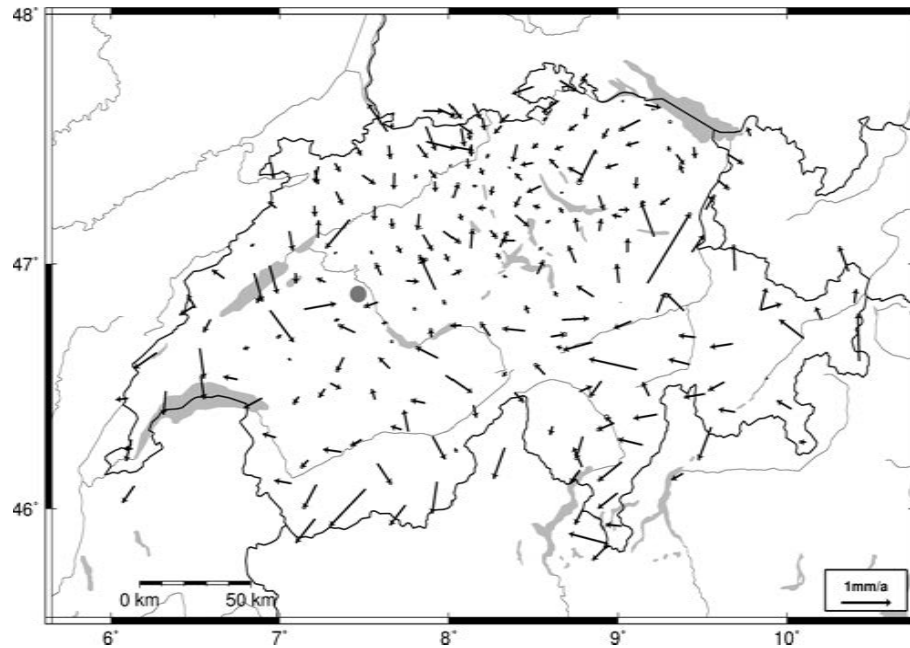


**Figure 2.2:** Velocities from the CHTRF 2010 campaign, relative to station Zimmerwald (marked as grey circle).

motion towards West anymore compared to the solution from 2004. The velocities have mostly been reduced by adding the new campaign. This becomes clear comparing the velocity histograms of both solutions (Figure 2.4). The reason for this result might be the better coverage by permanent stations and the longer time span covered by including the additional campaign.

### 2.1.3 Levelling data

Permanent GNSS stations deliver quite reliable uplift rates. The up components derived from the CHTRF campaigns have much higher uncertainties and cannot be used to obtain significant uplift values. The long history of terrestrial levelling compared to that of permanent GNSS measurements in Switzerland is ideal to fill this gap. The processing of the uplift rates includes levelling measurements from 1903 up to the present. For more information on the levelling data and their processing one may consult [Schlatter, 2005]. The expected uplift rates are similar to the horizontal rates lying in the millimetre to sub-millimetre per year range relative to Aarburg. The regions with the highest rates are located in the cantons Valais and Graubünden with up to 1.4 millimetres per year. Figure 2.5 shows the available uplift values based on levelling measurements (measured and processed by swisstopo).

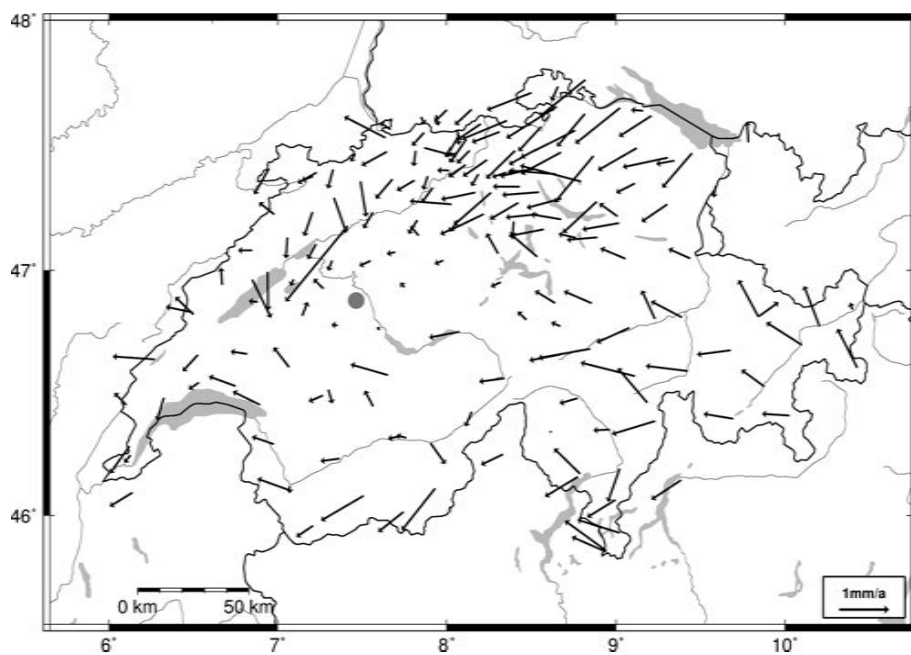


Figure 2.3: CHTRF 2004, velocities relative to station Zimmerwald (marked as grey circle).

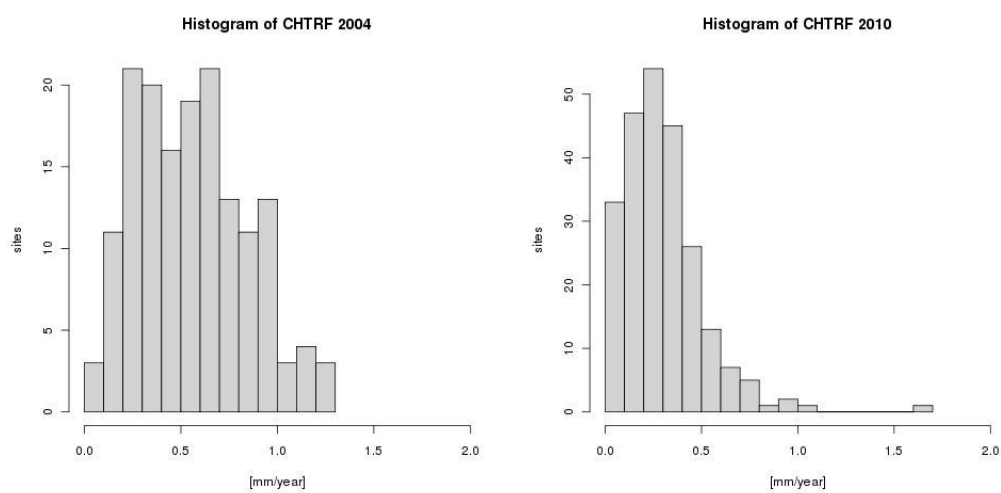
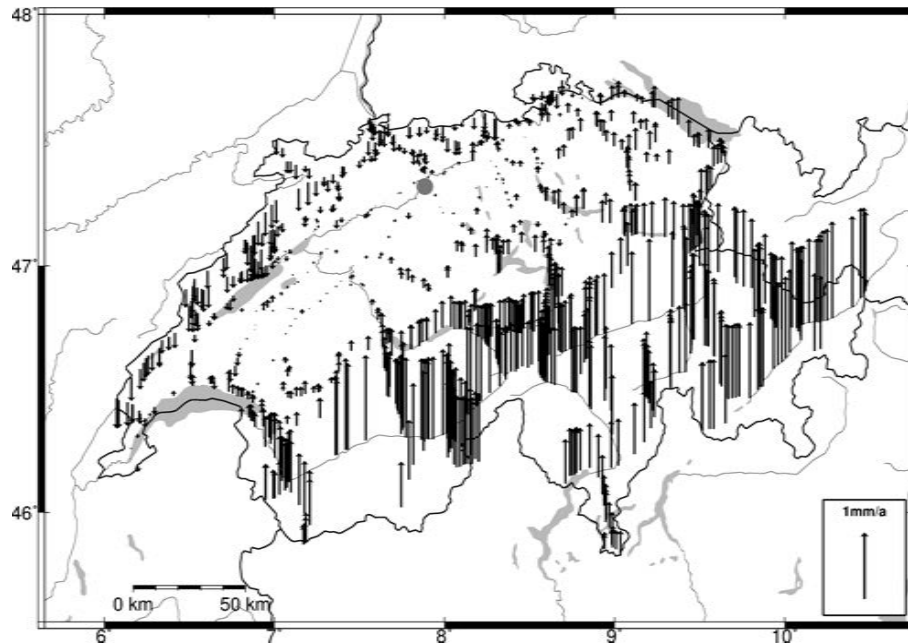


Figure 2.4: Histogram: Velocities from the CHTRF2004 (left) and CHTRF2010 (right) solutions.



**Figure 2.5:** Levelling data, uplift rates relative to Aarburg (marked as grey circle) [Schlatter, 2005].

## 2.2 Regional effects

### 2.2.1 Common mode

The continuous GNSS measurements deliver time series for each site describing their movements. The position is a combination of the true value, noise, systematic errors, and may even contain blunders. The noise can be reduced by measuring the position multiple times if the assumption of white noise can be made. Blunders may be detected using statistical tools. Physical background models of known effects allow to compensate their influences and, therefore, mitigate or eliminate their contribution to systematic errors.

The search for remaining spatially correlated errors, without knowing their exact origin, can be achieved considering their impact. Common mode is a tool to determine spatially correlated error sources [Wdowinski *et al.*, 1997; Hollenstein, 2007]. It allows to search for common patterns in a set of time series. By eliminating these common patterns one increases the precision of the velocity estimation and reduces the residuals. Hollenstein [2007] achieved an improvement of up to 25 percent in terms of variances on the velocity estimation. If no common mode signal exists, the method will not lead to an improvement for the precision obtained from the linear regression.

**Method**

The common mode detection and elimination can be done in three steps (after [Wdowinski *et al.*, 1997]):

1. Detrending: Velocity estimation using linear regression. The results are the velocities and the residuals at any epoch for each site  $s$ .

$$\epsilon_s(t) = X_s(t) - \hat{X}_s(t)q \quad (2.1)$$

with  $\epsilon_s$  as residual,  $X_s$  as the observation, and  $\hat{X}_s$  as the predicted position.

2. Stacking: Determination of the common mode signal.

$$\bar{\epsilon}(t) = \frac{\sum_{s=1}^S \epsilon_s(t)}{S} \quad (2.2)$$

where  $\bar{\epsilon}$  is the common mode signal and  $S$  the number of sites under consideration.

3. Filtering: Eliminating the common mode signal from the time series.

$$\hat{C}_s(t) = X_s(t) - \bar{\epsilon}(t) \quad (2.3)$$

with  $\hat{C}_s$  as the common mode filtered time series.

Complementarily it is possible to add a site-dependent weighting term to account for site-specific characteristics, like measurement accuracy, gaps in time series, etc. [Hollenstein, 2007]. Site-specific weighting is omitted here but in order to account for the site characteristics several site selections have been analysed. One of the variants includes only sites with good quality.

The determination of the common mode's standard deviation is achieved straight forward as the common mode is basically an epoch-wise mean value over various sites:

$$\sigma_{\epsilon}(t) = \sqrt{\frac{\sum_{s=1}^S [\epsilon_s(t) - \bar{\epsilon}_s(t)]^2}{S - 1}} \quad (2.4)$$

**Results**

Various sets of sites have been defined to search for common patterns in the time series. Each of them covers a specific region or characteristics to detect potential regional or altitude depending effects. The input data are time series obtained from the AGNES network; many sites have logged for more than 10 years. If common mode signals are detected they may have to be considered while interpreting the velocities derived from the CHTRF 2010 solution based on campaign data, too.

Four setups are defined in order to investigate different effects (see Figure 2.6).

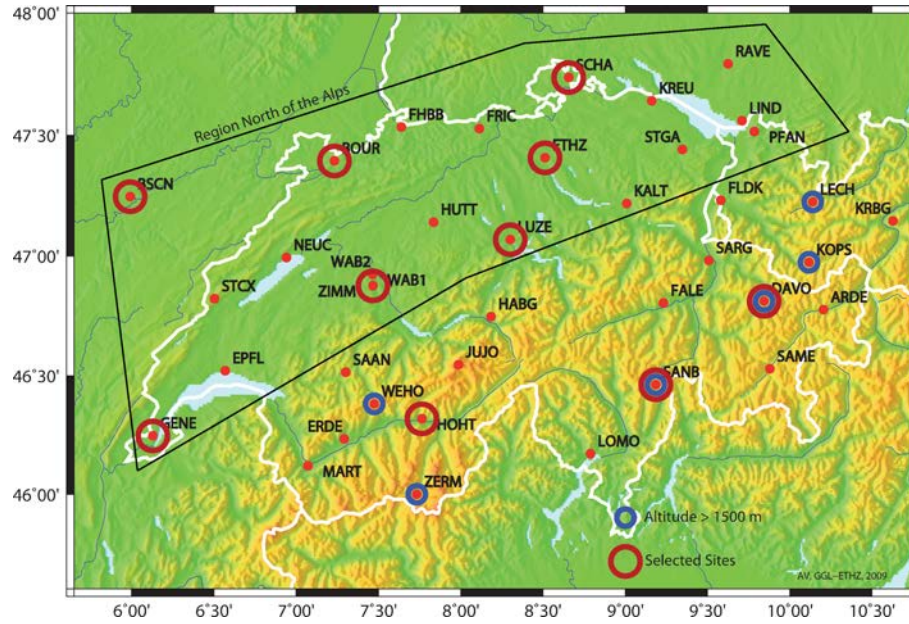


**Figure 2.6:** Regions defined for common mode estimation.

1. All sites within Switzerland: Search for global effects which may be caused by the reference frame or processing (red dots).
2. Location and quality criteria: Increase the quality by eliminating sites with large data gaps or several antenna changes (selected sites marked as larger red circles).
3. Sites North of the Alps: Detect possible regional effects only affecting the Swiss Molasse Basin (black polygon).
4. Sites with high altitude (above 1500 meters): Search for altitude depending signals (small circles, blue).

None of the 4 regions has shown statistically significant common mode signals. The analysis of all 4 site selections have similar outcomes. The results do not statistically significantly differ from zero. Figure 2.7 shows the retrieved signal based on the first setup; the two green lines represent the  $1\text{-}\sigma$  boundaries. The histograms of the deviation from zero are shown in Figure 2.8. Therefore, common-mode-free time series should lead to similar velocity and accuracy estimates compared to the non-corrected time series. This behaviour is true for all four site setups.

Using the linear regression algorithm the velocity and the RMS is estimated for each time series: common mode corrected and original one. To compare the improvement or degradation caused by the common mode signal, the change in percentage of the RMS is calculated and listed in Table 2.1. The percentage is calculated as follows:

$$\frac{\sigma_{normal} - \sigma_{commonmode}}{\sigma_{normal}} \cdot 100$$

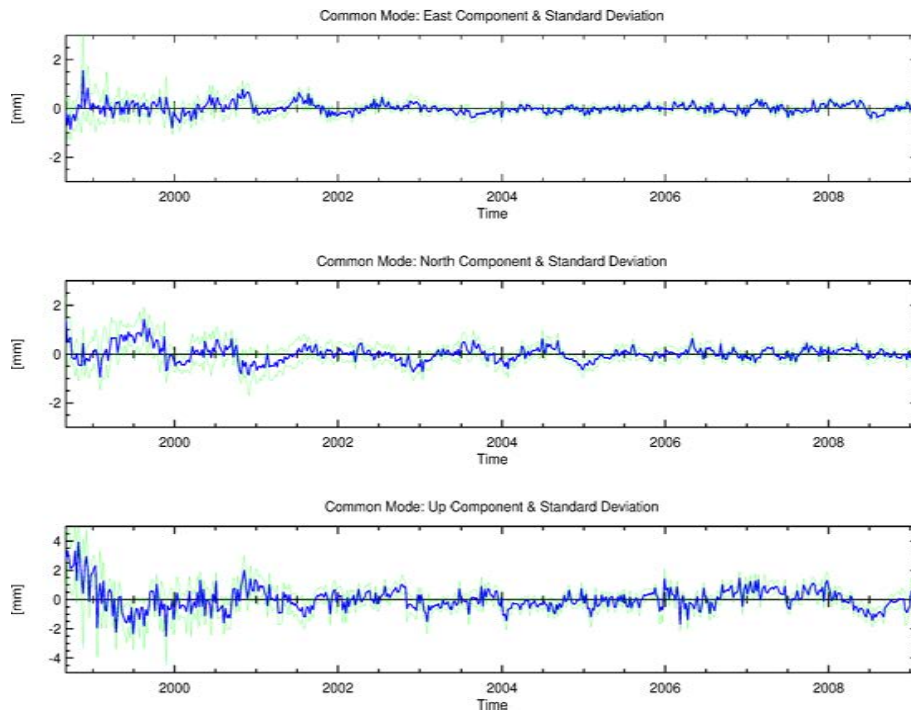


**Figure 2.7:** Common mode estimation for selection 1. The blue line is the calculated common mode signal and the green lines represents the  $\pm 1\sigma$  threshold.

It becomes clear from Table 2.1 containing data from setup 1, that no significant improvement over all sites is achieved. Some sites get even worse. Therefore, the common mode correction should not be applied to the data set and can be neglected for the campaign data. The velocities remained mostly equal after removing the common mode signal listed in table 2.2. The same behaviour is observed for all four tested setups (Appendix A.1).

### 2.2.2 Correlation analysis

Common mode estimation extracts similar patterns over a larger region covering several sites simultaneously. The correlation analysis between the time series of two sites determines their correlation. The correlation can be extracted using the well known cross-correlation algorithm which is explained in any standard textbook. This study applies it between all sites to search for possible correlations in certain regions. If a region with large correlation values is detected, an offset can be removed using the common mode technique [Wdowinski *et al.*, 1997].

The software *R* [R Development Core Team, 2009] offers a cross-correlation algorithm which is used to determine the correlation between the various time series. The relevant output is the maximum cross-correlation value and its time lag for each time series pair. To visualize the results the correlation values between Zimmerwald and the other stations are plotted in Figure 2.9; to have a better impression of the regions affected by correlation, the

**Table 2.1:** Variant 1: Improvement factor of the RMS in percent after the elimination of the estimated common mode (a negative sign implies an increased RMS). RMS of the original velocity estimation ( $\sigma_{O_E}, \sigma_{O_N}$ , and  $\sigma_{O_U}$ ), the common mode freed velocity estimation ( $\sigma_{CM_E}, \sigma_{CM_N}$ , and  $\sigma_{CM_U}$ ), and the per cent improvement of the precision ( $\%_{CM_E}, \%_{CM_N}$ , and  $\%_{CM_U}$ ) are listed in the table.

Station	$\sigma_{O_E}$	$\sigma_{O_N}$	$\sigma_{O_U}$	$\sigma_{CM_E}$	$\sigma_{CM_N}$	$\sigma_{CM_U}$	$\%_{CM_E}$	$\%_{CM_N}$	$\%_{CM_U}$
ARDE	0.70	0.89	3.12	0.67	0.86	3.00	3.7	3.0	3.6
BOUR	0.82	0.92	2.38	0.79	0.91	2.35	3.1	0.7	1.4
BSCN	0.58	1.02	1.54	0.57	1.15	1.62	0.7	-13.2	-5.1
DAVO	0.75	0.79	2.17	0.77	0.75	2.19	-1.8	5.6	-1.1
EPFL	1.26	3.11	2.04	1.22	2.91	1.95	2.8	6.5	4.5
ERDE	0.62	0.94	2.53	0.58	0.94	2.43	5.7	-0.3	4.0
ETHZ	0.82	0.85	1.86	0.85	1.01	1.93	-3.8	-18.4	-3.6
FALE	0.76	1.55	2.57	0.74	1.66	2.47	3.7	-6.5	3.7
FHBB	0.88	0.91	1.78	0.91	0.85	1.82	-2.7	5.9	-2.1
FLDK	0.81	1.38	1.69	0.77	1.25	1.78	4.7	9.7	-4.9
FREI	0.54	0.72	1.98	0.48	0.72	2.17	12.0	-0.1	-9.5
FRIC	0.65	1.29	3.00	0.67	1.31	3.03	-3.6	-1.8	-0.9
GENE	0.81	1.22	2.15	0.77	1.11	2.11	5.2	9.2	1.8
HABG	0.81	0.84	3.49	0.76	0.79	3.27	7.1	5.0	6.2
HOHT	0.79	1.33	2.84	0.79	1.41	2.70	0.5	-6.3	4.9
HUTT	0.86	0.61	2.04	0.84	0.54	1.99	2.6	12.1	2.2
JUJO	1.46	2.14	6.51	1.39	2.09	6.34	4.9	2.3	2.7
KOPS	0.81	2.04	2.19	0.75	1.98	2.16	7.5	2.9	1.6
KRBB	0.62	0.63	3.15	0.59	0.71	3.17	4.1	-12.9	-0.8
KREU	0.67	0.68	1.88	0.72	0.63	1.79	-7.8	8.2	4.8
LECH	0.58	0.82	1.69	0.54	0.73	1.63	7.4	11.3	3.5
LIND	0.74	0.80	1.97	0.70	0.71	1.98	5.3	11.2	-0.1
LOMO	0.77	1.73	2.62	0.80	1.71	2.67	-3.0	0.9	-2.0
LUZE	0.63	1.44	2.09	0.62	1.27	2.12	1.8	11.8	-1.5
MART	1.21	0.98	3.57	1.21	0.93	3.38	-0.2	4.5	5.5
NEUC	0.87	1.61	2.21	0.84	1.68	2.13	2.8	-4.6	3.5
PAYE	1.38	1.36	1.56	1.39	1.51	1.56	-0.3	-11.3	-0.6
PFAN	1.05	1.01	3.36	1.05	0.99	3.27	0.5	2.7	2.8
RAVE	0.64	0.63	1.65	0.63	0.60	1.67	2.6	4.1	-0.8
SAAN	0.78	0.81	2.55	0.74	0.80	2.54	5.3	1.8	0.5
SAME	1.01	0.85	3.02	0.99	0.86	2.90	1.6	-1.1	4.0
SANB	0.85	1.12	3.97	0.83	1.09	3.85	2.1	2.4	3.1
SARG	0.96	1.95	3.26	0.94	1.84	3.11	2.0	6.1	4.6
SCHA	0.98	1.06	1.70	0.96	1.18	1.71	2.1	-10.9	-0.7
SIGM	0.54	0.91	1.38	0.52	0.81	1.42	3.5	11.3	-3.1
STCX	1.27	2.15	2.30	1.22	2.02	2.29	3.6	5.7	0.5
STGA	1.03	0.85	2.15	1.02	0.77	2.07	0.7	9.1	3.7
VARE	0.56	1.57	2.67	0.53	1.59	2.68	4.6	-1.3	-0.2
VISW	0.53	1.18	1.52	0.45	1.16	1.54	14.6	2.0	-1.0
WEHO	1.56	0.83	2.19	1.46	0.87	2.26	6.1	-4.8	-3.2
ZERM	1.03	1.14	7.13	1.00	1.13	6.85	2.7	1.2	4.0
ZIMM	0.79	0.85	2.54	0.76	0.81	2.32	3.4	5.3	8.8
ZIM2	0.54	0.82	1.90	0.52	0.77	1.74	3.0	5.3	8.1

**Table 2.2:** Variant 1: Velocity estimation before and after the removal of the common mode signal in millimetres per year. The input data has already been de-trended using the Bernese GNSS software (by swisstopo). The original time series velocities are not zero as antenna changes and individual point accuracies are not taken into account in the linear regression.

Station	Original time series			Common mode freed		
	$v_e$	$v_n$	$v_u$	$v_e$	$v_n$	$v_u$
ARDE	-0.00	0.02	0.01	-0.01	0.01	-0.01
BOUR	0.01	-0.01	-0.06	0.01	-0.03	-0.08
BSCN	0.00	0.01	0.02	-0.00	-0.01	0.01
DAVO	-0.01	-0.00	0.03	-0.00	0.01	0.04
EPFL	-0.00	-0.01	0.05	-0.00	-0.00	0.02
ERDE	0.09	-0.04	0.49	0.12	-0.02	0.99
ETHZ	0.00	0.02	0.04	0.00	0.03	0.05
FALE	0.00	0.02	0.02	-0.01	0.01	0.01
FHBB	0.01	0.01	-0.00	0.01	0.02	0.01
FLDK	-0.05	0.03	-0.06	-0.06	-0.01	-0.10
FREI	0.16	0.41	-0.38	0.15	0.43	0.04
FRIC	-0.00	-0.01	-0.06	-0.00	-0.03	-0.08
GENE	0.01	0.00	0.01	0.01	-0.01	-0.00
HABG	0.05	0.02	0.45	0.06	0.05	0.92
HOHT	0.00	-0.00	-0.01	0.00	-0.02	-0.02
HUTT	-0.00	-0.01	-0.01	-0.00	-0.02	-0.03
JUJO	-0.05	-0.04	0.03	-0.05	-0.03	0.04
KOPS	0.01	0.05	0.07	0.00	0.00	0.12
KRBG	-0.03	0.01	0.07	-0.04	-0.03	0.03
KREU	-0.01	-0.00	-0.03	-0.02	-0.01	-0.04
LECH	-0.03	0.01	0.08	-0.04	-0.03	0.03
LIND	-0.03	-0.01	-0.05	-0.04	-0.05	-0.09
LOMO	-0.01	-0.01	0.03	-0.01	0.00	0.04
LUZE	-0.01	0.01	-0.07	-0.01	-0.01	-0.09
MART	0.01	0.02	0.05	0.01	0.01	0.03
NEUC	-0.00	-0.02	0.04	-0.01	-0.02	0.02
PAYE	0.01	-0.02	-0.03	0.01	-0.04	-0.02
PFAN	0.01	0.00	0.05	0.01	0.02	0.05
RAVE	-0.03	-0.00	0.03	-0.05	-0.02	0.00
SAAN	0.01	-0.00	0.02	-0.00	-0.01	0.01
SAME	-0.02	0.00	-0.01	-0.03	-0.01	-0.02
SANB	-0.01	0.03	0.03	-0.02	0.02	0.02
SARG	-0.01	-0.01	-0.02	-0.01	-0.02	-0.04
SCHA	-0.01	-0.01	-0.03	-0.01	-0.03	-0.05
SIGM	-0.01	-0.02	-0.00	-0.04	-0.03	-0.04
STCX	0.00	-0.01	0.01	-0.01	-0.02	-0.00
STGA	-0.01	0.00	-0.02	-0.01	-0.02	-0.03
VARE	0.02	0.04	0.03	0.05	0.06	0.52
VISW	-0.72	1.51	-0.35	-0.48	1.82	-0.35
WEHO	-0.04	0.04	0.23	-0.02	0.03	0.81
ZERM	-0.01	-0.01	0.30	-0.00	-0.00	0.46
ZIMM	-0.00	-0.00	0.03	-0.00	0.01	0.05
ZIM2	-0.07	0.04	0.17	0.14	0.25	0.75

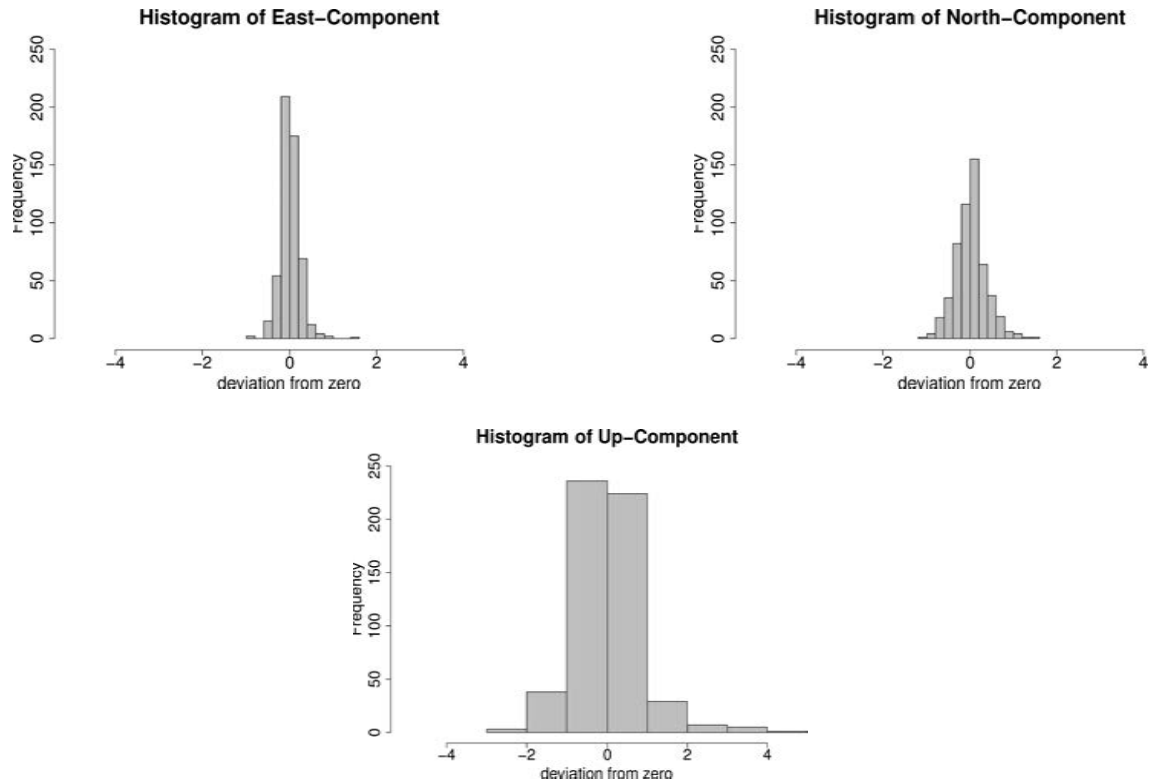


**Figure 2.8:** Histogram of the common mode deviation from zero for variant 1.

values have been interpolated and plotted as a grid. This should highlight regions where several sites are similarly correlated to the site Zimmerwald. However, the correlation analysis did not reveal any zones with high correlation values. It can therefore be assumed that the sites are mutually independent.

### 2.2.3 Conclusion

Neither the common mode analysis nor the correlation calculation reveal any major regional signals. It is therefore legitimate to assume the sites to be independent and to neglect their cross-correlations. Note that local effects may still disturb the assumption of a purely linear motion. Such effects are clearly visible and analyzed in Section 2.3.

## 2.3 Local effects

The environment may have a direct influence on the position of a site. Therefore, it may hide the purely geodynamically driven deformations. Possible effects are landslides, monumentation instabilities, or temperature variability leading to thermal extension of the monumentations.

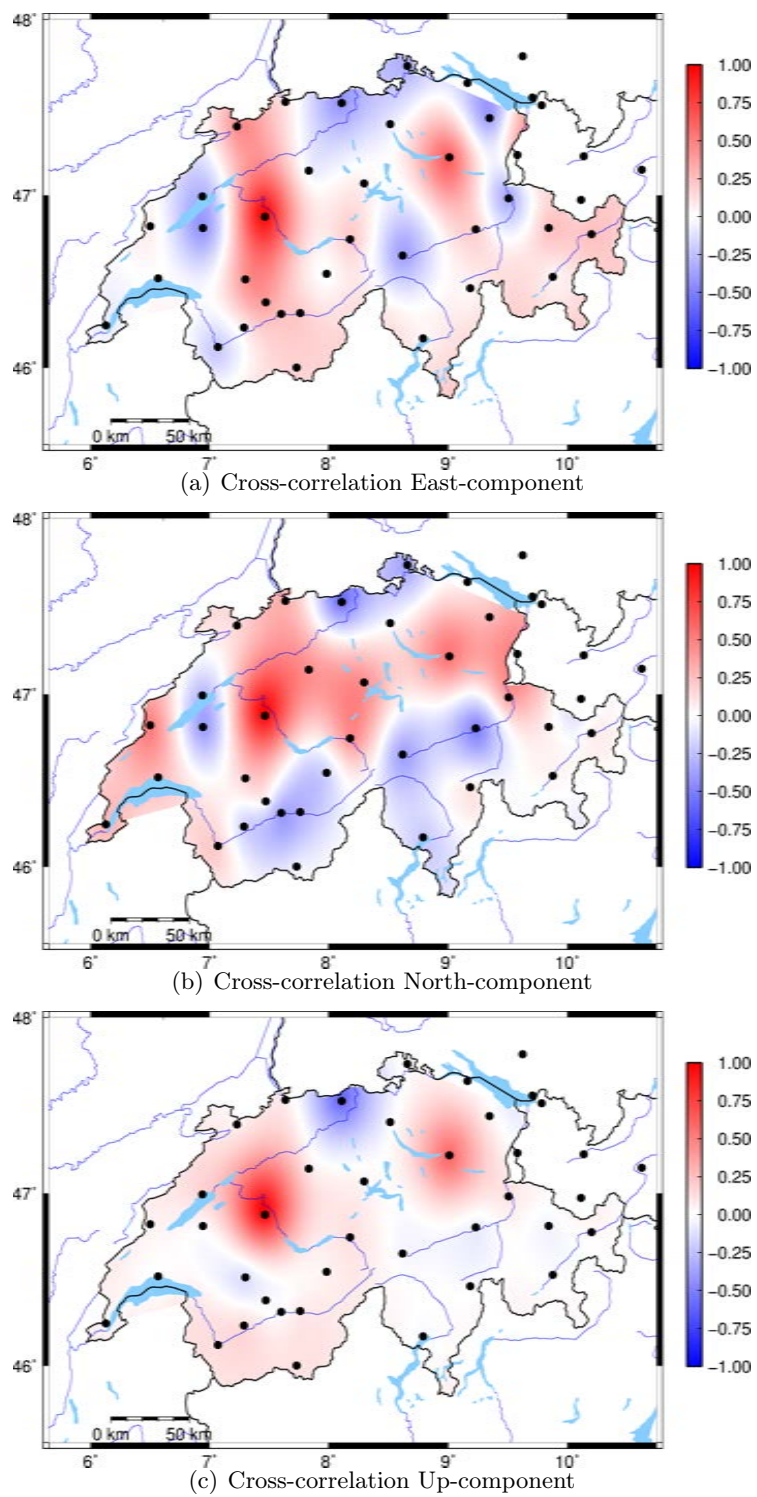


**Figure 2.9:** Cross-correlation values between ZIMM and the AGNES sites.

### 2.3.1 Seasonal trend

Various phenomena may lead to seasonal effects in the Continuous GPS (CGPS) time series. *van Dam et al.* [2001] describe effects of crustal displacements due to continental water, hydrological, and atmospheric loading. Therefore, *Blewitt and Lavallée* [2002] propose to simultaneously estimate annual, semi-annual signals, and the velocity. However, long time series reduce the influence of neglected seasonal effects. As most AGNES sites are recording and operating for more than four years the bias is reduced to a negligible minimum [*Blewitt and Lavallée*, 2002] but it may affect the accuracy estimations.

Most ground movements of seasonal nature predominantly reveal an annual period. In a first approximation a sinusoidal signal may be assumed, However, the stacking method would be more appropriate for the analysis of general periodic signals. All time series have been Fourier-transformed for a first assessment of potential signals. Because data with equidistant data sampling is required for the Fast Fourier transform (FFT), missing values (outliers, data gaps, ...) have been filled by zeros. Time series with data gaps longer than 5 weeks have been split into two parts. Only the longer part is used in the further processing.

Another tool to detect seasonal signals is the auto-correlation function. It is similar to the cross-correlation method applied in Section 2.2.2 but instead of using two different sites it is done using the same series moving it along the time axis. If the time lag is zero, the auto-correlation is 1 and not displayed in the plots as it does not contain any useful information.

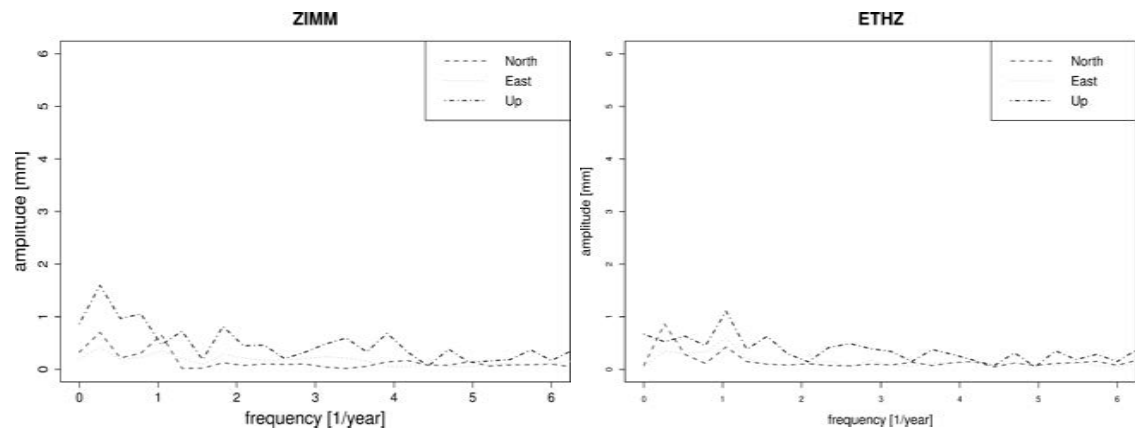


**Figure 2.10:** Fourier spectrum of the residuals of the de-trended position time series of ZIMM (left) and ETHZ (right) respectively.

Comparing results from the FFT and the autocorrelation analysis for the sites ZIMM and ETHZ (see Figures 2.10 and 2.11) reveals seasonal signals in the time series. Knowing the repetition frequency allows it to extend the linear regression by introducing additional parameters covering seasonal signals. Compared to the FFT the estimation of sinusoidal terms uses the whole time series independent of sampling rates and gaps. A sinusoidal

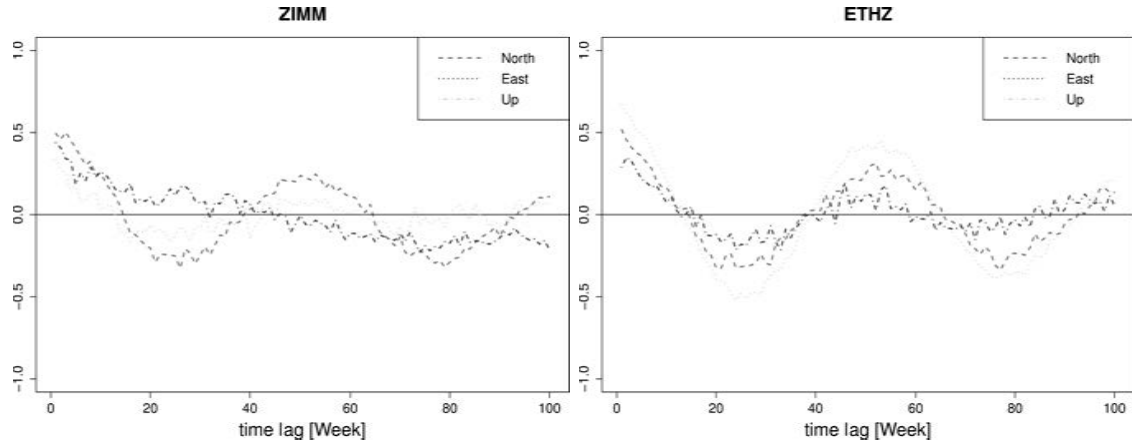
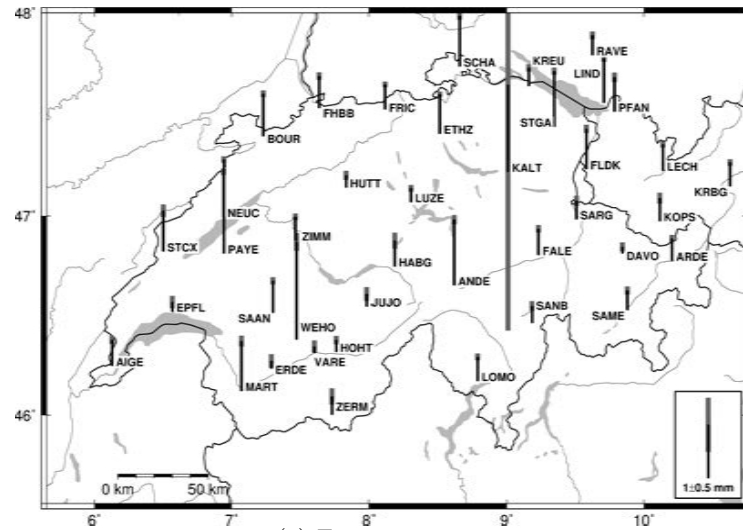


**Figure 2.11:** Auto-correlation function of the time series of station ZIMM (left) and ETHZ (right).

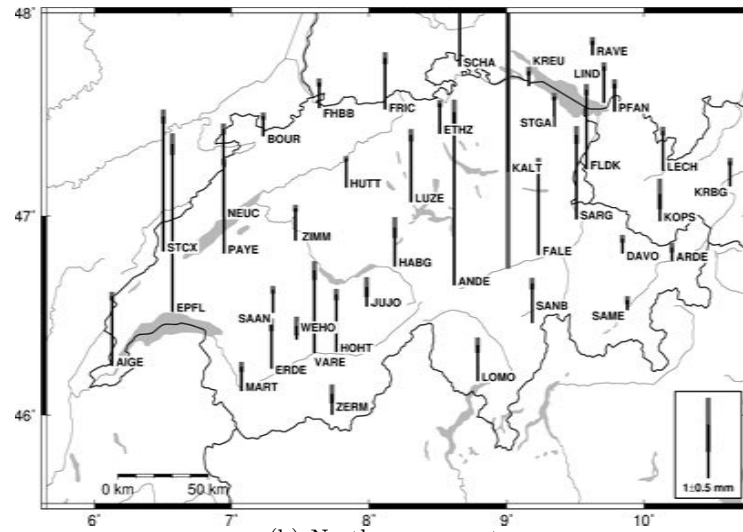
annual ( $\omega_a$ ) and semi-annual ( $\omega_s$ ) signal is estimated minimizing the squared residuals of the following model:

$$x(t) = a + bt + c \sin(\omega_a t) + d \cos(\omega_a t) + e \sin(\omega_s t) + d \cos(\omega_s t) \quad (2.5)$$

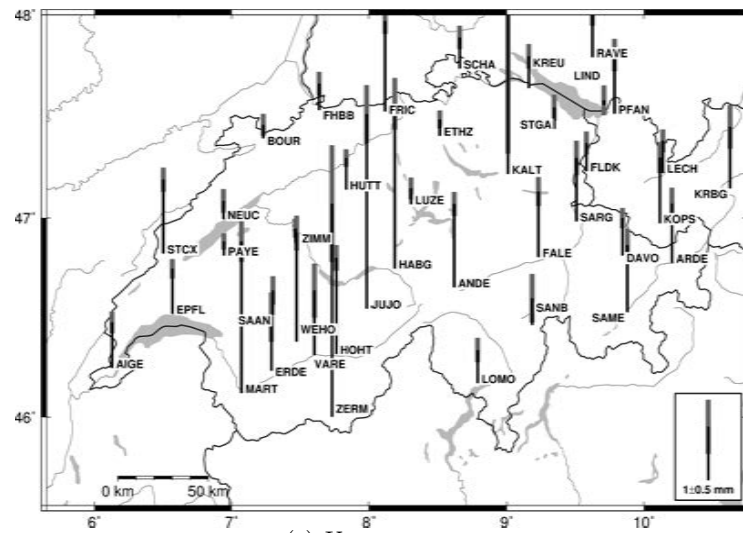
The results are plotted on a geographical map (see Figures 2.12, 2.13, 2.14, and 2.15). As expected from Section 2.2.3 no regional signals are found.



(a) East component

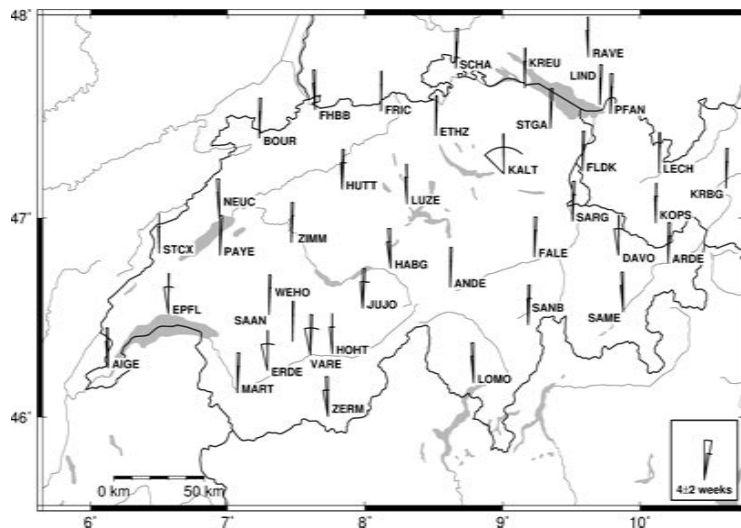


(b) North component

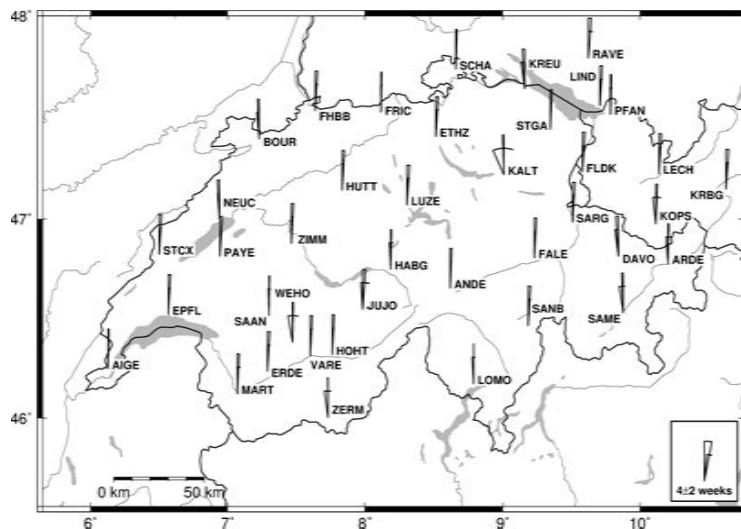


(c) Up component

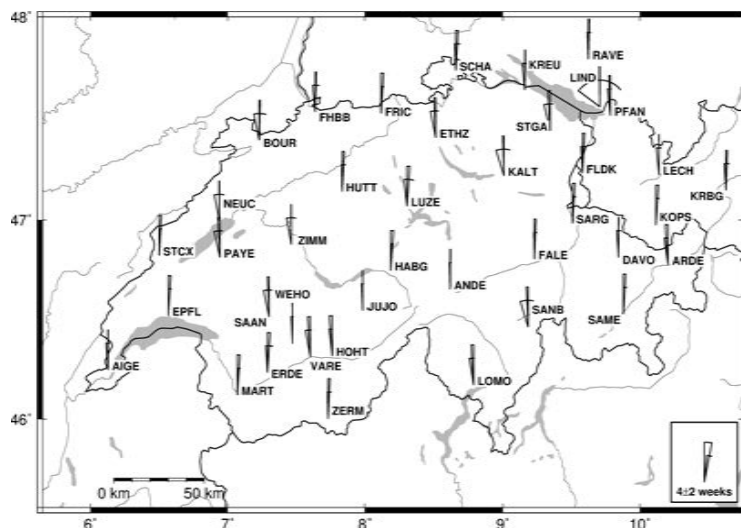
Figure 2.12: Annual sinusoidal signal: Amplitude.



(a) East component

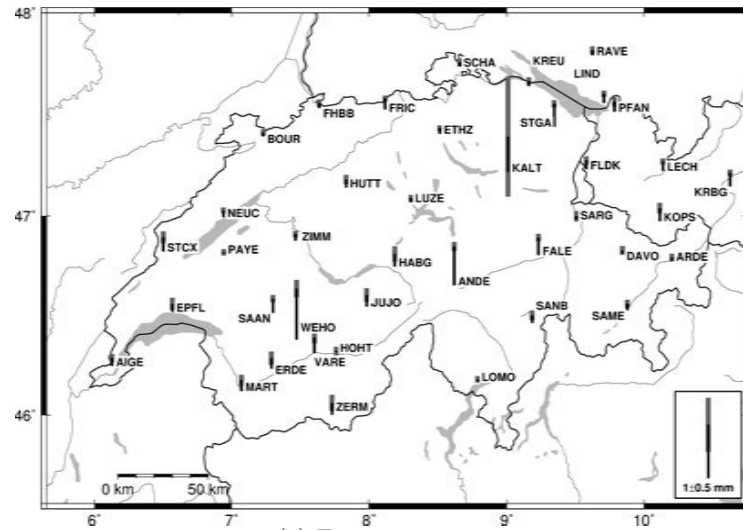


(b) North component

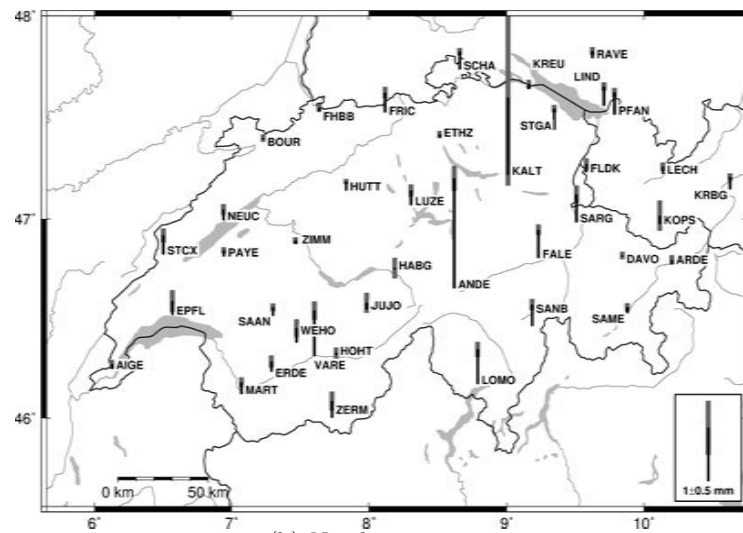


(c) Up component

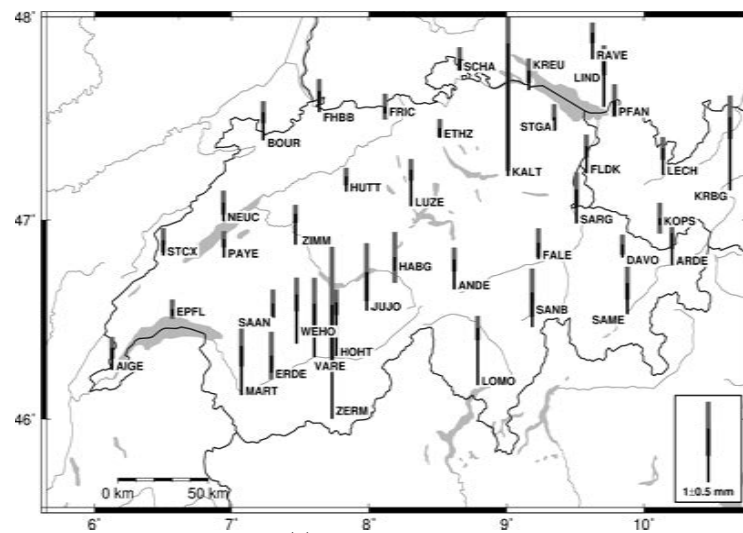
Figure 2.13: Annual sinusoidal signal: Phase.



(a) East component

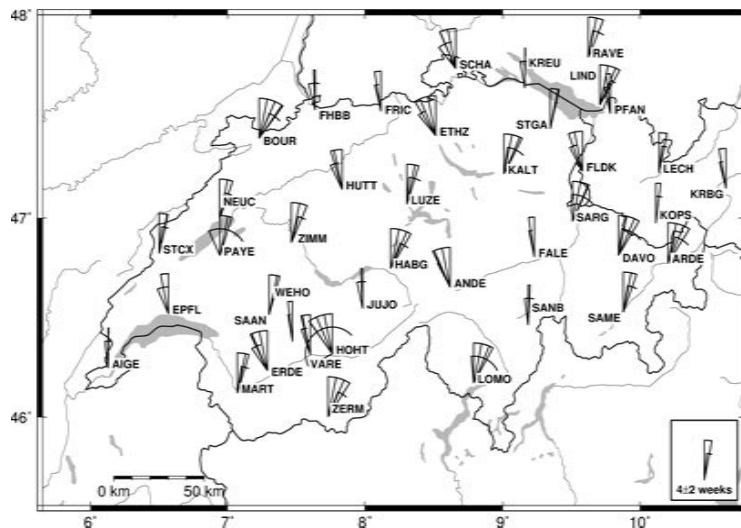


(b) North component

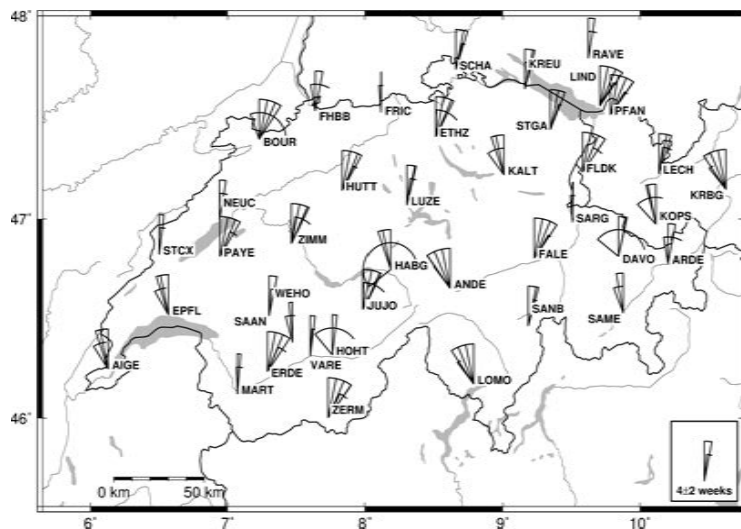


(c) Up component

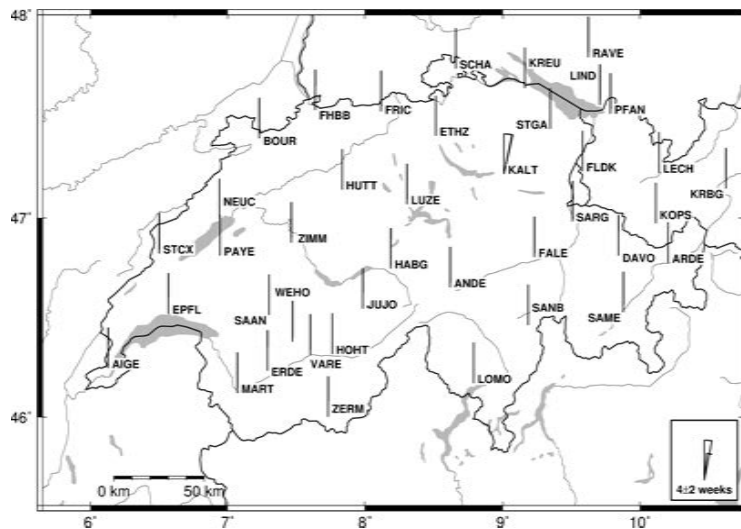
Figure 2.14: Semi-annual signal: Amplitude.



(a) East component



(b) North component



(c) Up component

Figure 2.15: Semi-annual signal: Phase.

### 2.3.2 Monumentation stability

Monumentation stability is a major issue for the extraction of small tectonic velocities. If the monumentation is drifting constantly over long time periods it will be observed by the GNSS measurements and adulterate the assumption that long-term movements are only connected to tectonic movements [Zhang *et al.*, 1997].

Long-term motion cannot be separated into tectonic and monumentation-based parts using only GNSS measurements from a single antenna. We tried to estimate the annual oscillation and derive evidences of the site's stability. For this purpose a stacking algorithm has been applied creating the monthly means using the whole de-trended time series. The residuals after the velocity estimation should have a repeatability period of one year assuming that only seasonal effects with a yearly repeating cycle occur. The stacking algorithm is independent from the signal form in contrast to a Fourier analysis where seasonal signals are assumed to be sinusoidal. We have done the stacking using monthly means of weekly solutions.

Figure 2.16 and Appendix A.2 display the stacking results. Even though the oscillation around zero is within the three sigma boundary, annually recurring patterns are visible.

### 2.3.3 Conclusion

Monumentation stability is a major issue for the purpose of observing geodetic velocities. Various approaches to minimize and quantify the effects caused by local issues have been applied to the time series. The stacking method did reveal clear patterns for the site-specific yearly motions. The range lies between 0 and 4 mm. However, taking the accuracy of the output signal into account shows that the results are not really significant, even though the results show clear motion patterns. Long time series reduce the influence of this effect for the velocity estimation. Short time series may still suffer from the seasonal effects and their velocities have to be interpreted with caution. This is important for the new COGEAR sites (see Chapter 7).

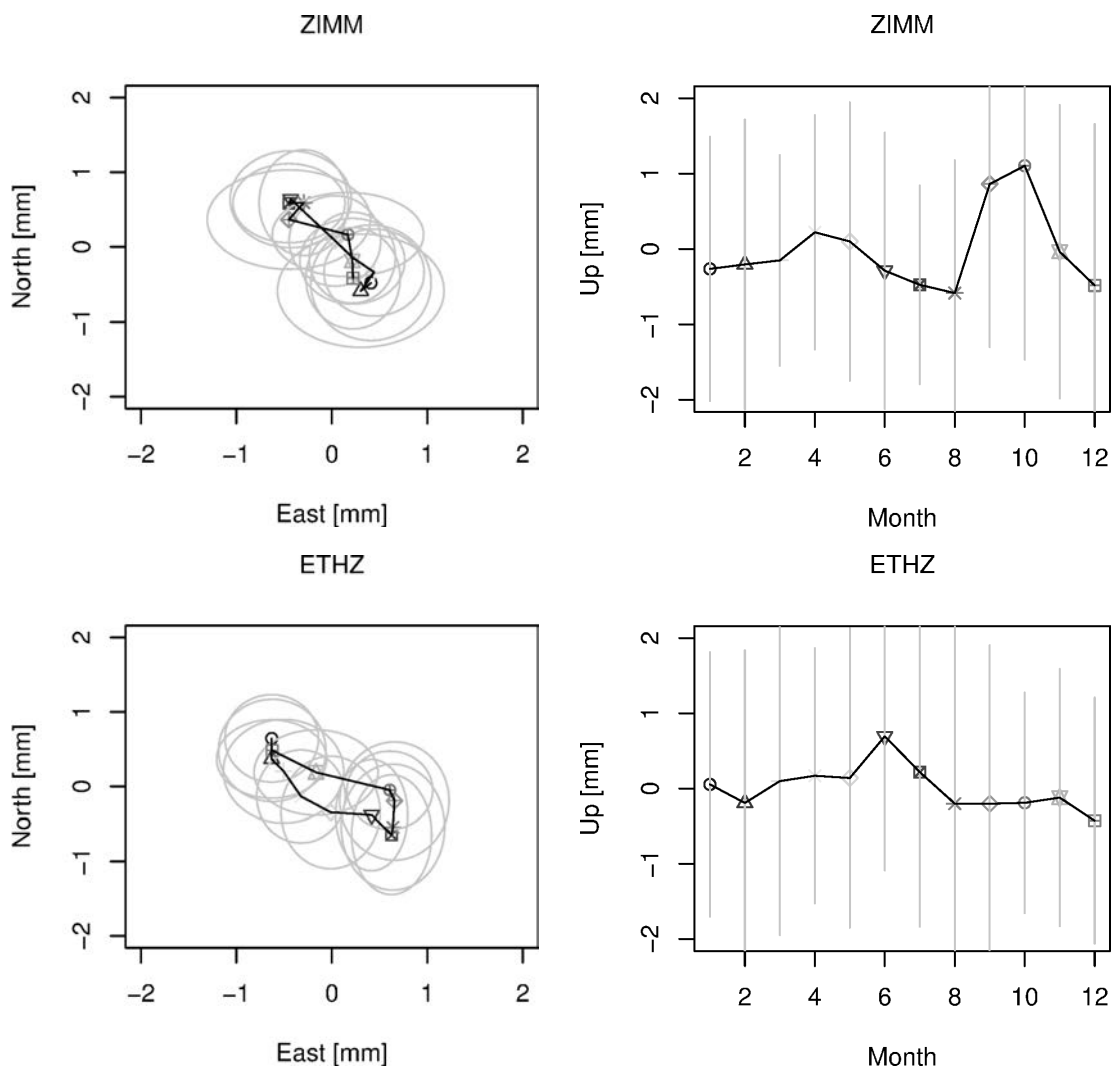


**Figure 2.16:** Stacking: Each component has been stacked on monthly basis to obtain the yearly movement and its accuracy ( $1 \sigma$ , blue line). The left plot displays the monthly means for the horizontal position. The right figure shows the monthly uplift rate. Each month is represented by its own symbol.

## 2.4 Multipath

GNSS signals are disturbed as they travel through ionosphere and troposphere. These disturbances are time varying and lead to advances which are interpreted as extended or shortened path length compared to the undisturbed Euclidean distance. Because the ionosphere is dispersive it is possible to reduce its effect by combining measurements on different frequencies. The tropospheric effect can be divided into dry and wet delay terms. Under the hydrostatic equilibrium assumption, the dry delay can be modeled by ground pressure and temperature, leaving the wet delay, which is given by the total delay minus the dry delay.

Further issues to be considered are antenna phase center variations and multipath. Antenna phase center variations can be taken into account to some extent using calibrated antennas. Multipath depends on the surroundings, especially on its geometry and reflectivity.

AGNES sites are continuously recording and are used to determine tectonic deformation processes. As the expected and measured deformation rates are small, local disturbances may introduce errors with a high relative impact on the estimation. Therefore, it is favorable to know the size of the multipath effects in order to judge the results.

Assuming that the multipath effects are remaining in the double-difference residuals it is possible to obtain the multipath for each station transforming the double-difference into zero-difference residuals. The used method is discussed in [Alber *et al.*, 2000] or [van der Marel and Gündlich, 2006].

### 2.4.1 Multipath estimation

This investigation has been worked out on one year of double-difference residuals from the AGNES processing in 2006. Based on these data the zero difference residuals have been derived using the algorithm described by [Alber *et al.*, 2000]. The used software to extract the zero-difference residuals was implemented by Dr. D. Perler at the GGL.

The transformation of double- into single- and the single- into zero-difference residual leads to under-determined systems. From  $n$  single-differences only  $n - 1$  independent double-differences can be built and the same problem occurs for the transformation of single- into zero-difference residuals. To solve the under-determined systems an additional condition has to be introduced. This constrain is the weighted zero-mean assumption. Two weighting functions have been used to extract the zero difference residuals from the double differences obtained from the processing run by swisstopo. The tropospheric estimation was done without including horizontal tropospheric gradients.

In a first step, single differences are created from the double differences. According to [Alber *et al.*, 2000] with  $dd$  as double difference phase observation,  $s$  as single difference, station  $A$  and  $B$ , satellite  $i$  and  $j$ ,  $\phi$  denoting the phase, the transformation reads:

$$s_i^{AB} = \phi_i^A - \phi_i^B \quad (2.6)$$

$$s_j^{AB} = \phi_j^A - \phi_j^B \quad (2.7)$$

$$dd_{ij}^{AB} = (\phi_i^A - \phi_i^B) - (\phi_j^A - \phi_j^B) = s_i^{AB} - s_j^{AB} \quad (2.8)$$

The building of the double differences can be written as a matrix product with the single differences  $\mathbf{s}$ , the double differences  $\mathbf{dd}$ , and the matrix  $\mathbf{D}$

$$\mathbf{Ds} = \mathbf{dd} \quad (2.9)$$

As for a single baseline only  $n-1$  linearly independent double differences can be built, the matrix  $\mathbf{D}$  cannot be inverted. Introducing a zero-mean assumption for each epoch as an additional constrain solves the problem:

$$\begin{pmatrix} 1 & -1 & 0 & 0 & \dots & 0 \\ 1 & 0 & -1 & 0 & \dots & 0 \\ \vdots & \vdots & \vdots & \vdots & \ddots & \vdots \\ \vdots & \vdots & \vdots & \vdots & \ddots & \vdots \\ w_1 & w_2 & \dots & w_n & & \end{pmatrix} \cdot \begin{pmatrix} s_1^{AB} \\ s_2^{AB} \\ \vdots \\ s_n^{AB} \end{pmatrix} = \begin{pmatrix} dd_{12}^{AB} \\ dd_{13}^{AB} \\ \vdots \\ dd_{1n}^{AB} \\ \sum w_i^{AB} s_i^{AB} \end{pmatrix} \quad (2.10)$$

with the zero mean assumption

$$\sum_i w_i^{AB} s_i^{AB} = 0. \quad (2.11)$$

Signals at low elevation travel through a longer path in the troposphere and are, therefore, more disturbed. The constraint can be improved by additionally down weighting single differences depending on the satellite elevation  $\epsilon$ . The used weighting function is:

$$w_i^{AB} = \frac{\sin(\epsilon_i^A)^2 \sin(\epsilon_i^B)^2}{2} \quad (2.12)$$

The next step is to obtain the zero differences  $z_i^A, z_i^B, z_j^A, z_j^B$  which are used to determine the path delay between the satellite  $i$  and the site  $A$ . This is formulated with a satellite-dependent matrix  $\mathbf{D}_i$ , the zero differences  $\mathbf{z}_i$  and the single differences  $\mathbf{s}_i$

$$\mathbf{D}_i \mathbf{z}_i = \mathbf{s}_i \quad (2.13)$$

with an additional constrain the equation is

$$\begin{pmatrix} 1 & -1 & 0 & 0 & \dots & 0 \\ 1 & 0 & -1 & 0 & \dots & 0 \\ \vdots & \vdots & \vdots & \vdots & \ddots & \vdots \\ \vdots & \vdots & \vdots & \vdots & \ddots & \vdots \\ w_A & w_B & \dots & w_Z & & \end{pmatrix} \cdot \begin{pmatrix} z_i^A \\ z_i^B \\ \vdots \\ z_i^Z \end{pmatrix} = \begin{pmatrix} s_i^{AB} \\ s_i^{AC} \\ \vdots \\ \sum_I w_i^I z_i^I \end{pmatrix} \quad (2.14)$$

The constrain can be improved introducing an elevation dependent weighting function:

$$w_i^I = \sin(\epsilon_i^I)^2 \quad (2.15)$$

To analyze the residuals, which are assumed to be caused by multipath, they are filled into equally spaced volume angle bins ( $5 \times 5$  degrees) covering a half sphere representing the sky. It is assumed that all signals arriving from identical directions have the same multipath delay as they are reflected by the same obstructions. Having more than one observation per bin gives more reliable results as the noise can be reduced by creating the mean delay, its standard deviation gives statistical information on the quality. Because of this, the chosen time span needs to include enough measurements covering the whole sky.

### 2.4.2 Results

Multipath analyses as described in the previous subsection have been applied to the AGNES stations. The analysed data covers the time period from 20 January 2006 to 5 May 2007. Yearly and monthly evaluation of the residuals have been done. The data covering one year gives an overall view of the influences caused by reflections. As the material properties influence the reflection, the effect depends also on the seasons. Sites at higher altitudes might be covered by snow during winter which decreases the absorption of the ground and therefore the reflected signals are stronger.

All available sites have been analysed. The sites of Zimmerwald, ETH Zurich, and Andermatt will be discussed in this chapter.

Figure 2.17 and 2.18 display the calculated multipath over one year for site ZIMM. The first plot shows the results without a specific mapping function whereas in the second figure the observations with low elevation have been down weighted using a squared sine function of the elevation. No specific pattern can be found in the results compared to the standard deviation. This may result from taking the average over a whole year. The ground reflections are influenced by the ground's cover such as snow in winter.

Figure 2.19, 2.20 and 2.21 show the results for the sites ZIMM, ANDE and ETHZ obtained over a two week period. Four different time periods are shown:

- Spring: 17.03.2006 – 30.03.2006
- Summer: 23.06.2006 – 06.07.2006
- Fall: 15.09.2006 – 28.09.2006
- Winter: 22.12.2006 – 04.01.2007

The analysis of the stations has been carried out in order to obtain a rough overview on the multipath effects. The applied approach did not reveal any stations with clear multipath effects. However, most of the stations had some spots with increased residuals. This might

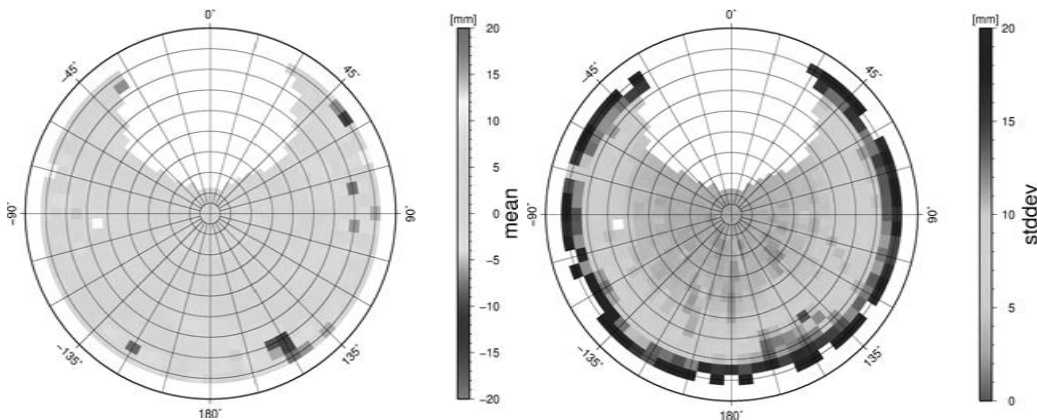


Figure 2.17: Average multipath of station ZIMM from 01.20.2006 – 01.19.2007.

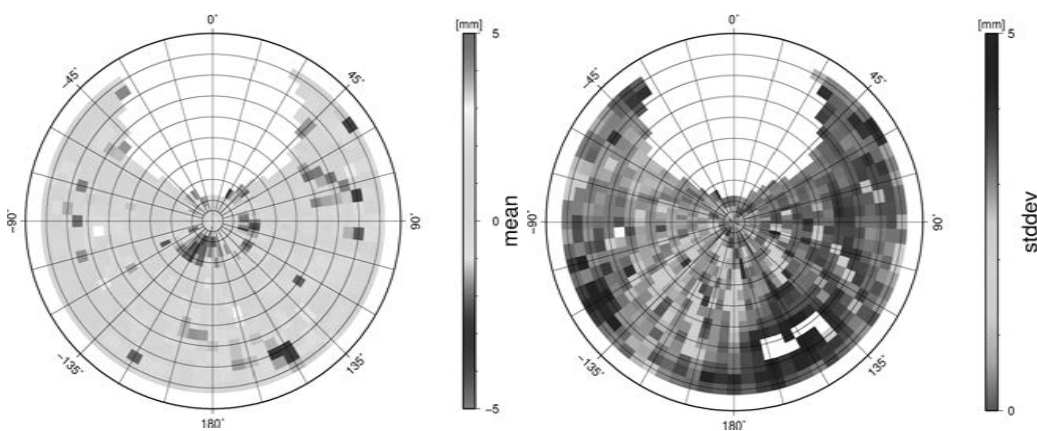
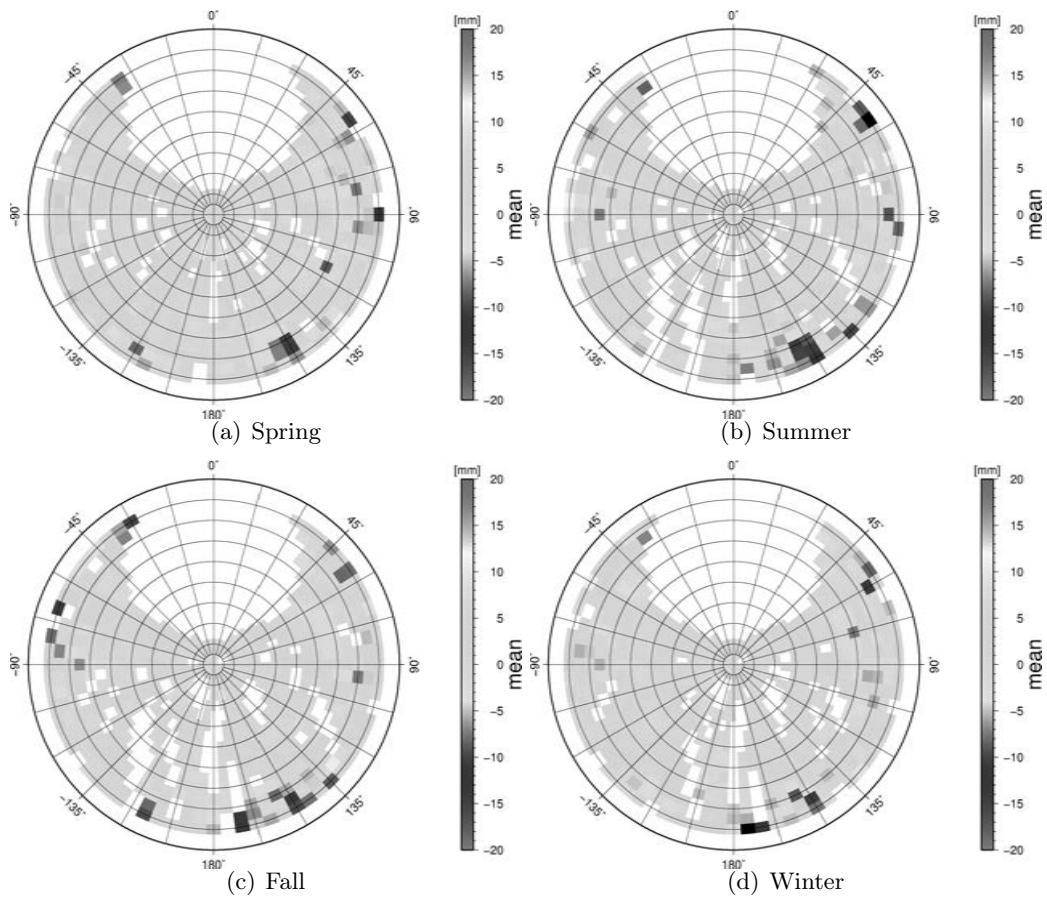


Figure 2.18: Average multipath of station ZIMM from 01.20.2006 – 01.19.2007 using the mapping function.

be caused by reflections. The increased residuals North of the ETHZ site might be caused by a tall building (azimut: ca. 40 degree, maximum elevation ca. 30 degrees)

## 2.5 Uplift rates from GNSS and levelling

The AGNES network can be used to detect the uplift motions of the individual sites [Brockmann et al., 2012, 2013]. Comparing the uplift rates with the values derived from levelling data reveals similar trends. The Alps are rising compared to the Swiss Molasse Basin and the Jura is subsiding. As both measurement methods use different reference points the absolute uplift rates cannot be compared directly. In order to estimate the offset caused by the different reference point the mean uplift rate of the AGNES sites, GNSS uplift and the interpolated uplift rates from the levelling data, was used and subtracted from the GNSS solution. The applied offset value is -0.95 millimetre per year. The uplift rates differ between both methods. Figure 2.22 and 2.23 display the levelling data (see Section 5.2.3) interpolated on a grid and the AGNES uplift rates. The rates are up to 1.5



**Figure 2.19:** Average multipath of station ZIMM for each season covering a time span of 2 weeks.

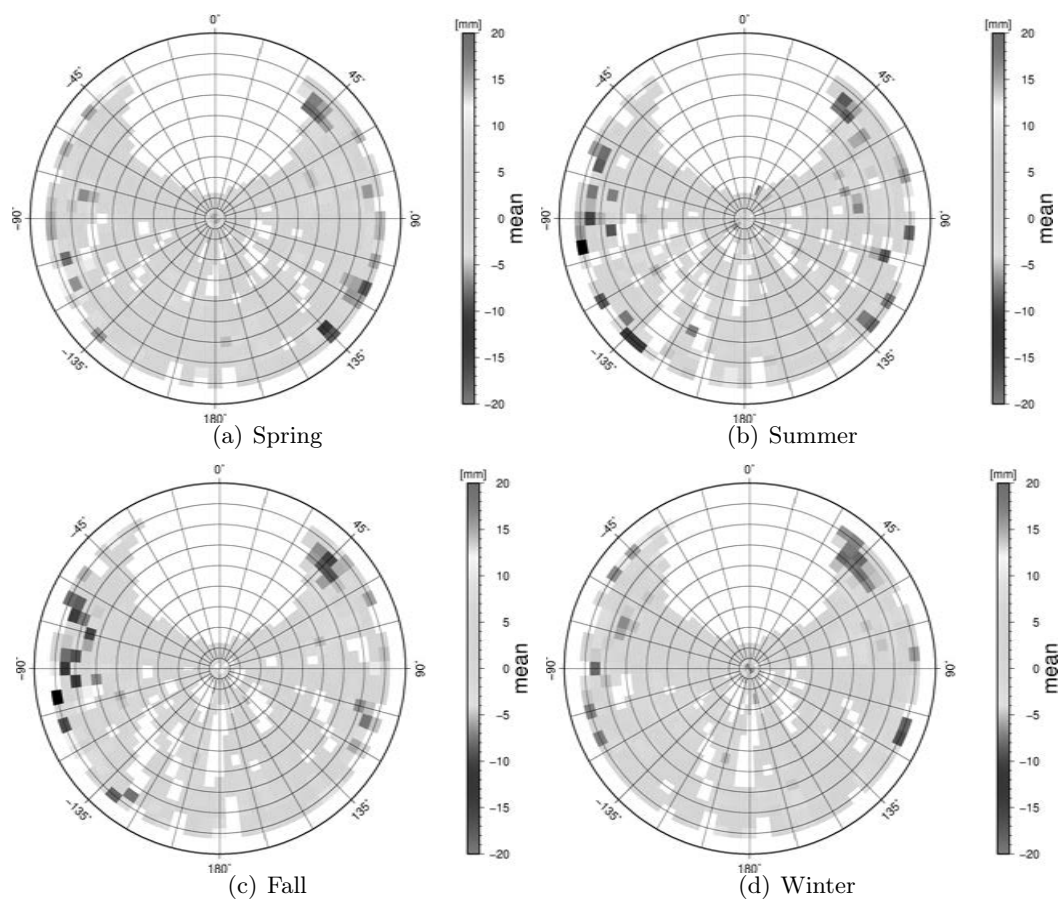


**Figure 2.20:** Average multipath of station ANDE for each season covering a time span of 2 weeks.

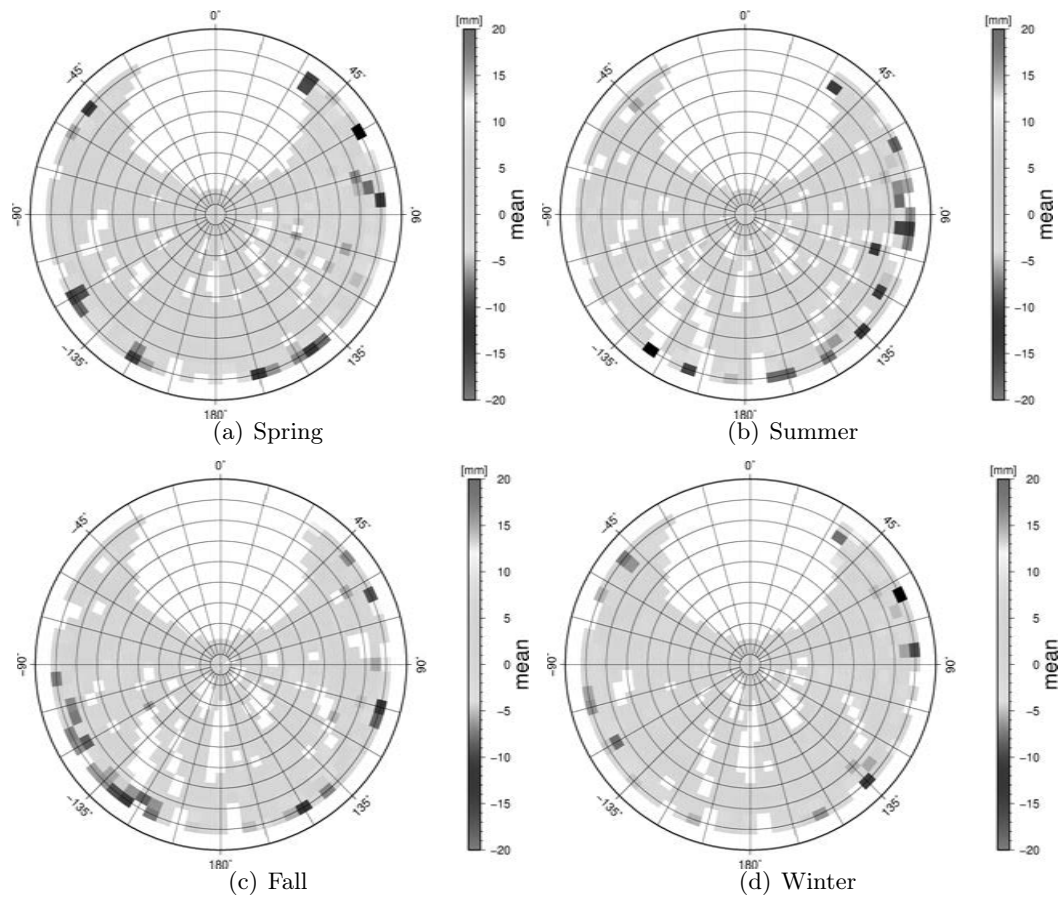


**Figure 2.21:** Average multipath of station ETHZ for each season covering a time span of 2 weeks.

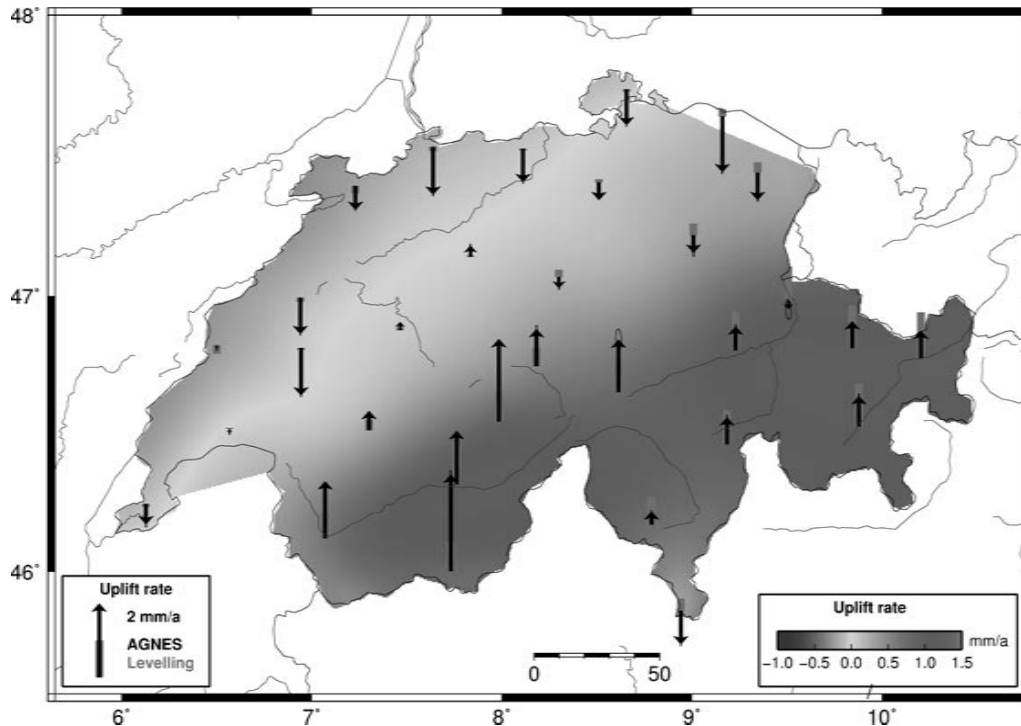


**Figure 2.22:** Comparison between the AGNES uplift rates and the interpolated rates from levelling data. The AGNES uplift rates are reduced by 0.95 millimetre per year in order to have the same mean value as the corresponding mean uplift from the interpolated levelling data.

millimetre per year for the levelling techniques. The GNSS sites have uplift velocities up to 4.5 mm / year. Figure 2.23 shows the difference between the GNSS uplift rates (offset removed) and the interpolated levelling rates. However, even though both methods show similar trends the absolute uplift rates from both methods differ and cannot be combined using only an offset and a for scale. Due to the longer time span covered and the higher point density the levelling data will be introduced as uplift measurements instead of the GNSS solution.

It is not clear what causes the difference between the two uplift rates. A possible cause are the different locations of the measured points. The levelling measurements are mainly performed in the valleys whereas the GNSS permanent stations are often located on the top of mountains in order to have an open sky. The uplift rates might differ between the valleys and mountains due to different tectonic setups.

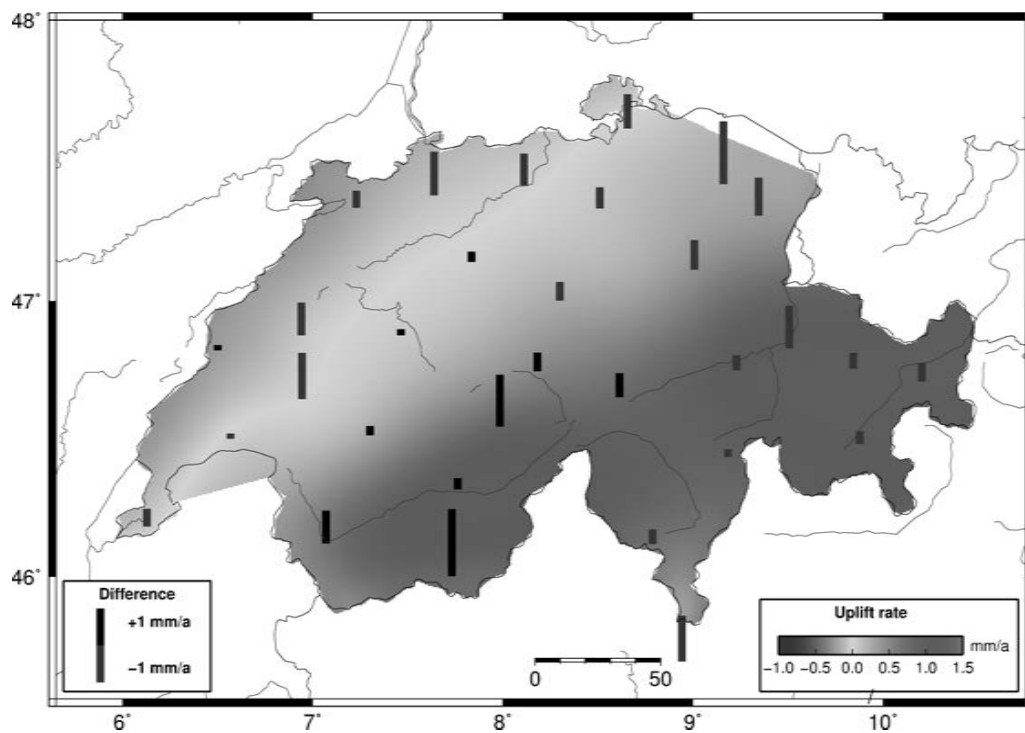


**Figure 2.23:** Difference between the interpolated uplift rates from leveling and the GNSS rate (GNSS-levelling). The AGNES velocities are reduced by 0.95 millimetre per year to have the same mean value for both uplift rates. The blue bar represents a negative and the black bar a positive offset.



## 3 Block detection

The collision between the Adriatic micro- and the Eurasian plate is an ongoing process. *Calais et al.* [2002] estimated the rotation pole of the Adriatic micro-plate with respect to the European plate (see Section 1.3). The corresponding horizontal velocities along the Alpine front are around one millimetre per year. Therefore, the velocities within Switzerland, relative to Zimmerwald located in the Swiss Molasse Basin, are expected to be mostly below 1 millimetre per year.

The local influences may have the same order of magnitude as the tectonically driven displacements. The extraction of the tectonic part from noisy data sets requires a physical or mathematical model to define the correlation between two points. The simplest model is defining rigid blocks for areas with similar tectonic structures. The deformation within such blocks is neglected and the remaining residuals are assumed to originate from local disturbances or noise. The block definition is the major challenge in this approach. The boundaries can either be defined based on geological maps or automatically extracted from measurements using an iterative approach.

The results of the CHTRF 2010 campaign were not available at the time when these studies were made. Therefore, the data source for the analysis is the AGNES network. It consists of 30 permanent GNSS sites in Switzerland with their positions, velocities, and formal errors. The automatic block detection was later, after the release of the CHTRF 2010 solution, also applied to the results of the CHTRF 2010 campaign.

### 3.1 Automatic block detection using a genetic algorithm

#### 3.1.1 Introduction

The problem of automatic block detection is the large number of possible solutions. For example, dividing 25 sites into 3 blocks leads to  $S(25, 3) = 1.4 \cdot 10^{11}$  possible block setups, where  $S$  stands for the 2nd order Stirling number. The straight forward way is to evaluate all possible constellations and compare their results. A more sophisticated approach is using the genetic algorithm method to obtain the best solution without the need to evaluate all of them. The method is briefly introduced in this section. More detailed information may be obtained from [Vose, 1999] which describes the simple genetic algorithm.

The automatic block determination should lead to the best possible block definition ful-

filling a given condition. This condition is, for the block detection purpose, minimising the weighted residuals remaining after the block velocity estimation. The method searches for a specific set of values, called genes, minimising the given criterion function. The genes represent the block definitions and the minimising function is given by the posterior precision of the block motion estimation.

The blocks are defined as 2-dimensional rigid structures. The motion is described by an angular velocity ( $\omega$ ), centre of rotation ( $X$ ), and a translation ( $v$ ). The problem has three degrees of freedom. Therefore, the origin of the rotation can be fixed to an arbitrary value. It is defined as the barycentre of each block. The velocity  $v_i$  of a point belonging to the block is

$$v_i = \omega \times (X_i - X) + v \quad (3.1)$$

with

$$\omega = (0, 0, \omega)^T \quad (3.2)$$

The basic idea behind the genetic algorithm comes from the evolution theory. The applied procedure, implemented in the software R [R Development Core Team, 2009], is visualized in the flowchart shown in Figure 3.1. A set of several genes, in this case a set of block definitions, is generated randomly and analysed estimating their weighting function (function to be minimised). Half of the analysed sets is taken directly into the next iteration. The other half of the sets are randomly modified, either by randomly changing the block of individual sites or by merging two block definitions into one. The selection of blocks to be taken into the next step or to be modified, is a random process giving block definitions with a better fitting value a higher chance to get selected. The rating is based on the criterion function which is to be minimised. For the block detection the value to be minimised is the RMS of the block velocity estimation. At the long term the fittest ones survive and the weighting function gets minimised. The process is repeated until a given limit or the maximum number of iterations is reached. For our purpose only the maximum allowed amount of iterations is set.

### 3.1.2 Test field

The test field contains three blocks with 25 points distributed over the three fields as input data. The velocity of each point is a combination of its corresponding block velocity and a white noise part. There are  $1.4 \cdot 10^{11}$  possible block constellations which should be tested to obtain the best fitting solution. The block extraction is achieved using the genetic algorithm with 150 iterations. The sample consists of 100 randomly initialized genes. During the process  $150 \cdot 100 = 1.5 \cdot 10^4$  individual estimations are calculated compared to the totally possible  $1.4 \cdot 10^{11}$  setups. This is a factor of  $10^8$  between the total of all possible and calculated constellations.

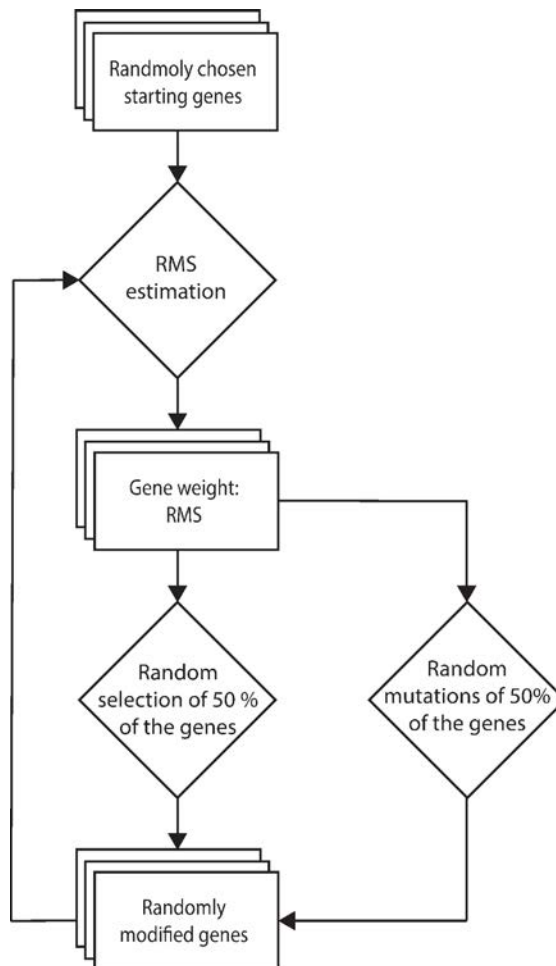


**Figure 3.1:** Flowchart of the implemented genetic algorithm. The random selection process is based on the gene weight where genes with a better RMS have a higher probability to get chosen.

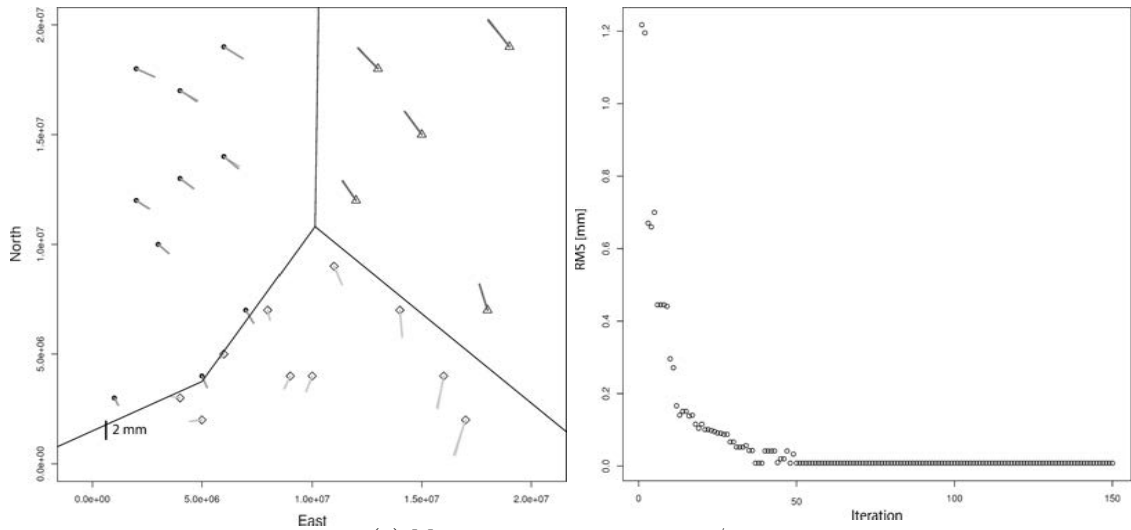
Figure 3.2 shows the test field with the three blocks. The average velocity for an individual point is 1.8 and the accuracy is  $\sigma=0.1$  millimetre per year. The algorithm divides the points into three blocks which is identical with the original setup. Therefore, no mismatch has occurred. The conditions are ideal due to the clear block boundaries and the high accuracy compared to the velocities. The optimal block identification is reached after 50 iterations after which no further improvement is achieved. If the accuracy of the input data is in the same order as the input velocities the detection algorithms gets unstable.

### 3.1.3 Application to the AGNES network

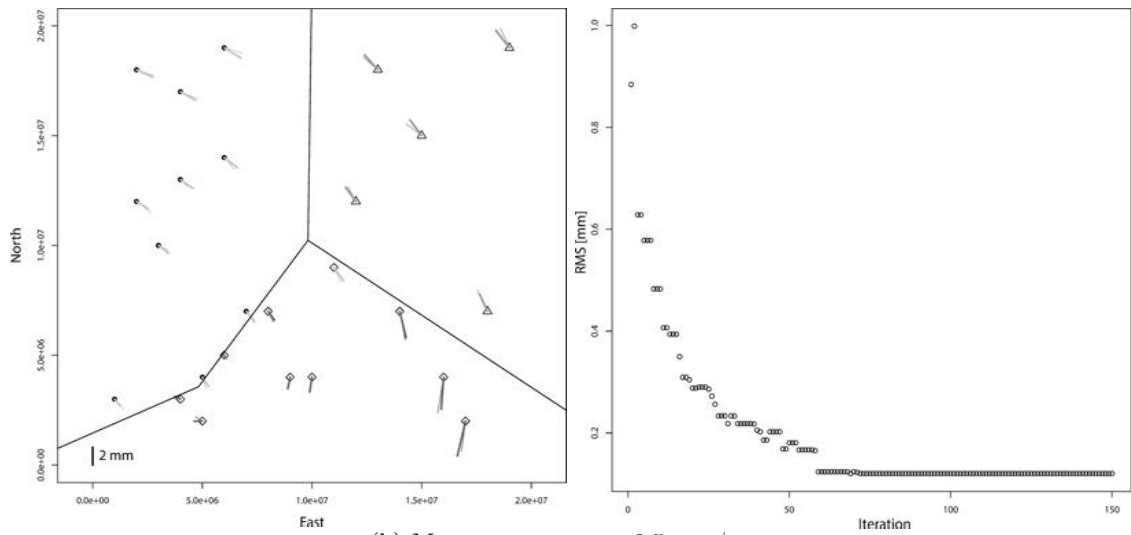
The results of the test field show that the method is capable to retrieve the created blocks if the noise level is below the tectonic velocities. The AGNES network delivers a real test data set to validate the implemented method. The velocities are, compared to the test field, much noisier, may contain local influences, and do include unmodeled intra-plate deformations. The outcome of the block detection does not have clear structures. The reasons are the previously mentioned problems and neglect of intra-plate deformation. Figure 3.3 shows the detected blocks (ZERM, SARG have been previously eliminated because the velocities indicate clear non-tectonic influences). The algorithm finds an optimal block setup but the definitions do not represent a meaningful solution. The points of one block are spread over the whole area and may not have a direct connection to the rest of the block. To get a better estimation, one has to introduce topological information using a triangulation or similar method. *Danuser et al.* [1993] describes such a system using neighbouring information to extract coherent blocks. A manual approach to solve the block building problem is to define them using geological information and then estimate their velocities.

The introduction of topological information and forcing the algorithm to build blocks where the points are connected by the given topology will ensure coherent results. The definition of the topological setup is done with the Delaunay triangulation which defines the neighbouring conditions. All points within a block have to be connected by one edge of the triangulation. Due to the neighbouring condition the merging of two setups into one was removed.

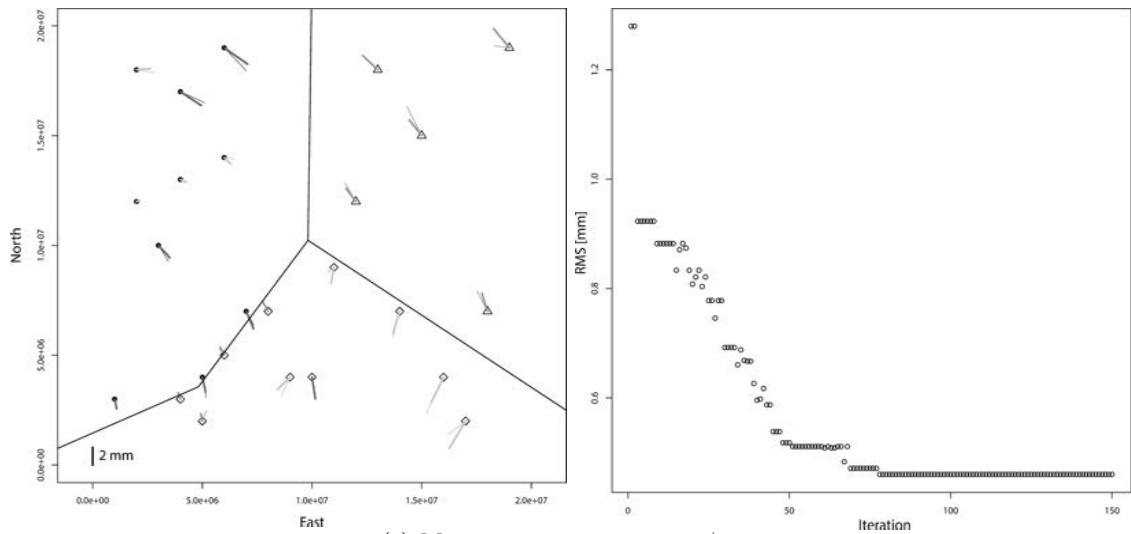
The enhanced method leads to a major improvement. Figure 3.4 shows the new block definition and Figure 3.5 the RMS resulting after each iteration. The blocks represent, to some extent, reasonable definitions. The Swiss Molasse Basin is divided into two blocks and separated from the alpine region. The western block (triangles) contains points in various tectonic structures. This might not represent a true constellation and only be a result of noise and local influences. Therefore, manual block definition might bring a better solution for the AGNES network.



(a) Measurement error: 0.1 mm/year



(b) Measurement error: 0.5 mm/year



(c) Measurement error: 1 mm/year

**Figure 3.2:** Block detection for a test field using a genetic algorithm. Left: Test field with the detected blocks. Right: RMS of the best block solution after each iteration.

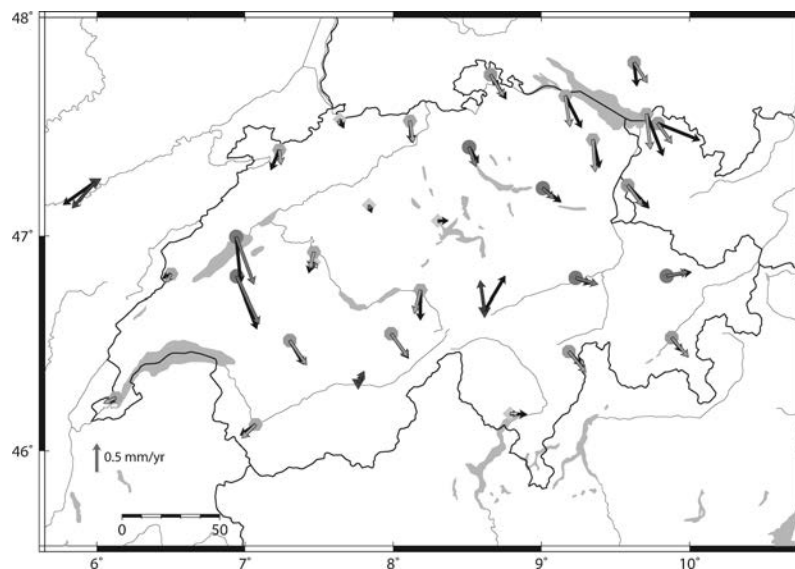


**Figure 3.3:** Estimation of five blocks within the velocity field of the AGNES stations. The black arrows are the original velocities whereas the coloured ones represent the estimated values.

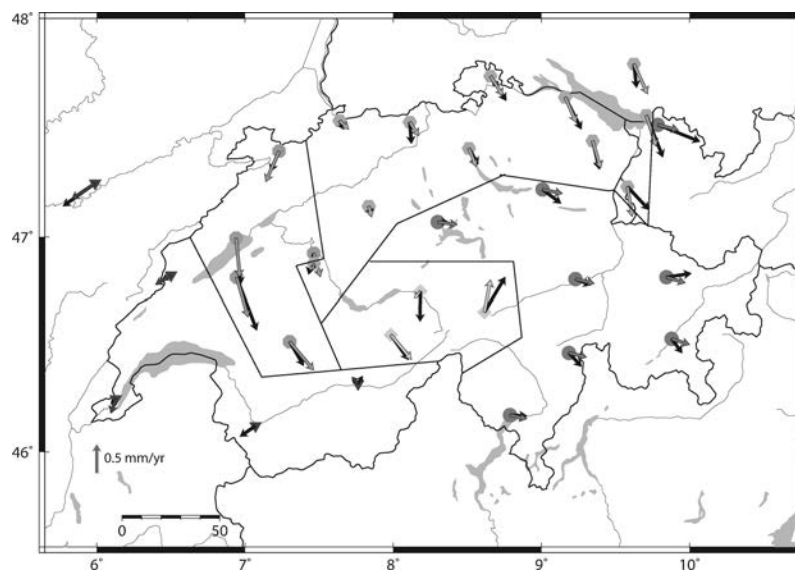


**Figure 3.4:** Genetic algorithm using Delaunay triangulation to force all points within one block to be connected: Estimation of five blocks within the velocity field of the AGNES stations. The measured velocities are black and the estimated block velocities are coloured.

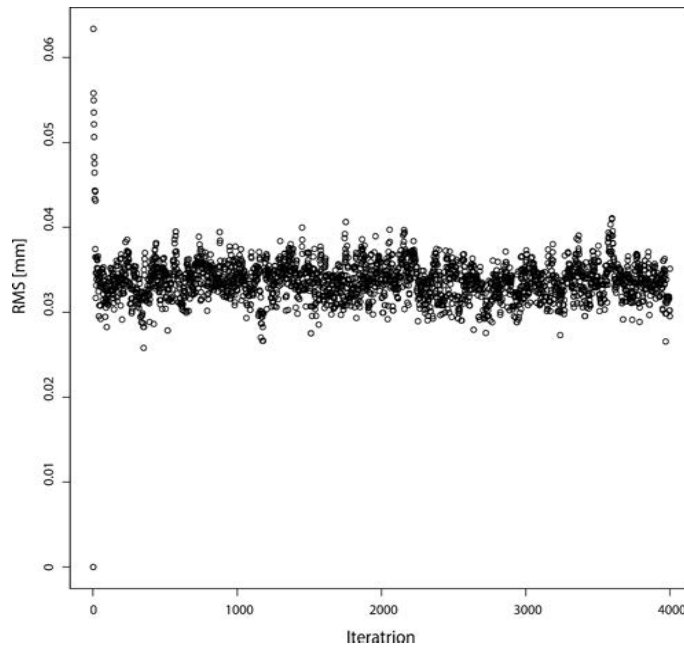


**Figure 3.5:** Genetic algorithm using Delaunay triangulation to force all points within one block to be connected: Estimation of five blocks within the velocity field of the AGNES stations. The lowest root mean square of the least-squares estimation after each iteration.

### 3.1.4 Application to the CHTRF 2010

After the GNSS campaign in 2010, carried out by swisstopo, the CHTRF 2010 solution is divided into 8 blocks using the genetic algorithm. The neighboring condition was constrained introducing the Delaunay triangulation. The algorithm consists of 4000 iterations and 150 genes. The advancement after each iteration became small after the first few iterations (Figure 3.7). The best solution, shown in Figure 3.6, has some reasonable block definitions. The Jura (diamonds) was separated from the Swiss Molasse Basin (triangles) in the eastern part but contains the western part and the canton Valais. However, the block model is too simplified as no clear borders exist. Using collocation techniques might lead to a better and more reliable interpretation of the ongoing plate tectonics.

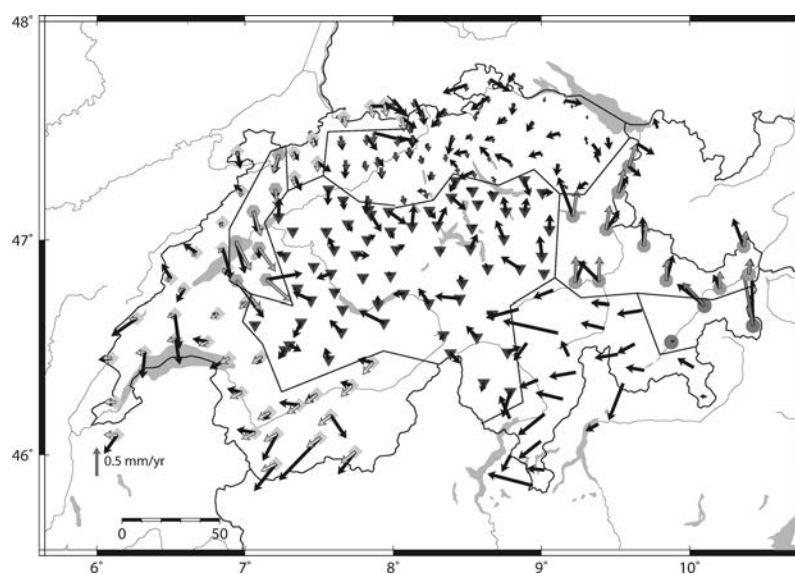


**Figure 3.6:** Genetic Algorithm using Delaunay triangulation to force all points within one block to be connected: Estimation of 8 blocks within the velocity field of the CHTRF 2010 points. The black arrows represent the original velocities whereas the coloured ones denote the estimated values.

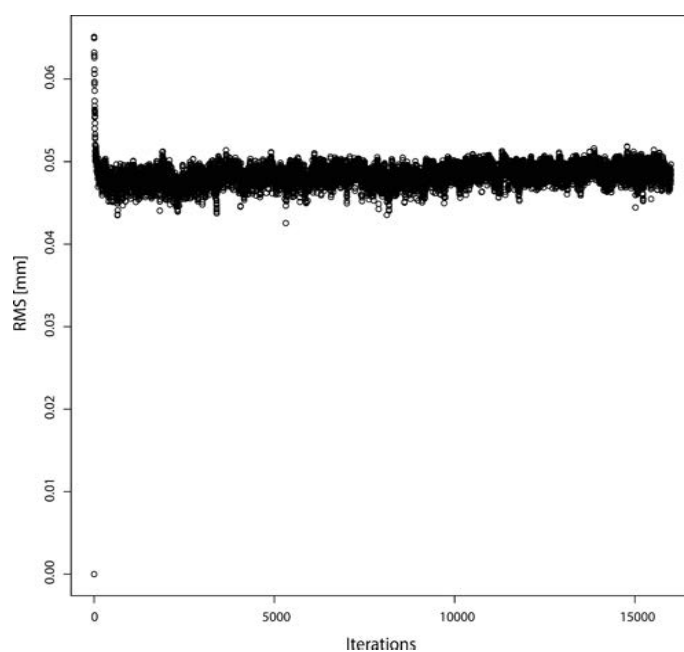


**Figure 3.7:** Genetic Algorithm using Delaunay triangulation to force all points within one block to be connected. The lowest root mean square of the least-squares estimation after each iteration.

## 3.2 Manual block definition based on geological information

### 3.2.1 Introduction

As mentioned in Section 3.1 it is difficult to extract realistic block definitions using genetic algorithms. A more intuitive approach is to define the blocks manually based on the tectonic setup. Within Switzerland, swisstopo releases tectonic and geological maps in various scales (1:25000, 1:300000) covering the whole country. The 1:25000 maps are very detailed and not used to define the block borders. A smaller scale map with a simplified tectonic setting is used instead to define areas with similar behaviour. The five blocks cover the following areas:

- I Jura
- II Swiss Molasse Basin
- III Prealps
- IV Alps
- V Wildstrubel area (*Project TECVAL, see Chapter 7*)

The block rotations are estimated in the same way as in the automatic mode, assuming the blocks to be solid structures. The horizontal block rotation is described by five components: a rotation, arbitrary chosen origin of rotation, and a translation. Therefore, only three unknowns remains to be estimated. Deformations within a structure are neglected. The estimation of the three unknowns ( $\omega, v_x, v_y$ ) is achieved using a robust approach with the mean position ( $X$  and  $Y$ ) of all sites within the block as the origin of rotation. The rotation and translations are calculated by a least-squares estimation using the robust method described by [Baarda, 1968] analysing the residuals with respect to their accuracy and reducing the weight of points which are above the 95% significance level (data-snooping).

### 3.2.2 AGNES: Horizontal components

Arranging the AGNES stations to five tectonic structures and estimating their rotations leads to the block rotations listed in Table 3.1. The original and estimated velocity for each site are shown in Figure 3.8. The residuals, also visible in Figure 3.8, indicate a different behaviour between the eastern and western part of the Swiss Molasse Basin. Therefore, block II is divided into two parts to account for the different behaviour. Additionally, a few sites show huge residuals compared to their corresponding block velocities. This may be caused by local influences.

The second block definition splits block II (Swiss Molasse Basin) into an eastern and a western part. The corresponding velocities are shown in Table 3.2 and displayed in Figure 3.9. The western part is not as homogeneous as the eastern part.

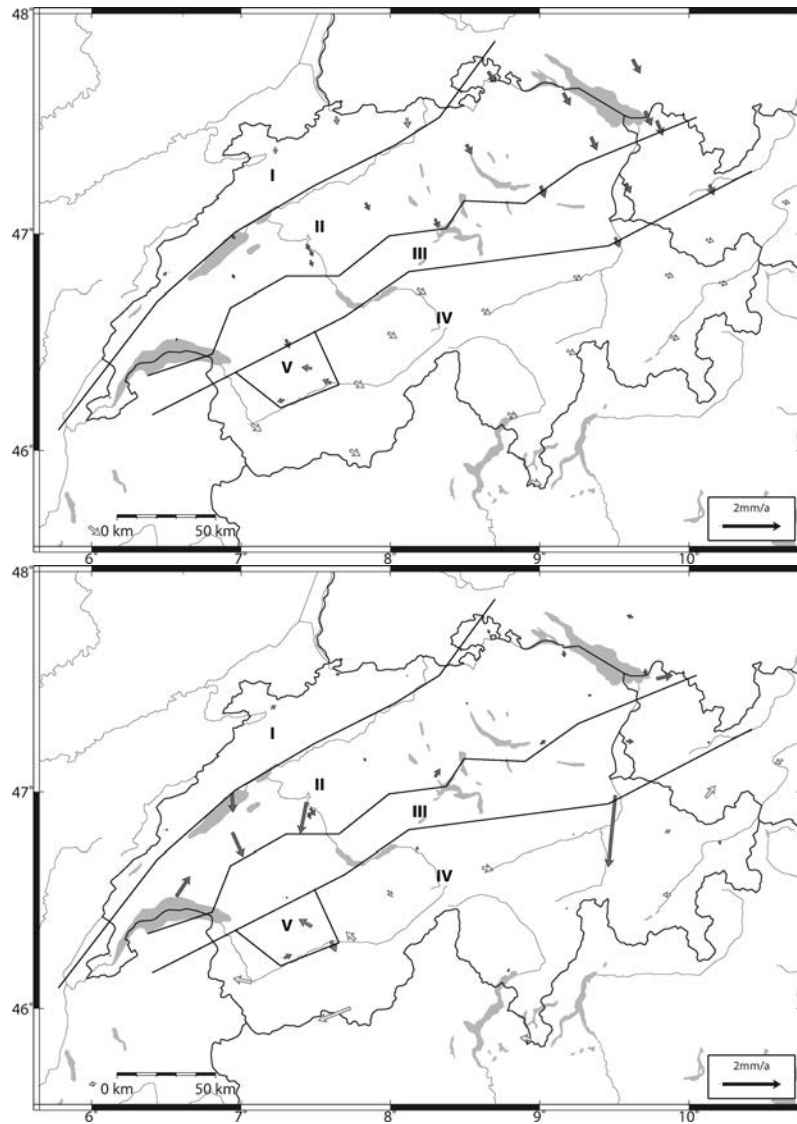


**Figure 3.8:** Horizontal block velocities (upper) and residuals (lower) using 5 blocks.

**Table 3.1:** Block rotation parameters using 5 blocks calculated in the LV03 system.

Block	Origin of rotation		Trans Y	Trans X	Rot Z-axis
	Y: km	X: km	mm/a	mm/a	arcsec/a
I	594	241	$-0.01 \pm 0.04$	$-0.24 \pm 0.04$	$0.39 \pm 0.16$
II	661	262	$0.14 \pm 0.03$	$-0.30 \pm 0.04$	$0.36 \pm 0.08$
III	701	148	$0.30 \pm 0.05$	$-0.15 \pm 0.05$	$-0.15 \pm 0.10$
IV	728	206	$0.14 \pm 0.07$	$-0.33 \pm 0.08$	$0.05 \pm 0.17$
V	601	129	$-0.28 \pm 0.17$	$0.03 \pm 0.17$	$-1.33 \pm 2.88$

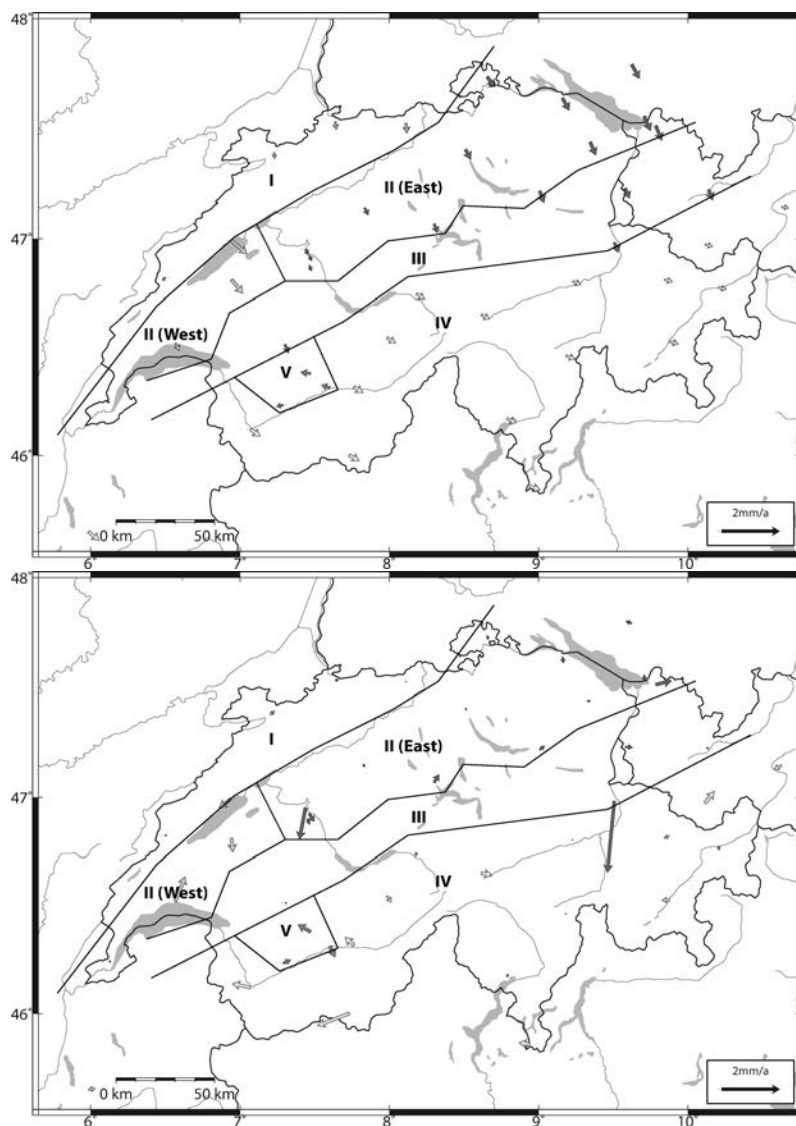


**Figure 3.9:** Horizontal block velocities (upper) and residuals (lower) using 6 blocks.

**Table 3.2:** Block rotation parameters with an eastern and western part of the Swiss Molasse Basin calculated in the LV03 system.

Block	Origin of rotation		Trans Y	Trans X	Rot Z-axis
	Y: km	X: km	mm/a	mm/a	arcsec/a
I	594	241	$-0.01 \pm 0.04$	$-0.24 \pm 0.04$	$0.39 \pm 0.16$
II (West)	690	243	$0.16 \pm 0.04$	$-0.35 \pm 0.38$	$0.12 \pm 1.09$
II (East)	539	166	$0.25 \pm 0.21$	$-0.30 \pm 0.21$	$1.60 \pm 1.04$
III	701	148	$0.30 \pm 0.05$	$-0.15 \pm 0.05$	$-0.15 \pm 0.10$
IV	728	206	$0.138 \pm 0.07$	$-0.33 \pm 0.08$	$0.06 \pm 0.17$
V	601	129	$-0.28 \pm 0.17$	$0.03 \pm 0.17$	$-1.33 \pm 2.88$

**Table 3.3:** Vertical block velocities using 4 blocks (Molasse Basin is one block) calculated in the LV03 system.

Block	Origin of rotation		Trans Z mm/a	Rot X-axis arcsec/a	Rot Y-axis arcsec/a
	Y: km	X: km			
I	588	234	$0.38 \pm 0.01$	$2.09 \pm 0.21$	$0.35 \pm 0.16$
II	661	226	$1.04 \pm 0.06$	$1.74 \pm 0.69$	$0.83 \pm 0.38$
III	701	148	$2.29 \pm 0.14$	$-0.85 \pm 0.92$	$-1.90 \pm 0.48$
IV	728	206	$1.45 \pm 0.01$	$-2.10 \pm 0.19$	$-0.90 \pm 0.08$

### 3.2.3 AGNES: Uplift component

Similar block definitions as for the horizontal deformations are introduced for the vertical component. The block motions for the uplift values are described by one translation and two rotations about the x- and y- axis of the coordinate system (LV 03). Compared to the last block definition for the horizontal case some minor changes are applied. Region Wildstrubel has not been used because the time series of the stations situated on this block are too short and the Swiss Molasse Basin is combined to one block. This definition leads to the translation and rotations listed in Table 3.3. The calculated uplift velocities for the sites and the remaining residuals are shown in Figure 3.10. The uplift components can be much better modeled by the introduced blocks than the horizontal components. It becomes clear that the Jura is subsiding with respect to the Swiss Molasse Basin and that the Alps are rising. Levelling data leads to the same conclusions [Schlatter, 2005].

## 3.3 Conclusion

The automatic block detection without the consideration of the neighbourhood has failed to build realistic blocks. The main problem is the relatively high noise level in the velocity values; both have similar magnitudes. The introduction of a Delaunay triangulation defining the topology led to a major improvement. The resulting block definitions do only match to a certain extend with the tectonic structures. Because of this, the manual block determination is to be preferred over the automatically generated solution. However, the models do not support any intra-plate deformation. To account for intra-plate deformations a least-squares collocation method is introduced. Using an adaptive version of collocation, described in the next chapter, changing the correlation between points depending on the strain field mapping the tectonic structures autonomously.

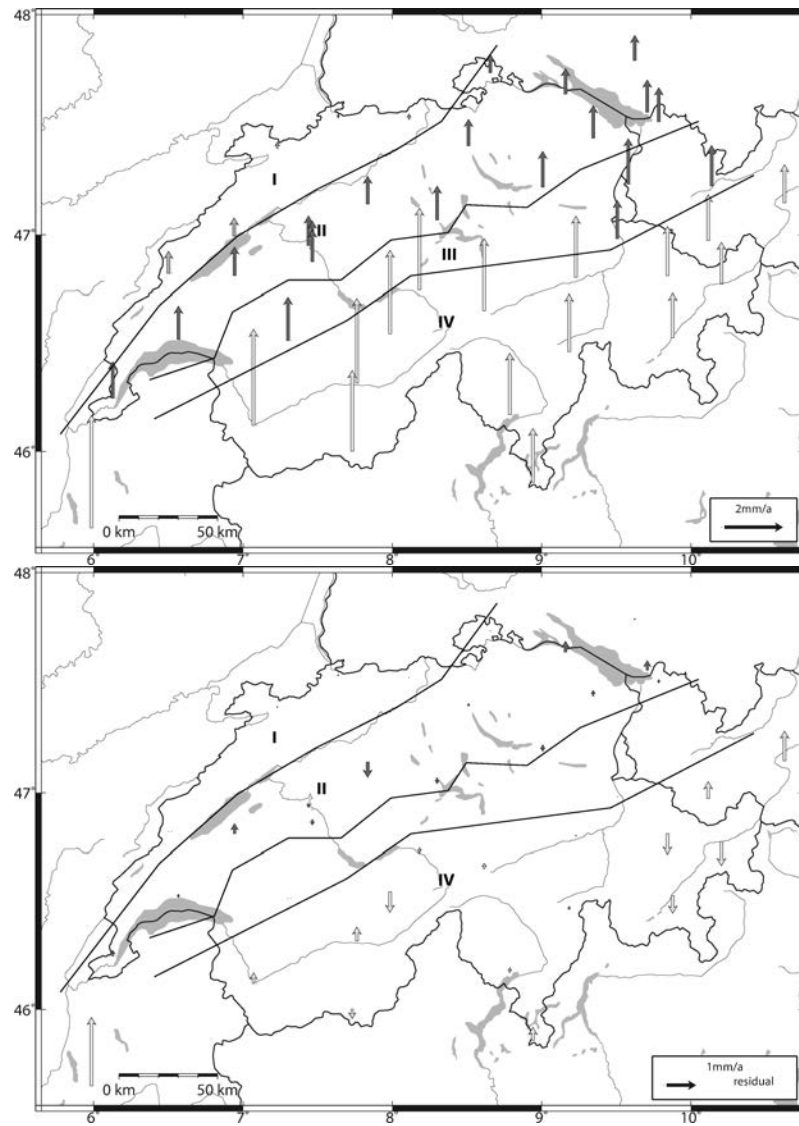


**Figure 3.10:** Uplift rates (upper) and residuals (lower) using 4 blocks.



## 4 Adaptive least-squares collocation: Theory

The extraction of a kinematic field based on point measurements, such as GNSS and levelling, can be achieved by interpolation methods. However, the interpolation techniques have to deal with uncertainties and need to be suitable for the given problem. Such a tool is the Least-Squares Collocation (LSC) technique described in [Moritz, 1970]. It is successfully applied to various geophysical problems such as potential anomalies and the extraction of tectonic movements. The method has been applied to derive the deformation and strain rate field, based on GNSS measurements, in Greece and Switzerland [Hollenstein, 2007; Egli et al., 2007; Peter, 2000; Kahle et al., 1995].

The FME technique, using a tectonic 3-D model of the crust, simulates the deformation process. This technique needs apart of the model also other input parameters such as the boundary conditions (velocities) and the rheology. The parameters can then be optimized by comparing the results with the measured deformations in order to obtain the best possible fit [Heidbach and Drewes, 2003; Bauchau and Craig, 2009; Müller et al., 2013]. However, this technique requires a simplified model of the crust and existing faults.

In the project Swiss-4D [Egli, 2004], the collocation technique was successfully applied to GNSS campaign-type data and levelling measurements. The technique was extended to the Adaptive Least-Squares Collocation (ALSC) method in order to map the tectonic setup based on the input data itself. This is achieved by reducing the correlation between points, where high strain rates are observed, leading to an inhomogeneous trend metric. The correlation between points is given by a function based on the point distance and predefined parameters describing the maximum correlation and the de-correlation factor with increasing distance. Deforming the metric used to measure the distance allows to de-correlate points by increasing their distance which is used in the correlation function. The deformation process is driven by the strain rate field which defines the deformation rates. Regions with high strain rates have a higher deformation contribution to the process than regions with low strain rates. With this approach, the deformation process is only based on the measurements without any information on tectonic structures such as plate boundaries or faults. The method is improved in order to extract a more reliable and coherent deformation field compared to the version used in [Egli et al., 2007]. The major improvements are the handling of different measurement types (levelling and GNSS) and the introduction of one trend metric for all three components allowing to process them simultaneously.

The movement of the measured points is a combination of tectonic movements, local influences, and seasonal effects. The expected deformation rates for Switzerland are between 0 and 25 nanostrain per year. Other influences may have a similar order of magnitude. The source of such disturbances are, among others, monumentation instabilities or land slides. For this purpose, the collocation technique is expanded by an additional stochastic model with a short correlation length. The first stochastic process, with a long correlation length, defines the geodynamic motion. The second part represents local influences and has therefore a smaller correlation length.

## 4.1 Theory

*Egli* [2004] introduced the ALSC approach. During this work the algorithm was enhanced in order to extract a full 3-D tensor from the measurements in one step. The Sections 4.1, 4.2, and 4.3 are based on the description made by [*Egli*, 2004] adding the 3-D functionality. After [*Egli et al.*, 2007], the general solution for the least-squares collocation with the interpolated value  $\hat{\mathbf{x}}$ , covariance function  $X$ , point coordinate  $\mathbf{r}$ , and the measured value  $\mathbf{x}(\mathbf{r}_k)$  at point  $\mathbf{r}$  is

$$\hat{\mathbf{x}}(\mathbf{r}) = \sum_{k=1}^N \lambda_k(\mathbf{r}, \mathbf{r}_k) \mathbf{x}(\mathbf{r}_k) \quad (4.1)$$

under rotational invariance when

$$\lambda_k(\mathbf{r}, \mathbf{r}_k) = \sum_{j=1}^N X(\mathbf{r}, \mathbf{r}_k) X^{-1}(\mathbf{r}_j, \mathbf{r}_k). \quad (4.2)$$

The classical LSC solution is

$$\hat{\mathbf{x}} = \mathbf{C}_{\hat{\mathbf{x}}\mathbf{x}} \mathbf{C}_{\mathbf{x}\mathbf{x}}^{-1} \mathbf{x} \quad (4.3)$$

for the interpolated field  $\hat{\mathbf{x}}$  at the prediction points  $\mathbf{p}_i$  with the covariance matrices  $[\mathbf{C}_{\mathbf{x}\mathbf{x}}]_{kj} = X(\mathbf{r}_k, \mathbf{r}_j)$  and  $[\mathbf{C}_{\hat{\mathbf{x}}\mathbf{x}}]_{ij} = X(\mathbf{p}_i, \mathbf{r}_j)$ .

The estimation of the covariance matrix is solved with Moritz's stochastic approach [*Moritz*, 1970] dividing  $\mathbf{x}$  into a deterministic part  $\mathbf{t}$ , further referenced as trend function, a stochastic part  $\mathbf{s}$ , called signal, and an observation error  $\mathbf{n}$ . The predicted values  $\hat{\mathbf{x}}$  can be divided into a trend part  $\hat{\mathbf{t}}$  and a signal  $\hat{\mathbf{s}}$ .

This leads, with the signal correlation matrix  $\mathbf{C}_{ss}$ , the signal covariance matrix between predicted and measured points  $\mathbf{C}_{\hat{\mathbf{s}}\mathbf{s}}$ , and the covariance matrix  $\mathbf{C}_{nn}$ , to

$$\hat{\mathbf{x}} = \mathbf{t} + \mathbf{C}_{\hat{\mathbf{s}}\mathbf{s}} (\mathbf{C}_{ss} + \mathbf{C}_{nn})^{-1} (\mathbf{x} - \mathbf{t}) \quad (4.4)$$

where the trend  $\mathbf{t}$  is defined by an a priori model representing the known tectonic setup. The deterministic part is usually given by physical laws or an empirically fitting model.

Therefore, the trend calculation is approximative and the signal not strictly stochastic as it includes trend errors. A simple model to describe the deterministic trend is a block model where each point is assigned to one specific tectonic structure. The blocks are introduced with physical properties describing their behavior. This can be the property of a solid structure with no intra-plate deformation. This method has been applied in several areas with clear tectonic boundaries [McClusky *et al.*, 2001; Chen *et al.*, 2004].

The separation into tectonic structures is not possible if no or insufficient information on the tectonic setup is known. Therefore, the block model is not feasible for such a setup. As the trend function is a non-stochastic process the covariance functions are inhomogeneous [Rummel and Schwarz, 1977] and anisotropic [Morrison, 1977]. Therefore, the ALSC approach introduces a inhomogeneous and anisotropic covariance function  $T(\mathbf{r}_A, \mathbf{r}_B)$  for the trend  $t(\mathbf{r})$ .

Including the additional stochastic process into the least-squares inversion leads to Equations (4.5) and (4.6). The trend covariance matrix between measured points is  $\mathbf{C}_{tt}$  and between prediction and measures points  $\mathbf{C}_{\hat{t}t}$ . Even though no deterministic part is used in the following description of the ALSC process, it can be included in a straight-forward way.

$$\hat{\mathbf{t}} = \mathbf{C}_{\hat{t}t}(\mathbf{C}_{tt} + \mathbf{C}_{ss} + \mathbf{C}_{nn})^{-1}\mathbf{x} \quad (4.5)$$

$$\hat{\mathbf{s}} = \mathbf{C}_{\hat{s}s}(\mathbf{C}_{tt} + \mathbf{C}_{ss} + \mathbf{C}_{nn})^{-1}\mathbf{x} \quad (4.6)$$

The derivative of the trend velocity is

$$\nabla\hat{\mathbf{t}} = (\nabla\mathbf{C}_{\hat{t}t})(\mathbf{C}_{tt} + \mathbf{C}_{ss} + \mathbf{C}_{nn})^{-1}\mathbf{x}. \quad (4.7)$$

The trend model represents the field characteristics based on their local deformation rates by deforming the used metric leading to inhomogeneous and anisotropic covariance function. Along plate boundaries the strain rates are assumed to be higher than in intra-plate areas. Therefore, strain rates are used as an indicator for de-correlation in areas with high deformation rates.

The trend correlation function  $T(\mathbf{r}_i, \mathbf{r}_j)$  is

$$T(\mathbf{r}_i, \mathbf{r}_j) = \sigma_t^2 f(|\mathbf{r}_i - \mathbf{r}_j|, r_t) \quad (4.8)$$

with the trend variance  $\sigma_t^2$  and correlation length  $r_t$  fulfilling following criteria:

- $f(r) \geq 0$  is a positive, monotonically decreasing function of  $r \geq 0$  with  $f(0) = 1$
- $\lim_{r \rightarrow \infty} f(r) = 0$
- $f'(0) = 0$

The deformation field is described by the covariance function using Equation (4.8). The correlation function has to be adapted to map the current tectonic features. The adaption of the trend correlation is achieved iteratively using the strain rate field as an indicator for de-correlation. In each iteration step the trend metric, in which the point distance  $r$  is measured for the correlation function, is deformed based on the strain rate field.

The  $k$ -th iteration is given by

$$T^k(\mathbf{r}_i, \mathbf{r}_j) = \sigma_t^2 f(|\mathbf{r}_i^{(k-1)} - \mathbf{r}_j^{(k-1)}|, r_t^k) \quad (4.9)$$

$$S(\mathbf{r}_i, \mathbf{r}_j) = \sigma_s^2 f(|\mathbf{r}_i - \mathbf{r}_j|, r_s) \quad (4.10)$$

using the dilatation process, described in the next section, to alter the trend metric. The signal correlation function is defined by two parameters, the signal variance  $\sigma_s$  and correlation length  $r_s$ , it remains homogeneous and is not affected by the dilatation process. The correlation function  $S(\mathbf{r}_i, \mathbf{r}_j)$  and  $T^k(\mathbf{r}_i, \mathbf{r}_j)$  between two points  $\mathbf{r}_i$  and  $\mathbf{r}_j$  depend on their distance  $r_{ij}$  and are defined as following

$$T(\mathbf{r}_i, \mathbf{r}_j) = \sigma_t^2 \cdot \left( \frac{r_t^2}{(r_t^2 + r_{ij}^2)} \right) \quad (4.11)$$

$$S(\mathbf{r}_i, \mathbf{r}_j) = \sigma_s^2 \cdot \left( \frac{r_s^2}{(r_s^2 + r_{ij}^2)} \right). \quad (4.12)$$

## 4.2 Dilatation

After [Egli et al., 2007] the local strain field can be used to characterize the trend metric changing the correlation between two points. High deformation rates between two points indicate weak correlation. To represent this behavior, a process to enlarge the distance between points (deforming the metric) with high relative deformation is introduced and further referenced as dilatation. By changing the trend metric, which is used to calculate the distance between two points, the correlation can be adjusted. Due to these iterations, the strain rates define the tectonic setup.

The trend covariance matrix adjustment is done by deforming the grid based on the field characteristics. This process is done using a dilatation, a continuous and derivable vector function  $\mathbf{D}(\mathbf{r}, \mathbf{r}_0, \mathbf{u}_1, \mathbf{u}_2, e_1, e_2, e_3, \gamma)$  which defines a coordinate transformation:

$$\mathbf{r}' = \mathbf{r} + \mathbf{D}(\mathbf{r}, \mathbf{r}_0, \mathbf{u}_1, \mathbf{u}_2, e_1, e_2, e_3, \gamma) \quad (4.13)$$

with

$\mathbf{r}$	point which is to be displaced
$\mathbf{r}'$	transformed coordinate
$\mathbf{r}_0$	centre of dilatation
$\mathbf{u}_1, \mathbf{u}_2, \mathbf{u}_3$	orientation given by unit vector
$e_1, e_2, e_3 > 0$	scaling coefficients
$\gamma$	dilatation length

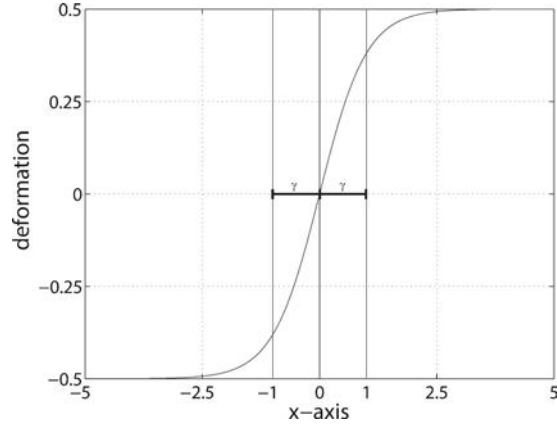


**Figure 4.1:** Deformation along the dilatation axis  $\mathbf{u}_1 = \text{x-axis}$  with  $\gamma = 1$  and  $e_1 = 1$ . The up-axis shows the dilatation value with respect to the distance from the centre (x-axis).

fulfilling the following two properties (scalar product between two points  $\mathbf{r}_a$  and  $\mathbf{r}_b$  is written as:  $\langle \mathbf{r}_a, \mathbf{r}_b \rangle$ )

$$\lim_{|\mathbf{r}-\mathbf{r}_0|/\gamma \rightarrow 0} \mathbf{r}' - \mathbf{r}_0 = \sum_{i=1}^3 e_i \langle \mathbf{r} - \mathbf{r}_0, \mathbf{u}_i \rangle \quad (4.14)$$

$$\lim_{|\mathbf{r}-\mathbf{r}_0|/\gamma \rightarrow \infty} \mathbf{r}' - \mathbf{r}_0 = 0. \quad (4.15)$$

According to Equation (4.14) a small region around the source is stretched along the basis vectors  $\mathbf{u}_i$  around the dilatation centre  $\mathbf{r}_0$ . The transformation does not affect points whose distance  $r$  to the centre is  $\gg \gamma$ . A simple function which fulfills these properties is

$$\mathbf{D}(\mathbf{r}, \mathbf{r}_0, \mathbf{u}_1, \mathbf{u}_2, e_1, e_2, e_3, \gamma) = \Delta(|\mathbf{r} - \mathbf{r}_0|, \gamma) \sum_{l=1}^3 e_l \langle (\mathbf{r} - \mathbf{r}_0), \mathbf{u}_l \rangle \mathbf{u}_l \quad (4.16)$$

$$\Delta(r, \gamma) = \frac{\gamma}{r} \tanh\left(\frac{r}{\gamma}\right) \quad (4.17)$$

The behavior of the chosen function is shown in Figure 4.1 displaying the calculated dilatation value based on the distance to the source. The effect of a single 2-D dilatation source is shown in Figure 4.2. The dilatation source has its centre point  $\mathbf{r}_0$  in  $(0, 0)$  and the deformation axes  $\mathbf{u}_1, \mathbf{u}_2$  parallel to the x- and y-axis, respectively. The left image has equal scaling coefficients ( $e_1 = e_2 = 0.5$ ). In the right image only one axis has a non-zero scaling coefficient ( $e_1 = 0.5$  and  $e_2 = 0$ ). A grid of  $N$  points may be introduced as origin points for the dilatation sources. Therefore, all  $N$  dilatation sources have to be applied to receive the adapted trend metric:

$$\mathbf{r}'_i = \mathbf{r}_i + \sum_{l=1}^N \mathbf{D}(\mathbf{r}_i, \mathbf{r}_l, \mathbf{u}_{l1}, \mathbf{u}_{l2}, e_{l1}, e_{l2}, e_{l3}, \gamma) \quad (4.18)$$

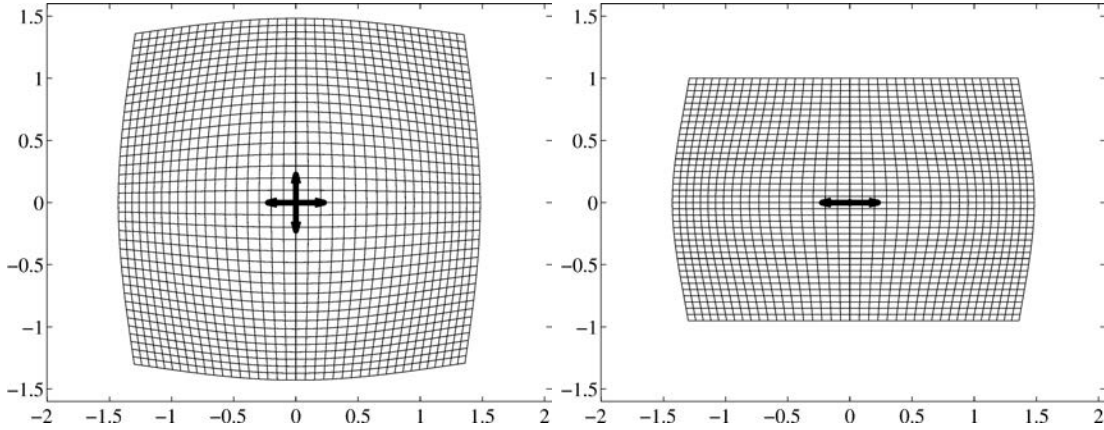


**Figure 4.2:** Example of a coordinate transformation using one 2-D dilatation source. For both plots the dilatation parameters are equal except for the scaling coefficient ( $\mathbf{r}_0 = (0, 0)$ ,  $\gamma = 0.5$ ,  $\mathbf{u}_1 = (1, 0)$ ,  $\mathbf{u}_2 = (0, 1)$ ). Left plot:  $e_1 = 0.5$ ,  $e_2 = 0.5$ . Right plot:  $e_1 = 0.5$ ,  $e_2 = 0$

#### 4.2.1 Determination of the dilatation parameters

The directional derivative, in direction  $\mathbf{n}$ , of the coordinate transformation is

$$\frac{\partial}{\partial \mathbf{n}} \mathbf{D}(\mathbf{r}, \mathbf{r}_0, \mathbf{u}_1, \mathbf{u}_2, e_1, e_2, e_3, \gamma) = \sum_{l=1}^3 e_l [\langle \mathbf{G}(\mathbf{r} - \mathbf{r}_0, \mathbf{n}, \gamma), \mathbf{u}_l \rangle] \mathbf{u}_l \quad (4.19)$$

$$\mathbf{G}(\mathbf{r}, \mathbf{n}, \gamma) = \langle \mathbf{r}, \mathbf{n} \rangle \frac{\mathbf{r}}{r^2} \operatorname{sech}^2\left(\frac{r}{\gamma}\right) + \frac{\gamma}{r} \left[ \mathbf{n} - \langle \mathbf{r}, \mathbf{n} \rangle \frac{\mathbf{r}}{r^2} \right] \tanh\left(\frac{r}{\gamma}\right) \quad (4.20)$$

According to Equation (4.19) and (4.20) the derivative of (4.18) for a point  $\mathbf{r}_j, 1 \leq j \leq N$  along the three perpendicular directions  $\mathbf{d}_{j1}, \mathbf{d}_{j2}, \mathbf{d}_{j3}$  is:

$$\sum_{k=1}^N \sum_{l=1}^3 [e_{kl} \langle \mathbf{G}_{kj1} \mathbf{u}_{kl} \rangle \mathbf{u}_{kl}] = d_{j1} \mathbf{d}_{j1} \quad (4.21)$$

$$\sum_{k=1}^N \sum_{l=1}^3 [e_{kl} \langle \mathbf{G}_{kj2} \mathbf{u}_{kl} \rangle \mathbf{u}_{kl}] = d_{j2} \mathbf{d}_{j2} \quad (4.22)$$

$$\sum_{k=1}^N \sum_{l=1}^3 [e_{kl} \langle \mathbf{G}_{kj3} \mathbf{u}_{kl} \rangle \mathbf{u}_{kl}] = d_{j3} \mathbf{d}_{j3} \quad (4.23)$$

with

$$\mathbf{G}_{kjl} = \mathbf{G}(\mathbf{r}_j - \mathbf{r}_k, \mathbf{d}_{jl}, \gamma) \quad (4.24)$$

The equations can be simplified replacing  $\mathbf{u}_{kl}$  with  $\mathbf{d}_{kl}$  assuming that the unit vectors  $\mathbf{u}_{kl} \approx \mathbf{d}_{kl}$ . A scalar product of all Equations (4.21–4.23) with  $\mathbf{d}_{km}$ ,  $m = 1, 2, 3$ , with  $\delta_{ml}$  as the Kronecker delta, leads to:

$$\sum_{k=1}^N \sum_{l=1}^3 [e_{kl} \langle \mathbf{G}_{kj1} \mathbf{d}_{kl} \rangle \langle \mathbf{d}_{kl}, \mathbf{d}_{jm} \rangle] = d_{j1} \delta_{ml} \quad (4.25)$$

Assuming  $\langle \mathbf{d}_{kl} \mathbf{d}_{jm} \rangle \approx 0$  for  $l \neq m$  and points nearby  $|\mathbf{r}_j - \mathbf{r}_k| \leq \gamma$  and  $\mathbf{G}_{kjl} \mathbf{d}_{km} \approx 0$  for  $l \neq m$  for two near points, and  $|\mathbf{r}_j - \mathbf{r}_k| \gg \gamma$ ,  $\mathbf{G}_{kjl} \approx 0$  for two far points allows to eliminate all terms in which  $l \neq m$ . This leads to

$$\sum_{k=1}^N \sum_{l=1}^3 [e_{kl} \langle \mathbf{G}_{kj1} \mathbf{d}_{kl} \rangle \langle \mathbf{d}_{kl}, \mathbf{d}_{j1} \rangle] = d_{j1} \quad (4.26)$$

$$\sum_{k=1}^N \sum_{l=1}^3 [e_{kl} \langle \mathbf{G}_{kj2} \mathbf{d}_{kl} \rangle \langle \mathbf{d}_{kl}, \mathbf{d}_{j2} \rangle] = d_{j2} \quad (4.27)$$

$$\sum_{k=1}^N \sum_{l=1}^3 [e_{kl} \langle \mathbf{G}_{kj3} \mathbf{d}_{kl} \rangle \langle \mathbf{d}_{kl}, \mathbf{d}_{j3} \rangle] = d_{j3} \quad (4.28)$$

Now this is a set of  $3N$  linear equations for  $3N$  unknown variables  $e_{kl}$  which can be solved. This leads to the following parameters with  $\mathbf{e}_{kl}$ , with  $l = 1, 2, 3$ , as the three eigenvectors of the strain tensor  $\epsilon_k$  for point  $k$  and  $e_{kl}$  the corresponding eigenvalues:

- $\mathbf{e}_{kl} = \mathbf{d}_{kl}$  is derived from the gradient field
- $d_{kl}$  is derived from the gradient field
- $e_{kl}$  obtained by solving Equations (4.26)–(4.28)

## 4.2.2 Dilatation definition

As described in Section 4.2.1, if the deformation scale and direction is known at the dilatation sources, the scaling rates  $e_{kl}$  can be determined. The geodetic strain rate field characteristics has to be transformed into the trend metric. Using a least-squares method allows to extract the strain rates for all dilatation sources from the measured velocities. The connection between the strain rates and the dilatation process is the main strain axis. The eigenvectors and eigenvalues of the strain rate tensor at point  $\mathbf{r}_j$  are  $\epsilon'_{jl}$  and  $\lambda_{jl}$  with  $l = 1, 2, 3$ . They describe the main deformation directions and rates. They are used as the deformation inputs  $\mathbf{d}_{jl}$  and  $d_{jl}$ . An additional scaling parameter  $\lambda_{\max}$  is applied to define the maximum allowed ratio between a distance before and after the dilatation process:

$$\mathbf{d}_{jl} = \epsilon'_{jl} \quad (4.29)$$

$$d_{jl} = \mu \lambda_{\max}^{-1} \lambda_{jl} \quad (4.30)$$

where  $\lambda_{\max}$  is the absolute maximum eigenvalue and  $\mu$  defines the maximum allowed deformation rate (between a distance before and after the deformation process).

## 4.3 Parameter estimation

### 4.3.1 Velocity and strain estimation

The ALS method is used to determine an inhomogeneous trend metric describing the tectonic setting characterized by the measurements himself. The velocities can be extracted

similarly to the normal least-squares collocation technique (see Equations (4.5) and (4.6)). The deformed trend metric does not have a direct impact on the velocity estimation. For the strain extraction, however, the deformation process has a major influence. It deforms the grid and, therefore, also the direction and distance between two points.

The trend velocity with  $\mathbf{l}$  as the measured velocities is given by:

$$\hat{\mathbf{t}} = \mathbf{C}_{\hat{t}t} \cdot (\mathbf{C}_{tt} + \mathbf{C}_{ss} + \mathbf{C}_{nn})^{-1} \cdot \mathbf{l} \quad (4.31)$$

And the strain rate is defined by:

$$\frac{\partial \hat{\mathbf{t}}}{\partial x} = \frac{\partial x'}{\partial x} \frac{\partial \hat{\mathbf{t}}}{\partial x'} + \frac{\partial y'}{\partial x} \frac{\partial \hat{\mathbf{t}}}{\partial y'} + \frac{\partial z'}{\partial x} \frac{\partial \hat{\mathbf{t}}}{\partial z'} \quad (4.32)$$

$$\frac{\partial \hat{\mathbf{t}}}{\partial y} = \frac{\partial x'}{\partial y} \frac{\partial \hat{\mathbf{t}}}{\partial x'} + \frac{\partial y'}{\partial y} \frac{\partial \hat{\mathbf{t}}}{\partial y'} + \frac{\partial z'}{\partial y} \frac{\partial \hat{\mathbf{t}}}{\partial z'} \quad (4.33)$$

$$\frac{\partial \hat{\mathbf{t}}}{\partial z} = \frac{\partial x'}{\partial z} \frac{\partial \hat{\mathbf{t}}}{\partial x'} + \frac{\partial y'}{\partial z} \frac{\partial \hat{\mathbf{t}}}{\partial y'} + \frac{\partial z'}{\partial z} \frac{\partial \hat{\mathbf{t}}}{\partial z'} \quad (4.34)$$

with

$$\frac{\partial \hat{\mathbf{t}}}{\partial x'} = \frac{\partial \mathbf{C}_{\hat{t}t}}{\partial x'} \cdot (\mathbf{C}_{tt} + \mathbf{C}_{ss} + \mathbf{C}_{nn})^{-1} \cdot \mathbf{l} \quad (4.35)$$

and analogous formulas for  $\frac{\partial \hat{\mathbf{t}}}{\partial y'}$  and  $\frac{\partial \hat{\mathbf{t}}}{\partial z'}$ .

$$(4.36)$$

### 4.3.2 Trend and strain error estimation

The precision of the trend and signal velocity parts can be extracted equally to a normal least-square collocation [Egli *et al.*, 2007; Moritz, 1970]. Equation (4.34) shows that the strain part also includes the change of the metric. In order to derive the strain values in the original metric, the changes from the dilatation process have to be taken into account. This section will describe the mathematics to obtain the accuracies based on [Egli *et al.*, 2007; Moritz, 1973]. Following these two papers with the error matrix  $\mathbf{E}_{\hat{t}t} = E(\epsilon_{\hat{t}t}^T)$ ,  $\epsilon_{\hat{t}} = \hat{\mathbf{t}} - \bar{\mathbf{t}}$ , and  $\bar{\mathbf{t}}$  as the error free value leads to

$$\begin{aligned} \epsilon_{\hat{t}} \epsilon_{\hat{t}}^T &= (\mathbf{H}\mathbf{l} - \bar{\mathbf{t}})(\mathbf{H}\mathbf{l} - \bar{\mathbf{t}})^T \\ &= \mathbf{H}\mathbf{U}^T \mathbf{H}^T - \bar{\mathbf{U}}^T \mathbf{H}^T - \mathbf{H}(\bar{\mathbf{U}}^T)^T + \bar{\mathbf{t}}\bar{\mathbf{t}}^T \end{aligned} \quad (4.37)$$

with

$$\mathbf{H} = \mathbf{C}_{\hat{t}t} (\mathbf{C}_{tt} + \mathbf{C}_{ss} + \mathbf{C}_{nn})^{-1} \quad (4.38)$$

assuming  $\mathbf{t}$ ,  $\mathbf{s}$  and  $\mathbf{n}$  to be independent leads to

$$E(\mathbf{U}^T) = \mathbf{C}_{tt} + \mathbf{C}_{ss} + \mathbf{C}_{nn} \quad (4.39)$$

$$E(\overline{\mathbf{t}\mathbf{t}^T}) \approx \mathbf{C}_{\hat{t}\hat{t}} \quad (4.40)$$

$$E(\overline{\mathbf{t}\mathbf{l}^T}) \approx \mathbf{C}_{\hat{t}\hat{l}} \quad (4.41)$$

and therefore

$$\mathbf{E}_{\hat{t}\hat{t}} = \mathbf{C}_{\hat{t}\hat{t}} - \mathbf{C}_{\hat{t}\hat{l}}(\mathbf{C}_{tt} + \mathbf{C}_{ss} + \mathbf{C}_{nn})^{-1}\mathbf{C}_{\hat{t}\hat{l}}^T. \quad (4.42)$$

The strain rates  $\mathbf{g}$  are the gradients of the velocity field, i. e.  $\mathbf{g} = \nabla\hat{\mathbf{t}}$  and  $\mathbf{g}_x$  the x-component of the strain rate. Rewriting Equation (4.34) using following notation

$$\mathbf{X}'_x = \frac{\partial\mathbf{x}'}{\partial x} \quad \mathbf{Y}'_x = \frac{\partial\mathbf{y}'}{\partial x} \quad \mathbf{Z}'_x = \frac{\partial\mathbf{z}'}{\partial x} \quad (4.43)$$

leads to

$$\mathbf{g}_x = [(\mathbf{X}'_x\partial_{x'} + \mathbf{Y}'_x\partial_{y'} + \mathbf{Z}'_x\partial_{z'})\mathbf{C}_{\hat{t}\hat{t}}](\mathbf{C}_{tt} + \mathbf{C}_{ss} + \mathbf{C}_{nn})^{-1}\mathbf{l} = \mathbf{G}\mathbf{l}. \quad (4.44)$$

From this equation we use the same error definition as the one used to extract the precision of the velocities (4.37).

$$\begin{aligned} \boldsymbol{\epsilon}_{\hat{g}_x}\boldsymbol{\epsilon}_{\hat{g}_x}^T &= (\mathbf{G}\mathbf{l} - \bar{\mathbf{g}}_x)(\mathbf{G}\mathbf{l} - \bar{\mathbf{g}}_x)^T \\ &= \mathbf{G}\mathbf{l}\mathbf{l}^T\mathbf{G}^T - \bar{\mathbf{g}}_x\mathbf{l}^T\mathbf{G}^T - \mathbf{G}(\bar{\mathbf{g}}_x\mathbf{l}^T)^T + \bar{\mathbf{g}}_x\bar{\mathbf{g}}_x^T \end{aligned} \quad (4.45)$$

using the assumptions following [Peter, 2000] and [Egli et al., 2007]

$$\begin{aligned} E(\bar{\mathbf{g}}_x\mathbf{l}^T) &= (\mathbf{X}'_x\partial_{x'} + \mathbf{Y}'_x\partial_{y'} + \mathbf{Z}'_x\partial_{z'})\mathbf{C}_{\hat{t}\hat{t}} \\ E(\bar{\mathbf{g}}_x\bar{\mathbf{g}}_x^T) &= \frac{\partial}{\partial x}(\mathbf{X}'_x\partial_{x'} + \mathbf{Y}'_x\partial_{y'} + \mathbf{Z}'_x\partial_{z'})\mathbf{C}_{\hat{g}_x\hat{g}_x} \end{aligned} \quad (4.46)$$

with

$$\begin{aligned} \frac{\partial}{\partial x}\partial_{x'} &= (\mathbf{X}'_x\partial_{x'} + \mathbf{Y}'_x\partial_{y'} + \mathbf{Z}'_x\partial_{z'})\frac{\partial}{\partial x'} \\ E(\bar{\mathbf{g}}_x\bar{\mathbf{g}}_x^T) &= (\mathbf{X}'_{xx}\partial_{x'} + \mathbf{Y}'_{xx}\partial_{y'} + \mathbf{Z}'_{xx}\partial_{z'} + \mathbf{X}'_x{}^2\partial_{x'x'} + \mathbf{Y}'_x{}^2\partial_{y'y'} + \mathbf{Z}'_{xx}\partial_{z'z'} + \\ &\quad 3\mathbf{X}'_x\mathbf{Y}'_x\partial_{x'y'} + 3\mathbf{X}'_x\mathbf{Z}'_x\partial_{x'z'} + 3\mathbf{Y}'_x\mathbf{Z}'_x\partial_{y'z'})\mathbf{C}_{\hat{t}\hat{t}} \end{aligned} \quad (4.47)$$

leads to

$$\mathbf{E}_{\hat{g}_x\hat{g}_x} = E(\bar{\mathbf{g}}_x\bar{\mathbf{g}}_x^T) - E(\bar{\mathbf{g}}_x\mathbf{l}^T)\mathbf{C}_{zz}^{-1}E(\bar{\mathbf{g}}_x\mathbf{l}^T)^T \quad (4.48)$$

with

$$\mathbf{C}_z z = (\mathbf{C}_{tt} + \mathbf{C}_{ss} + \mathbf{C}_{nn}). \quad (4.49)$$

Therefore, the strain precision is

$$\begin{aligned}
 E_{\hat{g}_x \hat{g}_x} = & (\mathbf{X}'_{xx} \partial_{x'} + \mathbf{Y}'_{xx} \partial_{y'} + \mathbf{Z}'_{xx} \partial_{z'} + \mathbf{X}'_x{}^2 \partial_{x'x'} + \mathbf{Y}'_x{}^2 \partial_{y'y'} + \mathbf{Z}'_x{}^2 \partial_{z'z'} + \\
 & 3\mathbf{X}'_x \mathbf{Y}'_x \partial_{x'y'} + 3\mathbf{X}'_x \mathbf{Z}'_x \partial_{x'z'} + 3\mathbf{Y}'_x \mathbf{Z}'_x \partial_{y'z'}) \mathbf{C}_{\hat{t}t} - \\
 & ((\mathbf{X}'_x \partial_{x'} + \mathbf{Y}'_x \partial_{y'} + \mathbf{Z}'_x \partial_{z'}) \mathbf{C}_{\hat{t}t}) \mathbf{C}_{zz}^{-1} ((\mathbf{X}'_x \partial_{x'} + \mathbf{Y}'_x \partial_{y'} + \mathbf{Z}'_x \partial_{z'}) \mathbf{C}_{\hat{t}t})^T
 \end{aligned} \tag{4.50}$$

and in the same way for y and z components.

## 4.4 Thin plate model

Surface deformation is observable by levelling and GNSS measurements which are mostly available at surface points only. Therefore, the direct determination of strain rates along the vertical axis is impossible. To extract a strain tensor with non-zero uplift strain rates a plate model describing the downward continuation is needed. A simple model to represent the Earth's crust is the planar thin plate model [Bauchau and Craig, 2009; Geiger et al., 1986]. Using standard values for the rheology combined with the thin plate model leads to the uplift strain rate.

The deformation tensor  $\mathbf{U}$  defines the deformation of an infinitesimally small area at a given point. The deformation tensor is defined by the (spatial) gradient of  $\mathbf{u}$ .

The main problem is the lack of measurements along the vertical axis (below the surface), whereas the horizontal movement and the uplift rates on the Earth surface are known. The downward continuation of the displacement is unknown as all geodetically are performed on the surface. Therefore, a full 3-D tensor can only be obtained by introducing additional models describing the subsurface behavior. The simplest model is to assume that the deformation on the surface remains constant along the vertical. This leads to a vertical deformation component of zero. The volume change along the vertical remains zero as well. The direction of one eigenvector of the strain tensor is then always parallel to the z-axis. The 2-D model is used to compare results with 2-D data and the 3-D model only if the full 3-D tensor is needed.

The thin plate model is another means to reconstruct a full 3-D tensor. As initial condition, a Kirchhoff-Love plate is used where it is assumed that plate bending is due to uplift only. This leads to the following deformation tensor with  $\mathbf{u} = (u_x, u_y, u_z)^T$ :

$$\mathbf{U} = \begin{pmatrix} -z \frac{\partial^2 u_z}{\partial x^2} & -z \frac{\partial^2 u_z}{\partial xy} & 0 \\ -z \frac{\partial^2 u_z}{\partial xy} & -z \frac{\partial^2 u_z}{\partial y^2} & 0 \\ \frac{\partial u_z}{\partial x} & \frac{\partial u_z}{\partial y} & 0 \end{pmatrix} \tag{4.51}$$

with  $z$  as the vertical distance to the midlayer of the thin plate; positive values of  $z$  are above and negative values are below the plate midlayer.

With the introduction of the thin plate model it is possible to determine the strain rates below the surface for the horizontal components. The uplift component is still unknown.

Hooke's law is used to overcome this problem introducing the Poisson's ratio  $\nu = 0.25$  [Stein and Wyssession, 2003]:

$$\nu = -\frac{d\epsilon_{trans}}{d\epsilon_{axial}} \quad (4.52)$$

with

$$\begin{aligned} \nu & \quad \text{Poisson's ratio} \\ d\epsilon_{axial} & \quad \text{applied deformation} \\ d\epsilon_{trans} & \quad \text{resulting deformation in the transverse axis} \end{aligned}$$

We assume that the displacement  $\mathbf{u}$  is a result of a pulling or pushing force in the axial direction  $\mathbf{m} = (m_x, m_y, m_z)^T$  and the transverse deformation introduced by the acting force on the two other axes.

$$\frac{\partial u_x}{\partial x} = \frac{\partial m_x}{\partial x} - \nu \left( \frac{\partial m_y}{\partial y} + \frac{\partial m_z}{\partial z} \right) \quad (4.53)$$

$$\frac{\partial u_y}{\partial y} = \frac{\partial m_y}{\partial y} - \nu \left( \frac{\partial m_x}{\partial x} + \frac{\partial m_z}{\partial z} \right) \quad (4.54)$$

$$\frac{\partial u_z}{\partial z} = \frac{\partial m_z}{\partial z} - \nu \left( \frac{\partial m_x}{\partial x} + \frac{\partial m_y}{\partial y} \right). \quad (4.55)$$

Under the assumption that the formation in the  $z$ -component is only driven by the transverse deformation on the horizontal axis, we have

$$\frac{\partial m_z}{\partial z} = 0. \quad (4.56)$$

Combined with Equations (4.53) and (4.54) with the condition given by Equation (4.56) this leads to

$$\frac{\partial m_x}{\partial x} = \frac{\frac{\partial u_x}{\partial x} + \nu \frac{\partial u_y}{\partial y}}{1 - \nu^2} \quad (4.57)$$

$$\frac{\partial m_y}{\partial y} = \frac{\frac{\partial u_y}{\partial y} + \nu \frac{\partial u_x}{\partial x}}{1 - \nu^2}. \quad (4.58)$$

Introducing the upper two equations into (4.55), the vertical deformation is

$$\frac{\partial u_z}{\partial z} = -\nu \left( \frac{\frac{\partial u_x}{\partial x} + \frac{\partial u_y}{\partial y}}{1 - \nu} \right) \quad (4.59)$$

and the 3-D deformation tensor becomes

$$\mathbf{U} = \begin{pmatrix} -z \frac{\partial^2 u_z}{\partial x^2} & -z \frac{\partial^2 u_z}{\partial x y} & 0 \\ -z \frac{\partial^2 u_z}{\partial x y} & -z \frac{\partial^2 u_z}{\partial y^2} & 0 \\ \frac{\partial u_z}{\partial x} & \frac{\partial u_z}{\partial y} & \frac{z\nu}{(1-\nu)} \left( \frac{\partial^2 u_z}{\partial x^2} + \frac{\partial^2 u_z}{\partial y^2} \right) \end{pmatrix} \quad (4.60)$$

in order to fulfill the volume change criteria. Therefore, the volume change of the deformation tensor  $\mathbf{U}$  is coherent with the rheology parameters. This formula represents the 3-D strain tensor derived from a thin plate model. Adding a time derivative to the equation leads to the strain rate tensor with  $\mathbf{v} = \dot{\mathbf{u}}$ .

$$\dot{\mathbf{U}} = \begin{pmatrix} -z \frac{\partial^2 v_z}{\partial x^2} & -z \frac{\partial^2 v_z}{\partial xy} & 0 \\ -z \frac{\partial^2 v_z}{\partial xy} & -z \frac{\partial^2 v_z}{\partial y^2} & 0 \\ \frac{\partial v_z}{\partial x} & \frac{\partial v_z}{\partial y} & \frac{z\nu}{(1-\nu)} \left( \frac{\partial^2 v_z}{\partial x^2} + \frac{\partial^2 v_z}{\partial y^2} \right) \end{pmatrix} \quad (4.61)$$

Equation (4.60) describes the deformation following a thin plate bending model. The collocation technique delivers the horizontal derivatives of the displacement  $\mathbf{u}$ . The displacement  $\mathbf{u}$  and its derivatives  $\mathbf{U}_m$  describe the behaviour on the surface:

$$\mathbf{U}_m = \begin{pmatrix} \frac{\partial u_x}{\partial x} & \frac{\partial u_y}{\partial y} & 0 \\ \frac{\partial u_x}{\partial x} & \frac{\partial u_y}{\partial y} & 0 \\ \frac{\partial u_z}{\partial x} & \frac{\partial u_z}{\partial y} & 0 \end{pmatrix} \quad (4.62)$$

where the derivatives in z-direction are not directly accessible. The combination of Equations (4.63) and (4.60) where the derivatives at the surface are determined by measurements, leads to Equation (4.63). The vertical derivatives are described by the thin plate model leading to  $\mathbf{U}_s$  with  $h$  as the plate thickness and  $z_s = 1/2h$ . Introducing the displacement  $\mathbf{o} = (o_x, o_y, o_z)^T$ , measured at the surface the deformation tensor  $\mathbf{U}$  becomes to

$$\mathbf{U}_s = \begin{pmatrix} \frac{\partial o_x}{\partial x} & \frac{\partial o_y}{\partial x} & 0 \\ \frac{\partial o_x}{\partial y} & \frac{\partial o_y}{\partial y} & 0 \\ \frac{\partial o_z}{\partial x} & \frac{\partial o_z}{\partial y} & \frac{z_s \nu}{(1-\nu)} \left( \frac{\partial^2 o_z}{\partial x^2} + \frac{\partial^2 o_z}{\partial y^2} \right) \end{pmatrix} \quad (4.63)$$

and the deformation tensor  $\mathbf{U}_z$  for a point along the vertical axis reads

$$\mathbf{U}_z = \begin{pmatrix} \frac{\partial o_x}{\partial x} + (z_s - z) \frac{\partial^2 o_z}{\partial x^2} & \frac{\partial o_y}{\partial x} + (z_s - z) \frac{\partial^2 o_z}{\partial xy} & 0 \\ \frac{\partial o_x}{\partial y} + (z_s - z) \frac{\partial^2 o_z}{\partial xy} & \frac{\partial o_y}{\partial y} + (z_s - z) \frac{\partial^2 o_z}{\partial y^2} & 0 \\ \frac{\partial o_z}{\partial x} & \frac{\partial o_z}{\partial y} & \frac{z\nu}{(1-\nu)} \left( \frac{\partial^2 o_z}{\partial x^2} + \frac{\partial^2 o_z}{\partial y^2} \right) \end{pmatrix}. \quad (4.64)$$

With the midlayer deformation, described by the part independent of  $z$ , and the bending part, the 3-D tensor can be computed for the whole plate thickness. For the application of this method, the plate thickness  $h$  is needed additionally. The plate is assumed to extend from the surface down to the Moho discontinuity. Therefore, the Moho depth corresponds to the thickness.

## 4.5 Strain energy density

The strain energy is used to estimate the accumulated deformation energy in the crust caused by the plate motion. It can be calculated for both models, the 2-D and the thin plate

model. However, the 2-D model has no vertical strain rates and assumes the horizontal components to remain constant across the plate thickness. The horizontal strain energy density per square metre is expressed as :

$$D_E = \int_0^h \frac{1}{2} \text{trace}(\boldsymbol{\sigma}^T \boldsymbol{\epsilon}) dz = \frac{1}{2} \text{trace}(\boldsymbol{\sigma}^T \boldsymbol{\epsilon}) h \quad (4.65)$$

where  $h$  is the plate thickness and  $\boldsymbol{\sigma}$  the stress tensor. The stress tensor can be expressed by the strain tensor  $\boldsymbol{\epsilon}$  using Lamé's parameters ( $\lambda$  and the shear modulus  $\mu$ ) and identity matrix  $\mathbf{I}$ :

$$\boldsymbol{\sigma} = 2\mu\boldsymbol{\epsilon} + \lambda\theta\mathbf{I} \quad (4.66)$$

$$\theta = \sum_{i=1}^3 \epsilon_{ii} = \text{trace}(\boldsymbol{\epsilon}) \quad (4.67)$$

and inserted into Equation (4.65) with  $\text{trace}(\theta\boldsymbol{\epsilon}) = \theta^2$  gives

$$D_E = \frac{1}{2} (\text{trace}(2\mu\boldsymbol{\epsilon}^T \boldsymbol{\epsilon}) + \lambda\theta^2) h \quad (4.68)$$

For the thin plate model the strain energy density formula needs to be adjusted as the tensor does not remain constant along the vertical. The thin plate strain tensor can be decomposed into a z-dependent part (bent) and a part which remains constant along the z-axis (linear). Inserting Equation (4.64) into

$$\boldsymbol{\epsilon} = \frac{1}{2} (\mathbf{U} + \mathbf{U}^T) \quad (4.69)$$

we obtain

$$\boldsymbol{\epsilon} = \mathbf{K} + z \cdot \mathbf{Z} \quad (4.70)$$

with

$$\mathbf{K} = \begin{pmatrix} \frac{\partial v_x}{\partial x} & \frac{1}{2} \left( \frac{\partial v_y}{\partial x} + \frac{\partial v_x}{\partial y} \right) & \frac{1}{2} \frac{\partial v_z}{\partial x} \\ \frac{1}{2} \left( \frac{\partial v_y}{\partial x} + \frac{\partial v_x}{\partial y} \right) & \frac{\partial v_y}{\partial y} & \frac{1}{2} \frac{\partial v_z}{\partial x} \\ \frac{1}{2} \frac{\partial v_z}{\partial x} & \frac{1}{2} \frac{\partial v_z}{\partial y} & 0 \end{pmatrix} \quad (4.71)$$

$$\mathbf{Z} = \begin{pmatrix} -\frac{\partial^2 v_z}{\partial x^2} & -\frac{\partial^2 v_z}{\partial xy} & 0 \\ -\frac{\partial^2 v_z}{\partial xy} & -\frac{\partial^2 v_z}{\partial y^2} & 0 \\ 0 & 0 & \frac{\nu}{(1-\nu)} \left( \frac{\partial^2 v_z}{\partial x^2} + \frac{\partial^2 v_y}{\partial y^2} \right) \end{pmatrix} \quad (4.72)$$

The stress tensor (Equation (4.66)) yields:

$$\boldsymbol{\sigma} = \underbrace{2\mu\mathbf{K} + \lambda\text{Tr}(\mathbf{K}) \cdot \mathbf{I}}_S + z \underbrace{(2\mu\mathbf{Z} + \lambda\text{trace}(\mathbf{Z})\mathbf{I})}_Q \quad (4.73)$$

$$\boldsymbol{\sigma} = \mathbf{S} + z\mathbf{Q} \quad (4.74)$$

Inserting Equation (4.73) into Equation (4.65)

$$D_E = \frac{1}{2} \int_0^h \text{trace}(\mathbf{S}^T \mathbf{K} + z(\mathbf{Q}^T \mathbf{K} + \mathbf{S}^T \mathbf{Z}) + \mathbf{Q}^T \mathbf{Z} z^2) dz \quad (4.75)$$

After integration along the plate thickness  $z \in [-\frac{h}{2}, \frac{h}{2}]$  we finally get

$$\begin{aligned} D_E &= \frac{1}{2} \text{trace}(\mathbf{S}^T \mathbf{K}) \cdot h + \frac{1}{2} \text{trace}(\mathbf{Q}^T \mathbf{K} + \mathbf{S}^T \mathbf{Z}) \cdot 0 \cdot h^2 + \text{trace}(\mathbf{Q}^T \mathbf{Z}) \cdot \frac{h^3}{2 \cdot 12} \\ &= \underbrace{\left( \mu \text{trace}(\mathbf{K}^T \mathbf{K}) + \frac{1}{2} \lambda \text{trace}^2(\mathbf{K}) \right)}_{\text{non-bent}} \cdot h + \underbrace{\left( \mu \text{trace}(\mathbf{Z}^T \mathbf{Z}) + \frac{1}{2} \text{trace}^2(\mathbf{Z}) \right)}_{\text{bent}} \cdot \frac{h^3}{12} \end{aligned} \quad (4.76)$$

The two parts of the energy distribution can be identified as the non-bending (linearly dependent on  $h$ ) and the bending part. The latter part increases non-linearly with increasing depth whereas the non-bending part remains linear. The resulting horizontal strain energy density ( $[\text{N}/\text{m}^2]$ ) can be used to determine regions with high values indicating a higher seismic hazard.

## 4.6 Fault planes from strain

Under the assumption of isotropic material the strain and stress tensors can be connected using the crust rheology. Stress and strain are related by Hooke's law, if the crust is linearly elastic [Stein and Wysession, 2003]. Using Einstein's summation convention the relationship between the stress  $\sigma_{ij}$  and strain  $\epsilon_{ij}$  them can be described as follow

$$\sigma_{ij} = c_{ijkl} \epsilon_{kl} \quad (4.77)$$

The constants  $c_{ijkl}$  are the elastic moduli containing the material properties. Starting from this equation strain can be expressed by stress and the material's rheology parameters  $\lambda$ , Lamé's first parameter, and  $\mu$ , Lamé's second parameter, the shear modulus. The Equations (4.66) and (4.67) can be rewritten into the main components (eigenvectors and -values)  $\sigma'_i$  and  $\sigma_i$  for the stress tensor  $\boldsymbol{\sigma}$  and  $\epsilon'$  and  $\epsilon_i$  for the strain tensor  $\boldsymbol{\epsilon}$

$$\sigma'_i = \lambda \theta + 2\mu \epsilon'_i \quad (4.78)$$

The direction of maximum compressive principal stress (T) and minimum compressive principal stress (P) are given by the vectors  $\mathbf{t}$  (tension) and  $\mathbf{p}$  (pressure). The principal stress and strain axes are parallel as can be derived from Equation (4.78). Therefore,  $\mathbf{p}$  and  $\mathbf{t}$  are the strain tensor's eigenvectors with the maximal and minimal eigenvalue. Ordering the eigenvalues that  $\epsilon'_1 > \epsilon'_2 > \epsilon'_3$ , the tension axis is parallel to  $\mathbf{e}'_1$  ( $\sigma'_1$  or  $\epsilon'_1$ ) and the pressure axis parallel to  $\mathbf{e}'_3$  ( $\sigma'_3$  or  $\epsilon'_3$ ).

The fault planes can be extracted from the stress tensor assuming a homogeneous material. The so-called beachball representation is an adequate way to graphical represent the fault

planes. Converting the stress tensor into dip  $\rho$ , strike  $\phi$  and rake  $\gamma$  is described in various standard textbooks such as [Stein and Wysession, 2003]. A brief summary of the fault plane estimation is given here. The fault plane with its normal  $\mathbf{n}$  and slip direction  $\mathbf{d}$  can be expressed as

$$\mathbf{t} = \mathbf{n} + \mathbf{d} \quad (4.79)$$

$$\mathbf{p} = \mathbf{n} - \mathbf{d} \quad (4.80)$$

Knowing  $\mathbf{t} = \mathbf{e}_1$  and  $\mathbf{p} = \mathbf{e}_3$  from the strain tensor (as they are parallel to the stress tensor) leads directly to the fault plane normal. The fault plane normal and slip are given by

$$\mathbf{n} = \begin{pmatrix} -\sin(\rho) \sin(\phi) \\ -\sin(\rho) \cos(\phi) \\ \cos(\rho) \end{pmatrix} \quad (4.81)$$

$$\mathbf{d} = \begin{pmatrix} \cos(\gamma) \cos(\phi) + \sin(\gamma) \cos(\rho) \sin(\phi) \\ -\cos(\gamma) \sin(\phi) + \sin(\gamma) \cos(\rho) \cos(\phi) \\ \sin(\gamma) \sin(\rho) \end{pmatrix} \quad (4.82)$$

The extraction of the three parameters strike, slip, and rake is straight-forward. The beachball representation can then be done easily. There are several ways to draw them. In this report the plots are made using the Generic Mapping Tool (GMT) [Wessel and Smith, 1998]. Depending on the used mode during the ALSC (bending plate model or not) the plane fault solutions are either 3-D or just describe strike-slip events.



# 5 Adaptive least-squares collocation: Results

The ALS algorithm was first presented in [Egli *et al.*, 2007] and extended within this thesis (see Chapter 4). This chapter sets its focus on the functionality of the ALS approach. The input parameters and their impact on the given algorithm is illustrated based on a simple generic example. The second part will focus on the extraction of the geodynamic deformations using the CHTRF 2010 solution and precise levelling data.

## 5.1 Generic example

The functionality of the ALS approach will be shown in this section based on a simple and simulated test field. It contains two colliding plates separated by a clear boundary in the middle of the field. Eight measurement points are evenly distributed on each side. All velocities are introduced error-free and their velocities are five millimetres per year. The northern plate is moving to the South and the southern plate to the North (Figure 5.1).

The adaptive part of the ALS technique changes the trend metric based on the strain rate field. The scale defines the maximum allowed ratio between a distance before and after the deformation process.

$$s = \frac{d_{start}}{d_{end}}$$

If the scale is set to one, no deformation is occurring, and the output of the ALS is equal to a normal LSC approach. Apart of the scaling ratio the maximal strain rate  $g_{max}$ , defining at which rate the maximally allowed ratio is applied, and the affected region around the dilatation source, given by the parameter  $\gamma$ , have to be defined before starting the ALS process.

The effect of the dilatation process depends on the chosen scale. To demonstrate the effect of the scale, a range of several values is chosen and applied. Figure 5.2 shows four different scale and their impact to the trend metric.

The effect of the dilatation radius and scale on the velocity and strain rate field is illustrated introducing a profile line perpendicular to the fault. The profile is marked as a red line in Figure 5.2. The velocities and compression rates of the North-South component are plotted using the kilometrage (North: 0 m, fault: 10000 m, and South: 20000 m) in the

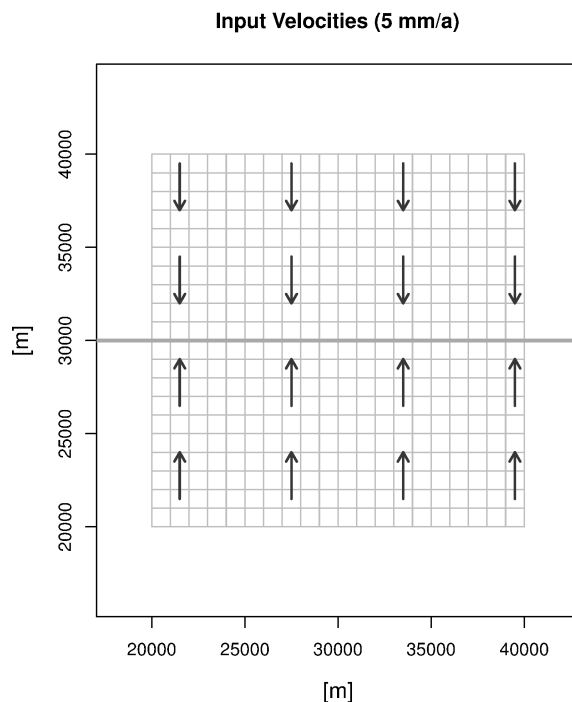


**Figure 5.1:** A simple test field consisting of two colliding plates.

**Table 5.1:** Integrated strain values along the North-South profile. The theoretical shortening is 10 mm.

Scale	Integrated strain (N-S)	Scale	Integrated strain (N-S)
1.00	-7.3 mm	2.00	-8.5 mm
1.25	-7.7 mm	2.25	-8.6 mm
1.50	-8.1 mm	2.50	-8.7 mm
1.75	-8.3 mm	2.75	-8.7 mm

x-axis and the compression rate or velocity in the y-axis. Figure 5.3 shows the resulting velocity and strain rate profiles. A higher ratio will de-correlate points across the fault boundary leading to a faster change of the velocity and higher compression rates.

Both plates have no intra-plate deformations and are colliding with a total velocity of 10 millimetres per year. As the strain rate is the derivative of the velocity field, the integration along the profile line, going from North to South, should reveal a total shortening of 10 millimetres per year. The integration for the eight scale is listed in Table 5.1. The theoretical value is not achieved but with higher ratios the amount gets closer to 10 millimetres per year. With a larger deformation the distance between two points on both plates gets enlarged and their correlation value decreases. Therefore the impact is less and they will be less influenced by the introduced velocities on the other side of the fault.

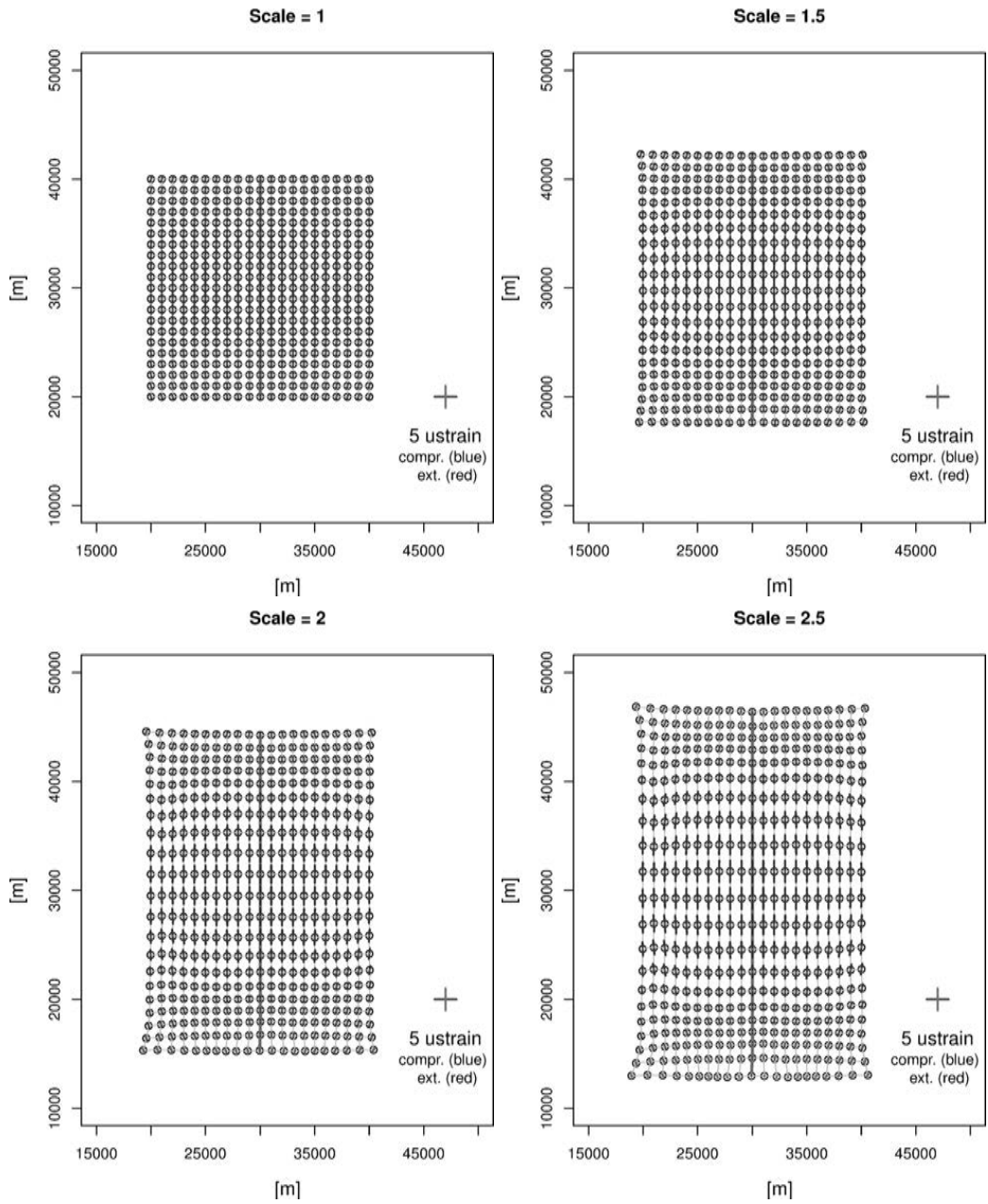


**Figure 5.2:** Strain rate field and the transformed trend metric. The scale varies between 1 and 2.5. The red line represents a profile used for further analysis.  $1 \mu\text{strain} = 10^{-6}$  strain

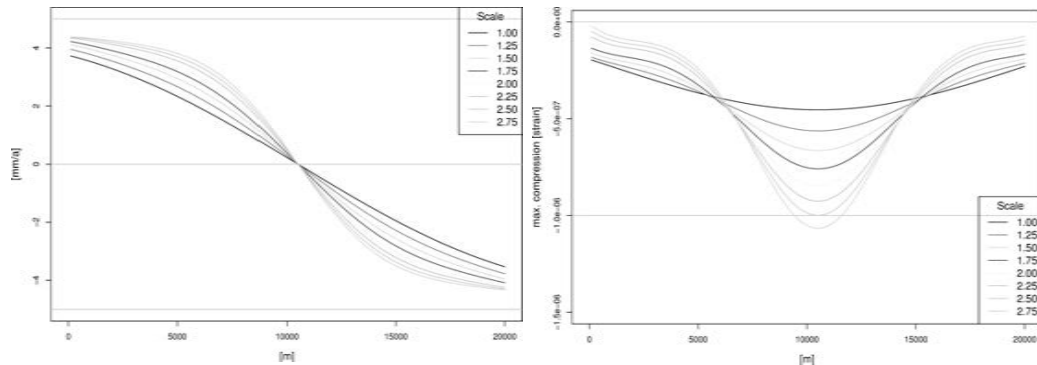


**Figure 5.3:** North-South velocities (left) and maximum compression rates (right) along the given profile using various deformation scales. With higher scales the strain rates get more and more concentrated on the fault.

## 5.2 CHTRF 2010

The horizontal velocities are given by the CHTRF 2010 solution including over 230 point measurements of GNSS campaign-type. The uplift rates are covered by precise levelling data. The combination of both data sets leads to the kinematic field of Switzerland.

The ALSC method is applied to the data in order to obtain the deformation field. However, the technique requires the definition of input parameters which control the deformation process. The parameters, listed in Table 5.2, have an impact on the solution and need to be carefully chosen. To acquire the optimal starting values several sets of parameters are tested to determine the final one. The tests focused on the collocation length and the scale.

**Table 5.2:** Input parameters for the ALSC algorithm.

Parameter	Definition
$\sigma_{trend}$	Assumed to be equal to the mean velocity
$\sigma_{signal}$	Assumed to be zero
$r_{trend}$	Correlation length for the trend
$r_{signal}$	Correlation length for the signal
$s$	Scale (max. change of the distance during one iteration)
$\gamma$	Dilatation influence (distance)

To examine the effect of the two major parameters, the trend correlation length and scales, series for both values are created and computed. The next two sub-chapter will show the outcome of the series in order to choose the input parameters for the extraction of the final kinematic model of Switzerland.

### 5.2.1 Trend correlation length

To test the influence of the trend correlation length a set of starting values covering the range between 40 km and 200 km, with 5 km intervals, is computed. The tests are applied to both models, the 2-D and the thin plane model. The output of the strain rate and velocity fields is shown in Figure 5.4 for the 2-D model, and in Figure 5.5 for the thin plate model. The resulting trend metric, describing the tectonic model, is displayed in Figure 5.6. The other parameters are kept fixed for all tested trend correlation lengths:

- Trend correlation length: 40 – 200 km using 5 km steps
- $\sigma_{trend} = \sigma_{velocity}$
- Signal correlation length: 15 km
- $\sigma_{signal} = 0.00001$
- Scale = 1.25
- $\gamma = 20$  km

After each iteration the trend correlation length gets adjusted until an equilibrium between the three parameters  $\sigma_{trend}$ ,  $\sigma_{signal}$ , and the velocity distribution  $\sigma_{velocity}$  is achieved. The iteration stops when the following relation is fulfilled or the maximum allowed number of iterations is exceeded:

$$\sigma_{velocity}^2 - (\sigma_{trend}^2 + \sigma_{signal}^2) < \text{tolerance} \quad (5.1)$$

The choice of the trend correlation length has a major impact on the resulting strain rate field. The value has to be large enough to cover several sites in order to distinguish between noise and a common, tectonically driven deformation. With a mean inter-station distance of 15 kilometres for the GNSS measurements the length of 60 kilometres covers several sites within its region. A larger value has a higher smoothing effect (see Figure 5.4) and smaller tectonic deformation patterns are lost.

### 5.2.2 Scale

The trend correlation length has been set to 60 km for the scale tests. Therefore, the following values are used to determine the influence of various scale:

- Trend correlation length: 60km
- $\sigma_t = \sigma_x$  with  $\sigma_x$  as the mean velocity.
- Signal correlation length: 15 km
- $\sigma_s = 0.00001$
- Scale s: 1.00 – 3.00 using 0.25 steps
- $\gamma = 20$  km

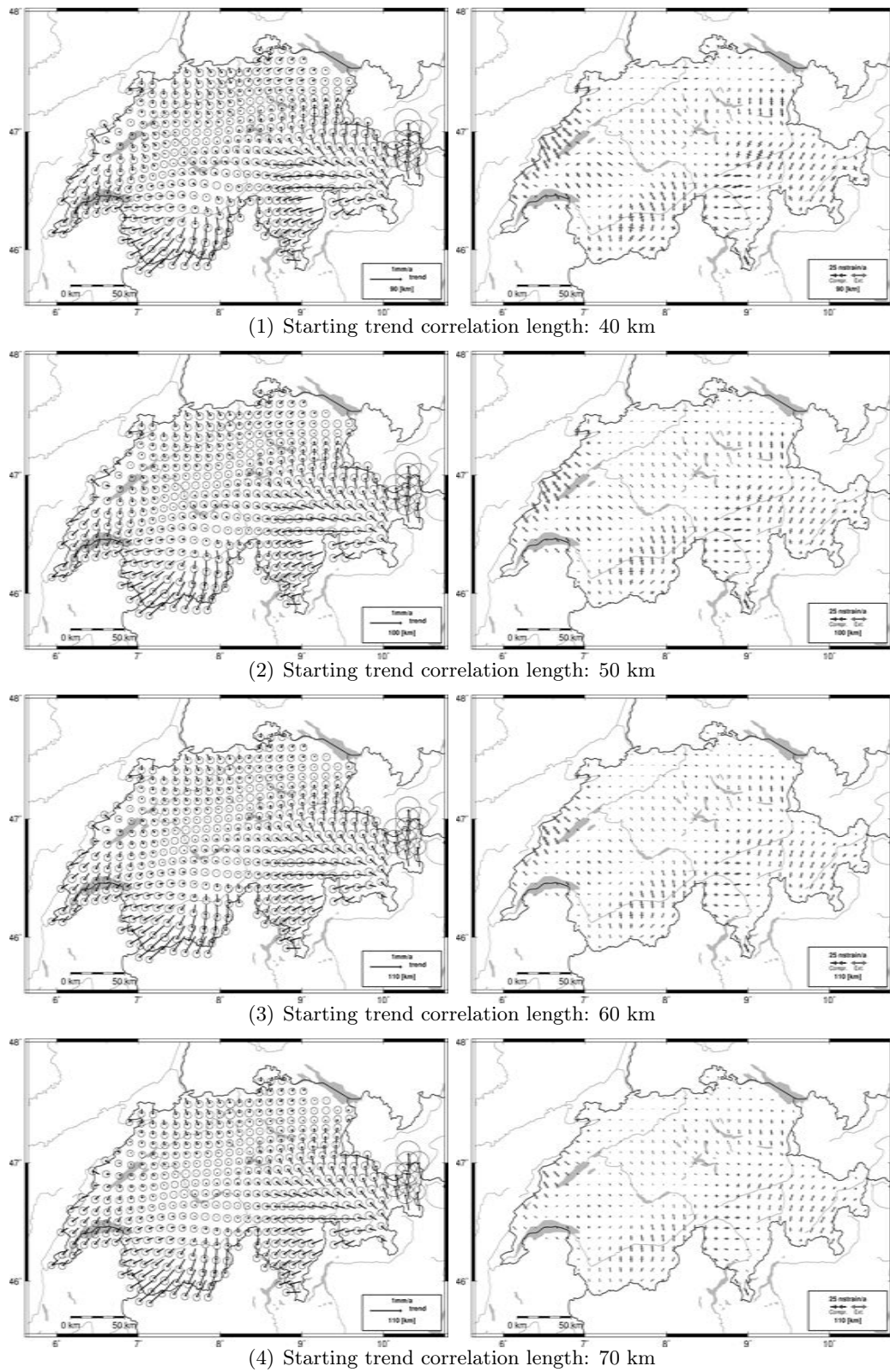
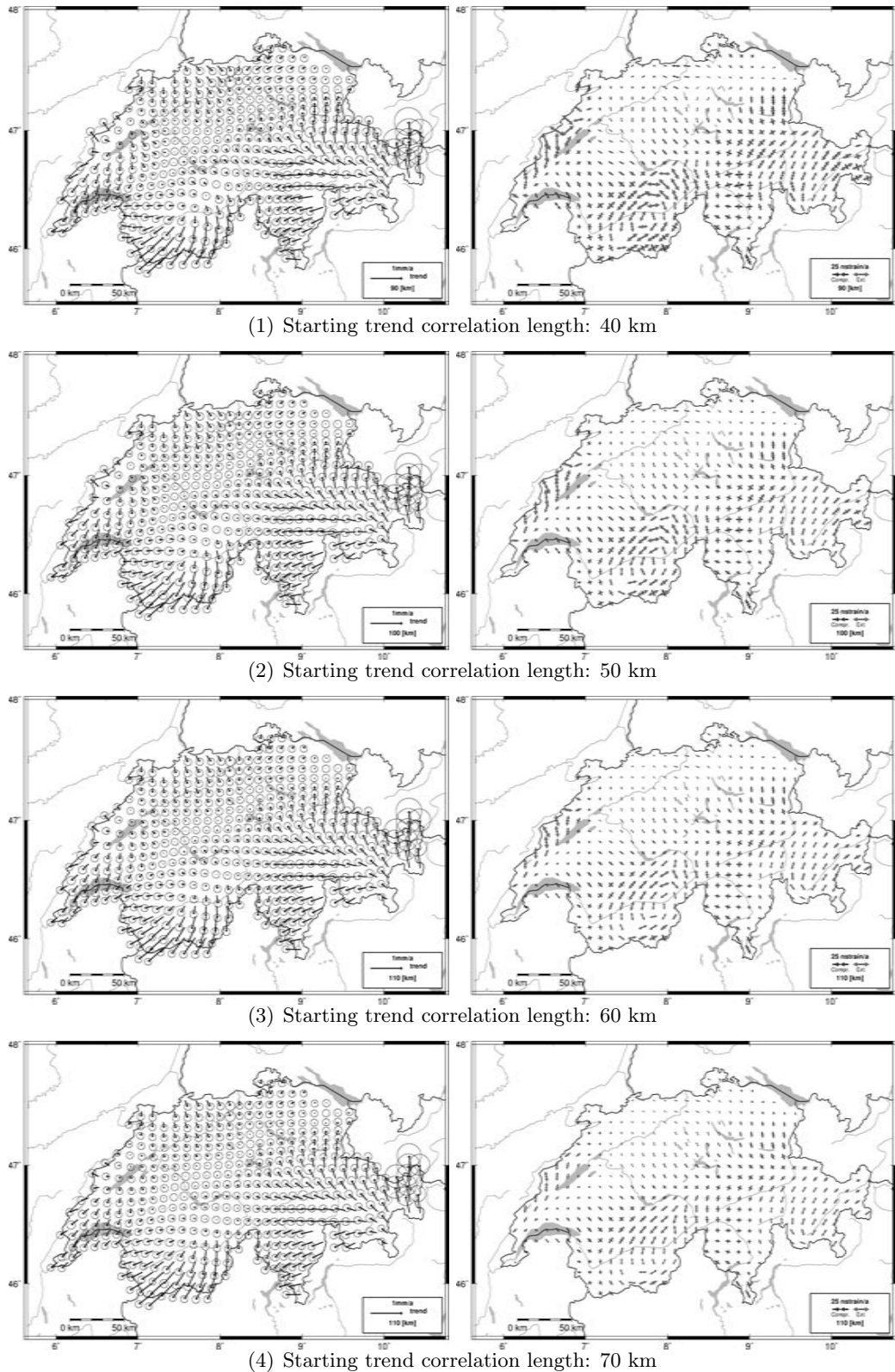
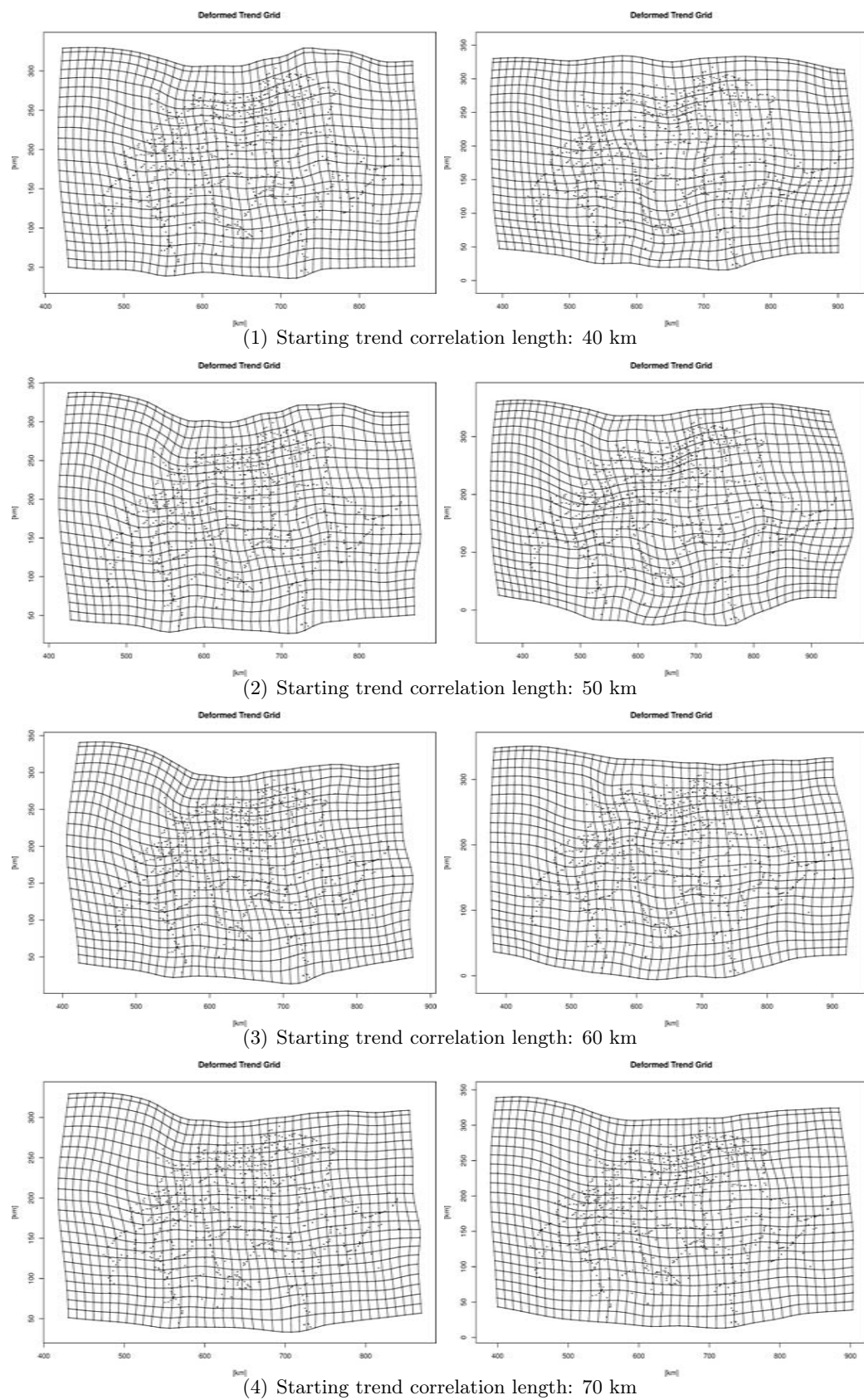


Figure 5.4: Tectonic deformation (left) and strain (right) derived from a 2-D strain model.



**Figure 5.5:** Tectonic deformation (left) and strain (right) derived from a thin plate model (3-D strain).



**Figure 5.6:** Trend metric grid which is used for the correlation between two points. Used strain model: (left) 2-D and (right) 3-D.

The resulting trend metrics for the various scales are shown in Figure 5.7. The scale in the plots changes with increasing scale value. The scale defines the effect of the strain rate field on the trend correlation length and, therefore, has a direct influence on the velocity and strain rate field. The resulting velocity and strain rate fields are displayed in Figure 5.8. The corresponding strain rate fields using the thin plate model are shown in Figure 5.9.

The choice of the scale is the second parameter, apart from the correlation length, with a huge influence on the resulting kinematic field. The tests (Figure 5.8) reveal that a ratio above 1.5 leads to very inhomogeneous fields which is not realistic. Therefore, the choice was between the scale values 1 and 1.5, where the mean value of 1.25 is introduced for the final evaluation. The distance between two points will, therefore, be enlarged by a maximum of 25 percent during each iteration.

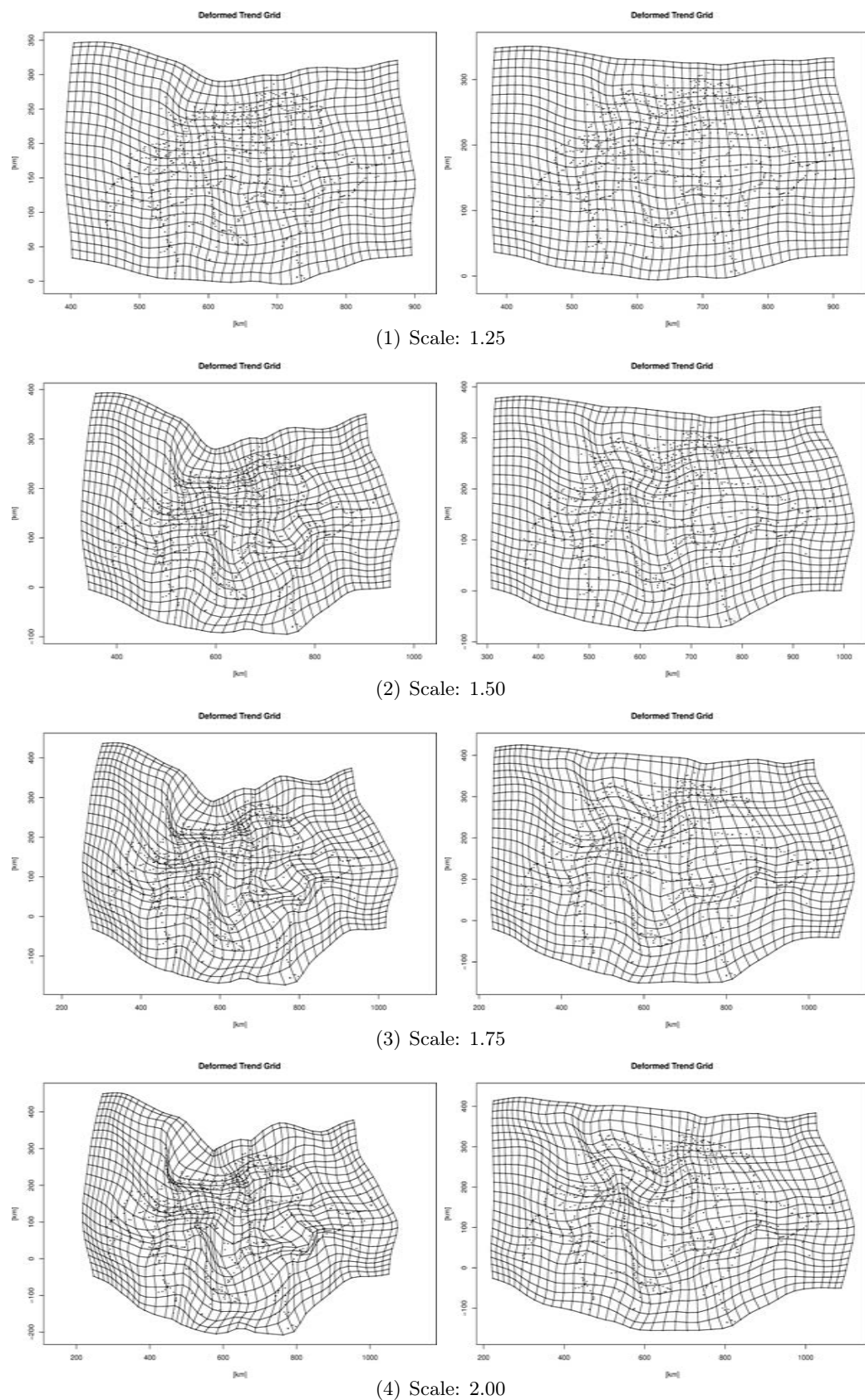


**Figure 5.7:** ALSC collocation using scale rates from 1.25 to 2. The trend correlation length is 60 km. The plot scale changes between the plots. Left: 2-D model, Right: 3-D Model.

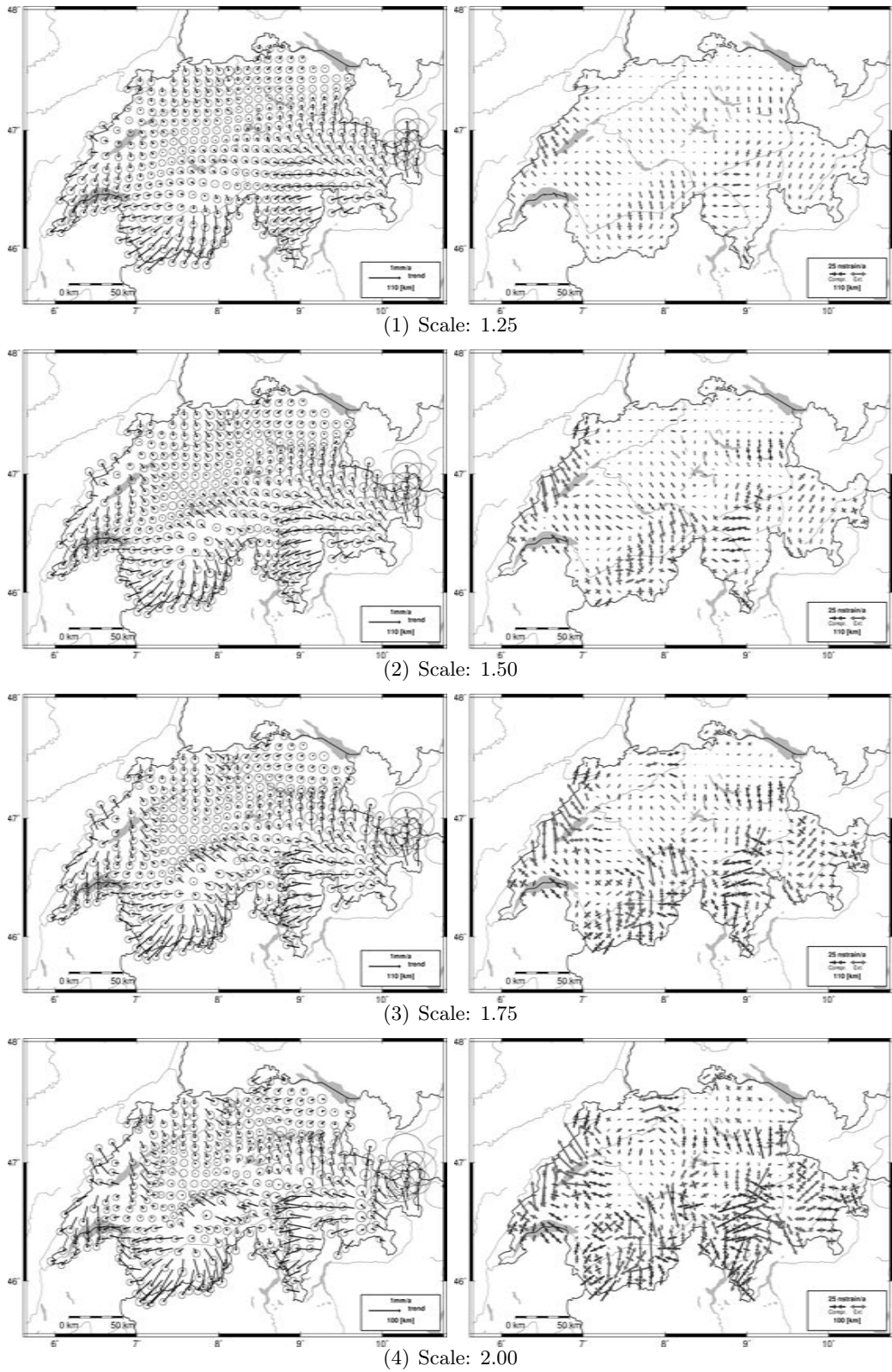
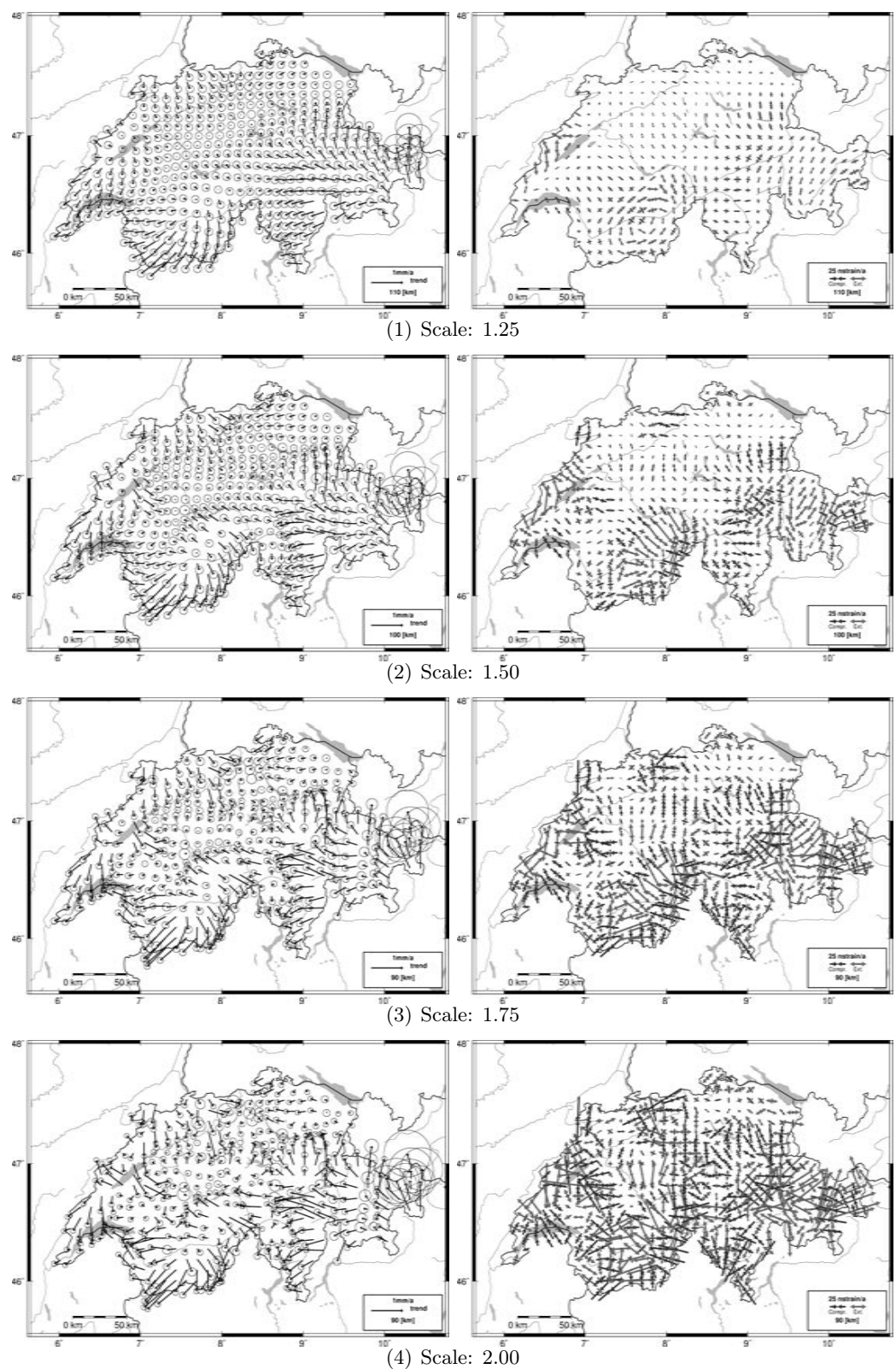


Figure 5.8: 2-D model: Tectonic deformation and strain derived using a 2-D strain model.



**Figure 5.9:** Thin plate model: Tectonic deformation and strain derived using the 3-D strain model.

### 5.2.3 Final solution

The tests from the previous sections lead to the chosen parameters, scale, and trend correlation length for the final collocation solution. The correlation length is set to 60 kilometres and the corresponding scale to 1.25. The second stochastic part, the signal, has a correlation length of 15 kilometres. This is the mean distance between the GNSS measured points. In addition to these parameters the  $\gamma$  value was set to 20 kilometres. The list of starting values to obtain the final kinematic model for Switzerland is:

- $\sigma_{trend} = \sigma_x$
- $\sigma_{signal} = 0$
- $r_{trend} = 60$  km
- $r_{signal} = 15$  km
- $s = 1.25$
- $\gamma = 20$  km

The processing is done for both models, the 2-D and the thin plate model. The final solution consists of the tectonically driven (trend, Figure 5.10) and local (signal, Figure 5.11) velocity field. The signal part has a clear different pattern at 8° E / 46.5° N from the rest of the field. This is caused by two points nearby where their velocities are diametrically opposed to each other. The uplift rates are shown in Figure 5.12 and the corresponding 1- $\sigma$  error in Figure 5.13. The strain rate tensors shown in Figure 5.14 has been aligned to the eigenvectors and -values: the main compressional and extensional axes. To map the strain rate tensor in 3-D an additional representation is introduced, the beachball. It shows the fault plane solutions derived from the strain rate tensor. The 2-D tensor leads to strike-slip events whereas the 3-D model covers also normal and thrust faulting. They are shown in Figure 5.18.

For a better interpretation of the extracted strain rate field additional representations are created. The maximum compressional and extensional strain rates are plotted in Figure 5.15 and 5.16. The maximum shear strain rate is shown in Figure 5.17. The residuals, containing the remaining measurement noise, are displayed in Figure 5.19 (horizontal component) and Figure 5.20 (uplift component).

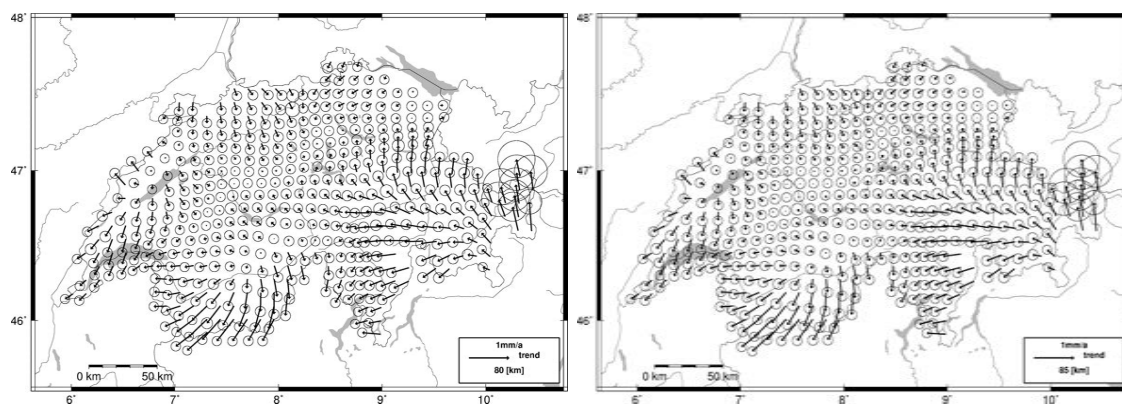


Figure 5.10: Trend: Tectonic velocities (with  $1\text{-}\sigma$  error ellipses) (left: 2-D, right: 3-D).

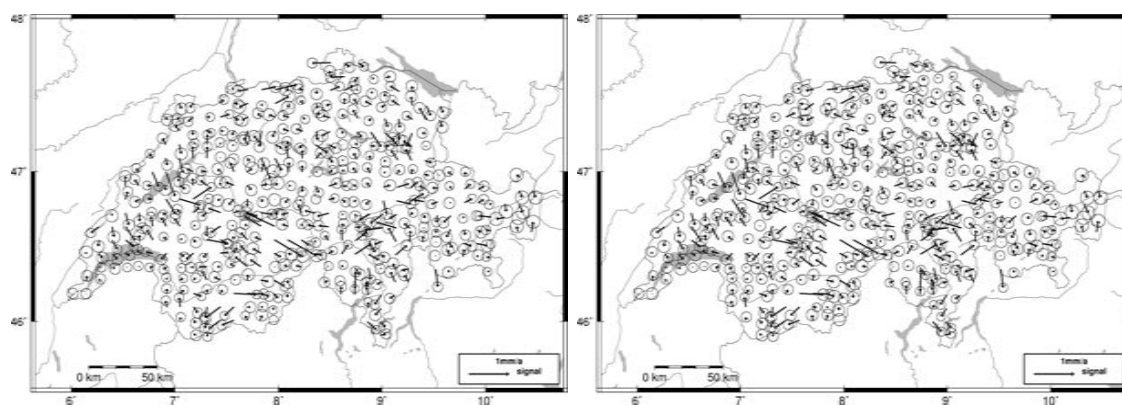


Figure 5.11: Signal: Local deformations (with  $1\text{-}\sigma$  error ellipses) (left: 2-D, right: 3-D).

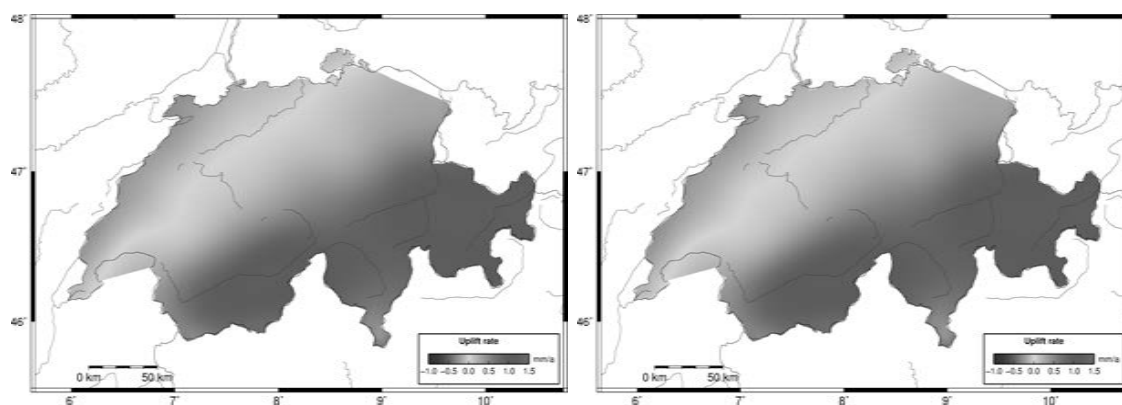


Figure 5.12: Uplift rates (left: 2-D, right: 3-D).

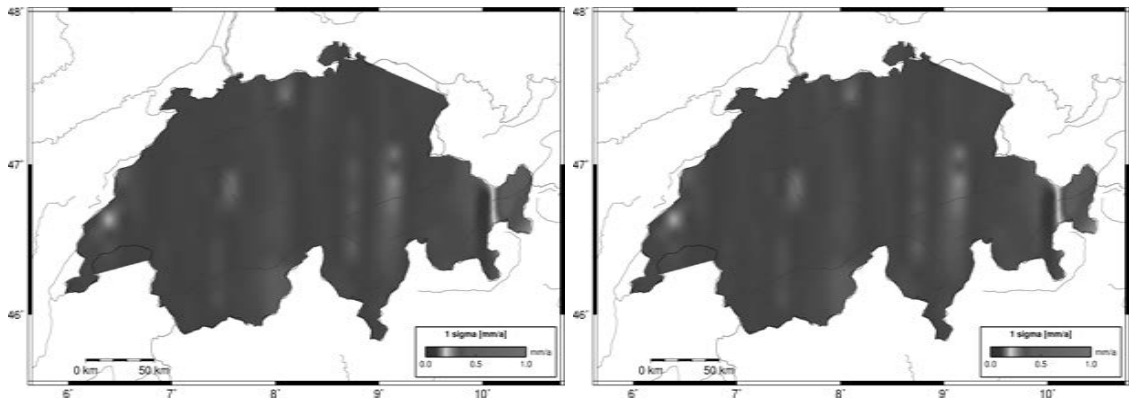


Figure 5.13: Uplift rates error ( $1 \sigma$ ) (left: 2-D, right: 3-D).

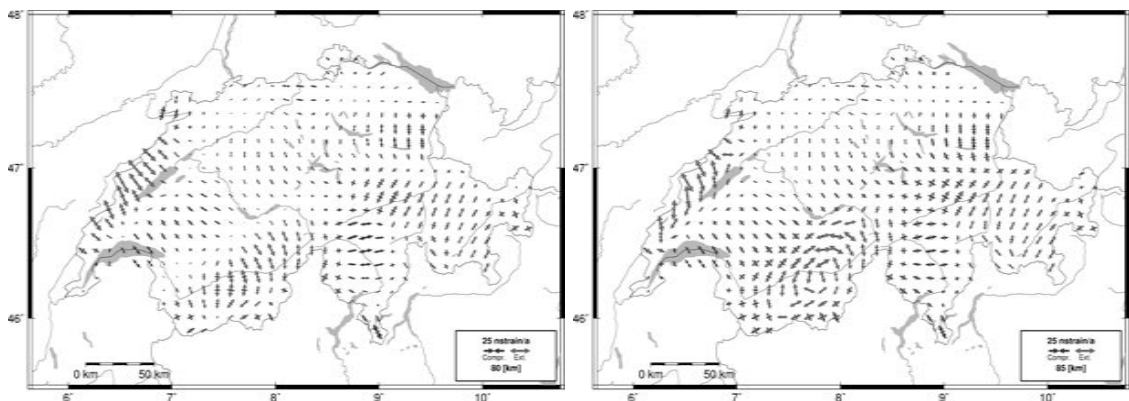


Figure 5.14: Strain rates (left: 2-D, right: 3-D).

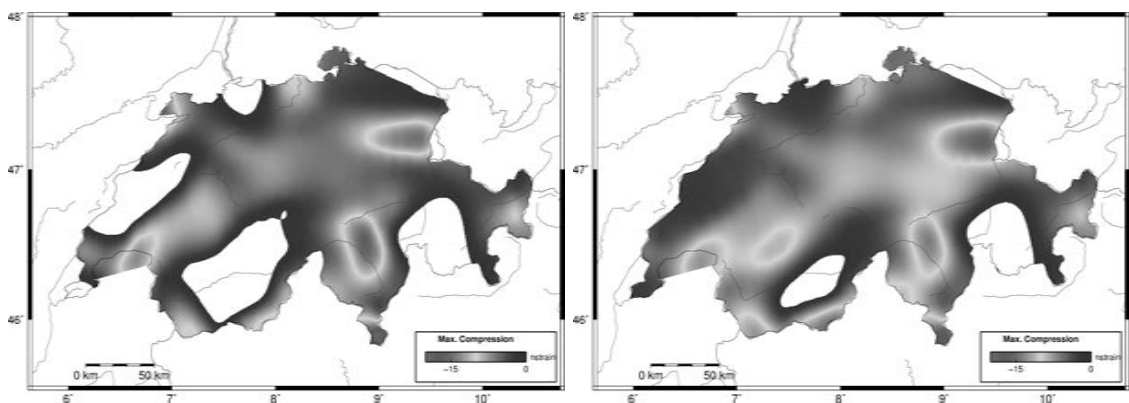
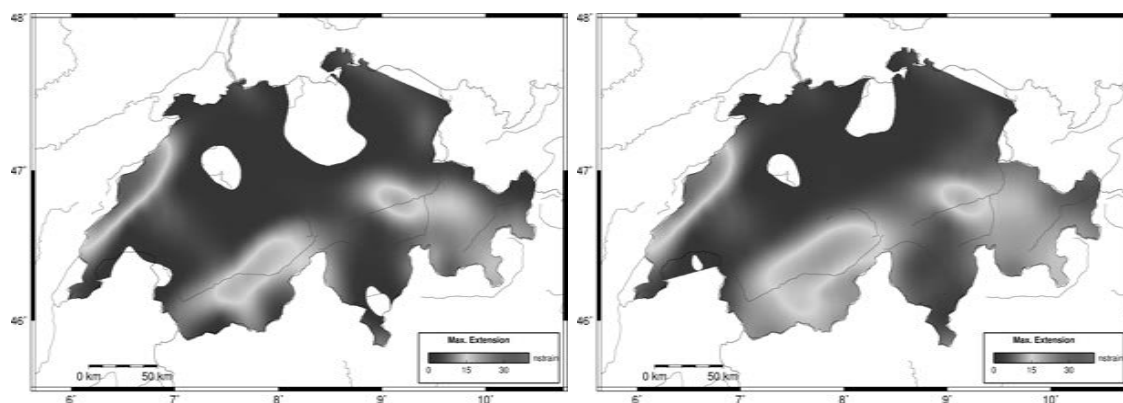
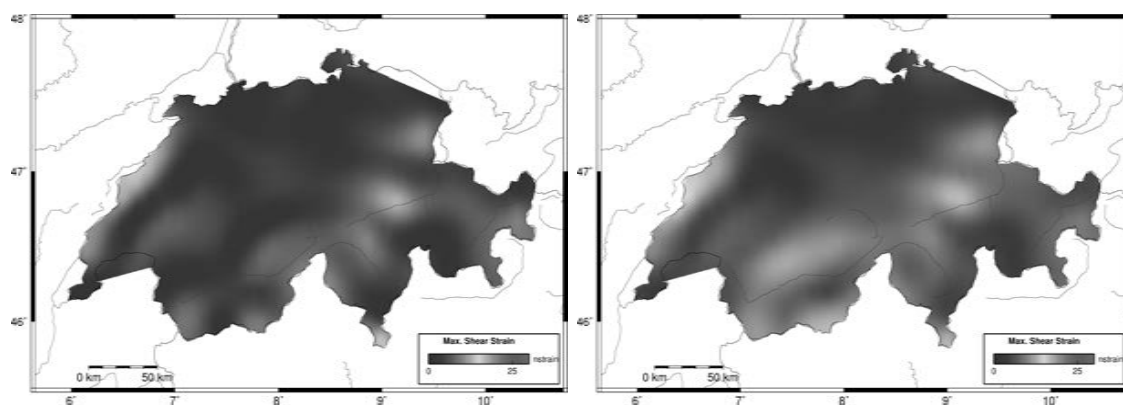


Figure 5.15: Maximum compressional strain (left: 2-D, right: 3-D). White areas represent regions where extensional values occur only.



**Figure 5.16:** Maximum extensional strain (left: 2-D, right: 3-D). White areas represent regions where compressional strain rates occur only.



**Figure 5.17:** Maximum shear strain rate (left: 2-D, right: 3-D).

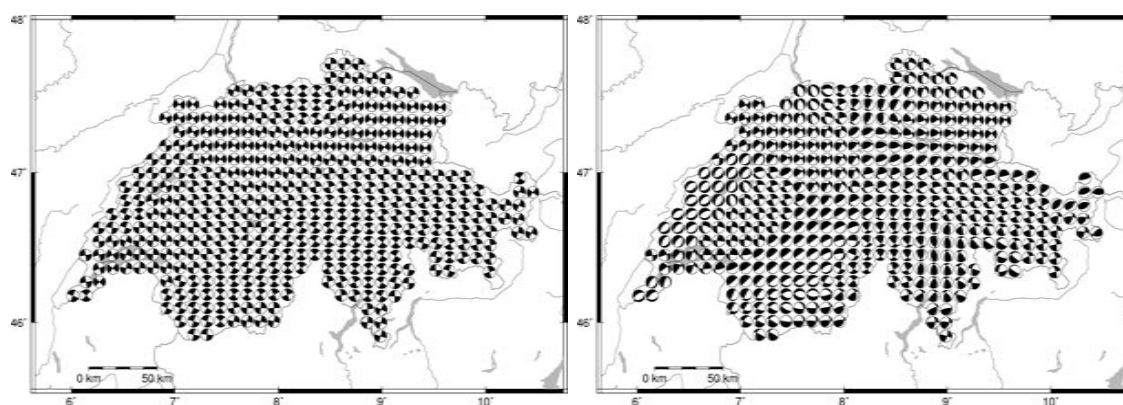


**Figure 5.18:** Fault plane solutions calculated from the strain rate tensors represented as beach balls (left: 2-D, right: 3-D).

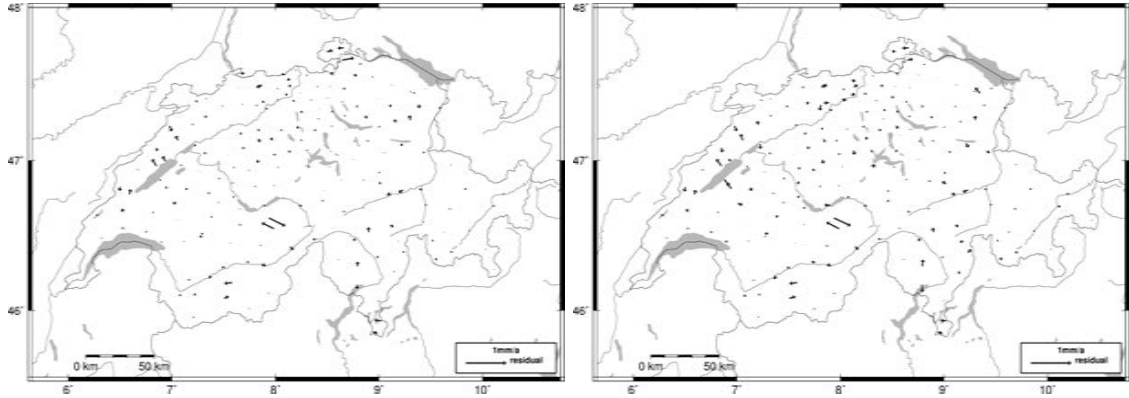


Figure 5.19: Horizontal residuals (left: 2-D, right: 3-D).

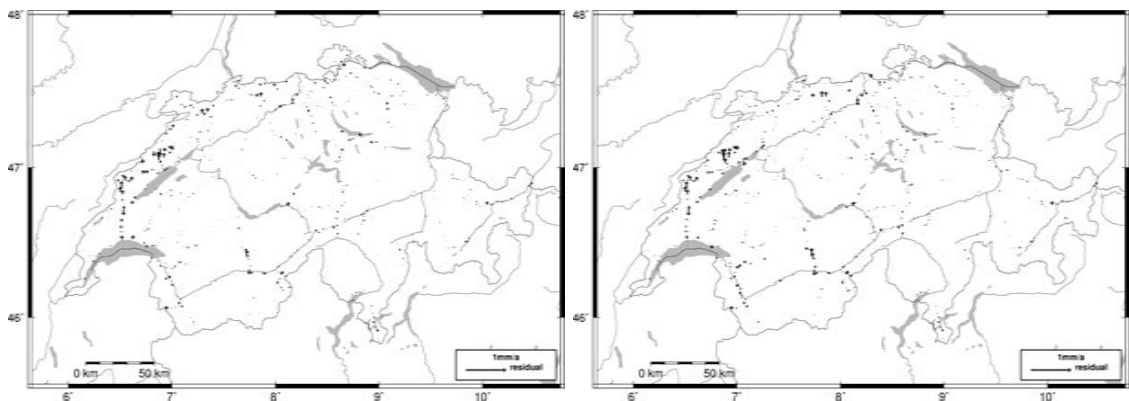


Figure 5.20: Uplift residuals (left: 2-D, right: 3-D).



## 6 Comparison of the strain rate field with geophysical findings

The analysis of the CHTRF 2010 velocities and precise levelling uplift, described in the previous chapter, lead to, among others, the tectonically driven deformation, the strain rate tensor field, and their formal errors. Due to the lack of accessibility to geodetic measurements along the vertical line towards the Earth centre, only the surface deformation can be extracted. These velocities can only be derived along the horizontal axes and it is not possible to extract a full 3-D strain rate tensor. For most comparisons and interpretations the 2-D strain rate tensor is sufficient.

The 3-D model, introduced to extract the uplift strain rate, is the thin plate assumption leading to a 3-D tensor with non-zero vertical strain rates. However, due to the thin plate model additional parameters have to be introduced in order to calculate the strain rates. The method needs the Poisson constant to describe the material's compressibility and the thickness of the plate. Assuming that the Moho discontinuity describes the lower boundary of the crust, the Moho depth corresponds to the plate thickness. The thickness of the Moho is taken from the model calculated by *Baumann* [1994].

### 6.1 Kinematic Model of Switzerland

The final velocity field and its standard deviation are shown in Figure 6.1 (horizontal component), Figure 6.2 (vertical component), and the corresponding strain rate tensor field (eigenvectors and -values) in Figure 6.3. The strain rate formal errors are shown individually in Figure 6.4. The left plot represents the standard deviation of the most extensional and the right one of the most compressional eigenvalue.

The 2-D model reveals clear trends for the tectonic deformations. Along the Alpine front a compression perpendicular to it is observed. In the canton of Valais, South-West of Switzerland, extension is observed. The Jura regions, North-West, has a clear extension. However, this has to be interpreted with caution. It might be introduced due to local effects at various sites along the northern shore of the lake Neuchâtel where the slope is sliding southwards towards the lake. The region of Basel, located at the southern end of the Upper Rheingraben, which is known for its catastrophic earthquake in 1356, has almost no deformation. This might be caused by missing GNSS campaign measurements north of the Swiss borders. Most of the observations are carried out within the country as the

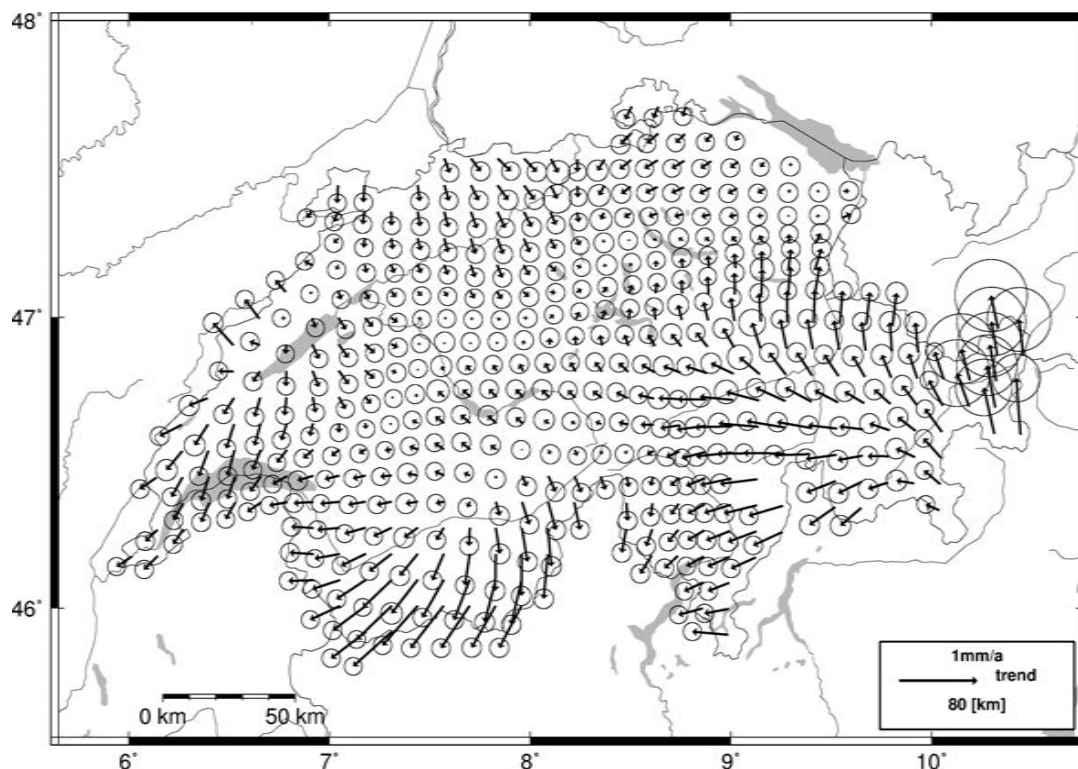


**Figure 6.1:** 2-D Model: Horizontal velocity field with its formal errors extracted from the CHTRF 2010 solution.

main purpose of the campaigns is the verification of the Swiss terrestrial reference frame. For a reliable conclusion on the strain rates in this area, including measurements covering the southern part of the Upper Rheingraben is essential.

Figure 6.5 shows the maximum value of either compressional or extensional strain rates. It becomes visible, that the Swiss Molasse Basin is majorly governed by compression whereas in the Alps the extension rate is higher. Between the eastern and western part of the Alps a compression line from North to South is detected. As mentioned before, using a simple thin plate model allows to estimate a 3-D strain rate tensor. The 3-D strain rate tensor can be expressed using the so-called beachball representation showing the corresponding fault plane assuming isotropic material. It is discussed in Section 6.4.2.

Wiget *et al.* [2007] applied the ALSC method, introduced in [Egli *et al.*, 2007], to the levelling data and the CHTRF 2004 solution. Compared to the new solution, obtained during this work and discussed during this chapter, it has different deformation rates. The biggest difference is in the North-East part of Switzerland where the old velocity field has a westwards velocity of over 0.5 mm/year whereas the new data indicates no deformation for this part. The strain rate tensors have similar precision. It can be seen that in general the strain rates are lower in the new processing mainly caused by the new CHTRF 2010 solution which led to lower velocities.

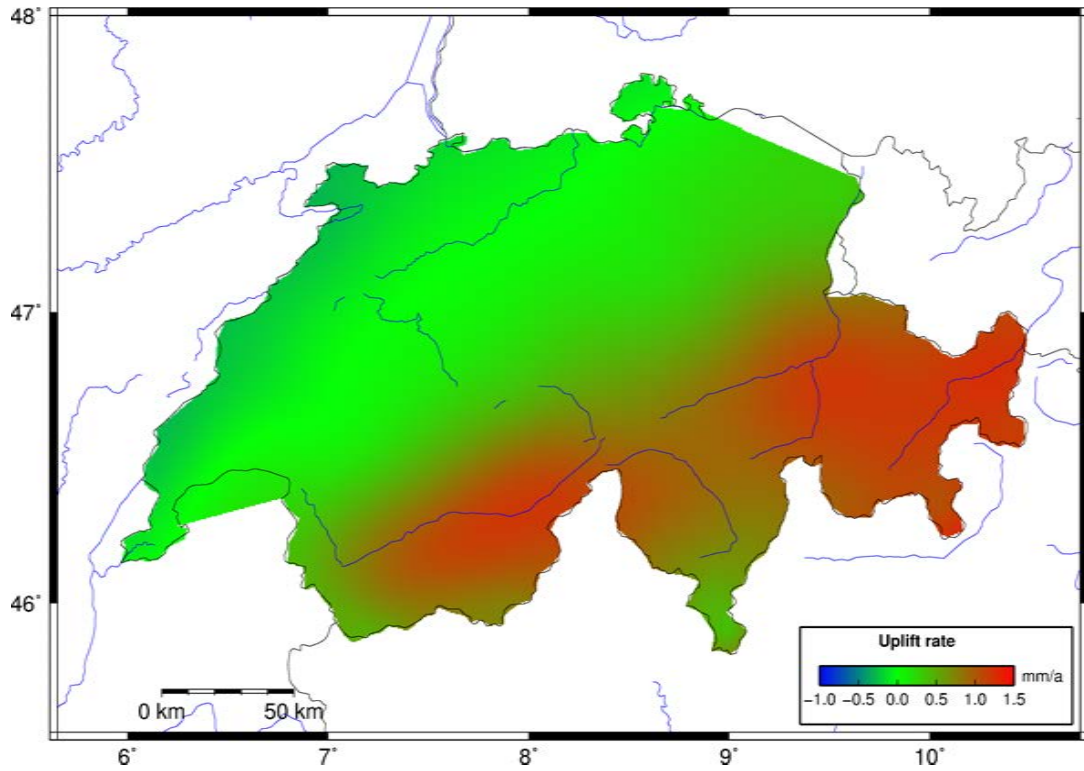


Figure 6.2: 2-D Model: Vertical velocity field based on precise levelling data.

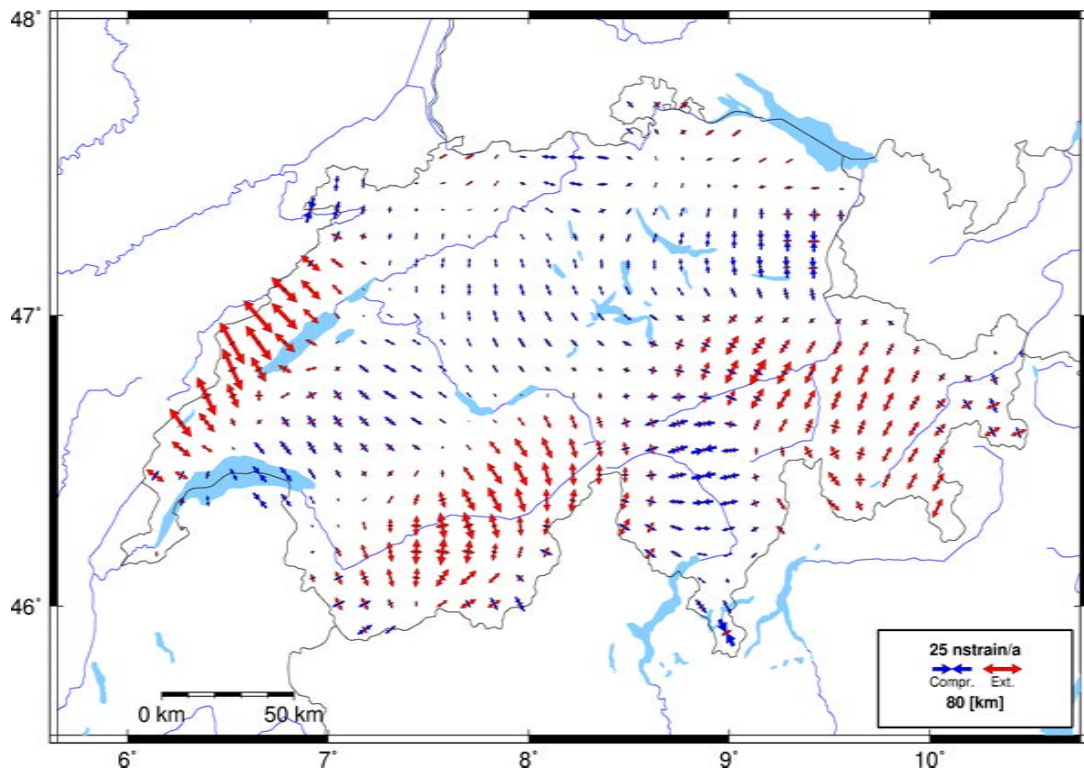
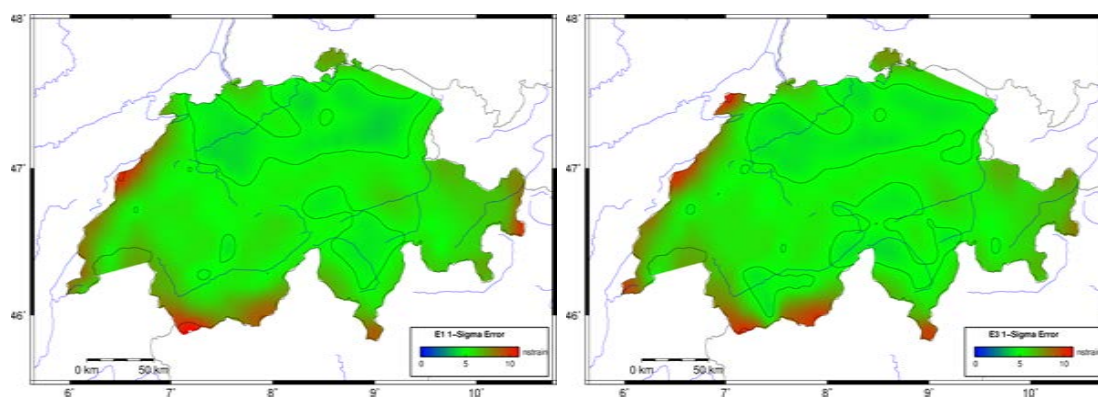
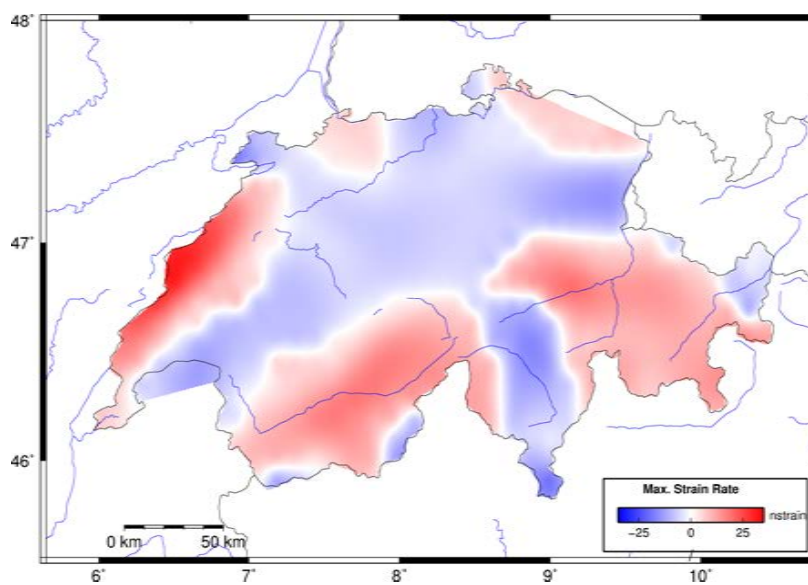


Figure 6.3: 2-D Model: Horizontal strain extracted from the CHTRF2010 solution.



**Figure 6.4:** 2-D Model: Standard deviation ( $1 \sigma$ ) of the most extensional (E1, left) and most compressional (E3, right) strain rate.



**Figure 6.5:** Maximum compressional or extensional strain rates.

## 6.2 Strain Energy

The surface deformation field describes the uppermost part of the crust. However, under some assumption it is possible to derive the built-up strain energy per square kilometre. The strain energy is built-up over time and may be released by earthquakes if a critical level is reached. This depends, among others, on the rheology of the crust and existing faults. The yearly built-up strain energy can be estimated but the total amount remains unknown. The strain energy density per year reveals areas where high energy is built-up indicating higher seismic hazard.

The strain energy is estimated for both models: the 2-D and the thin plate model. Both models need the crustal thickness, to determine the built up energy and in the thin plate model to estimate the bending part of the strain rate tensor. It is assumed that the crust goes down to the Moho discontinuity. For Switzerland, the Moho discontinuity has been studied in several publications [Baumann, 1994; Waldhauser *et al.*, 1998]. The Moho depths published by [Baumann, 1994] are used for the strain energy calculation.

To test the quality of the models they have to be compared to independent energy estimations. Therefore, the comparison is made to energies obtained by analysing the released energy from earthquakes. The resulting energies are published in [Rüttener, 1995].

### 6.2.1 2-D model

For the simple 2-D model the uplift strain rates are assumed to be zero and the horizontal deformation rates to remain constant over the whole thickness of the crust as described in Section 4.5 using Equation (4.65). The derived strain energy is displayed in Figure 6.6 and amounts to values from 7 MJ/km<sup>2</sup> to 1.91 GJ/km<sup>2</sup> per year.

### 6.2.2 3-D model

The strain energy calculation based on the thin plate model is described in Section 4.5 using Equation (4.76). It includes, apart from the horizontal deformation rates, which remain constant over the whole crust thickness, a bending part which leads to non-zero upward strain rates. Figure 6.7 shows the strain energy built up by the horizontal component and the total strain energy including the bending part is displayed in Figure 6.8. The maximum strain energy density is located in the Alps. In the central part of the Alps a density drop of the strain energy is visible.

### 6.2.3 Conclusion

The energy released by earthquakes is analysed in [Rüttener, 1995]. He covers several time intervals: 1975–1993 (instrumental time period), 1850–1974, and 1300–1850 (historical

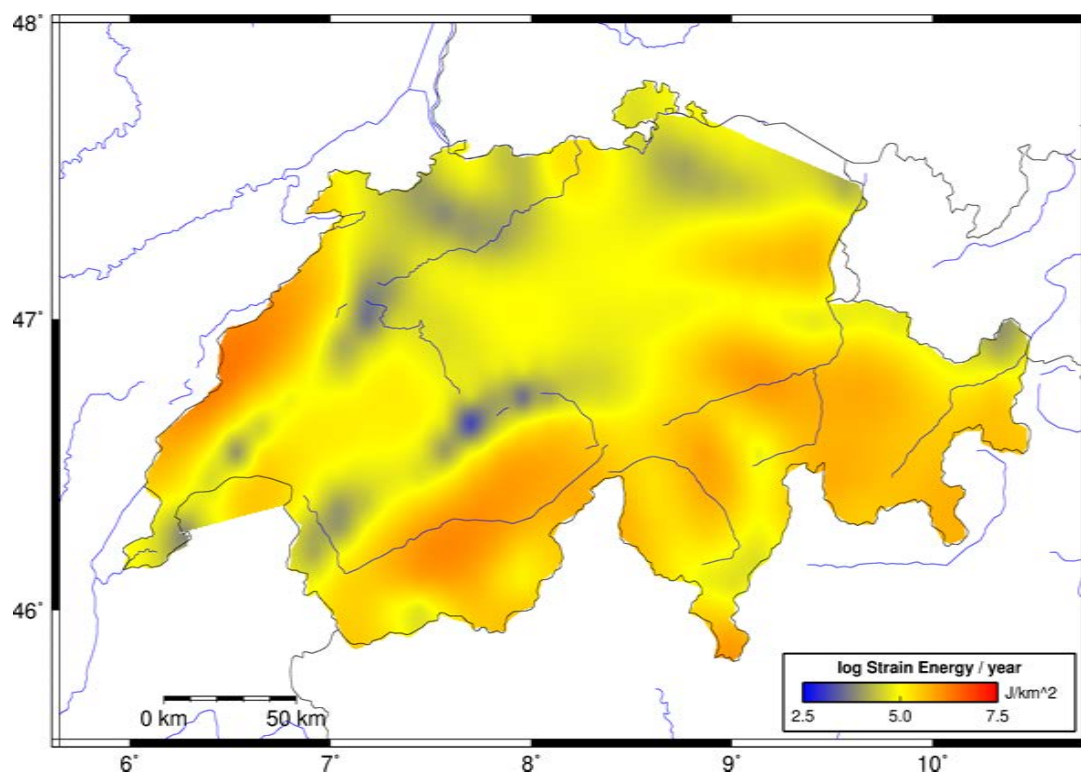


Figure 6.6: 2-D model: Strain energy.

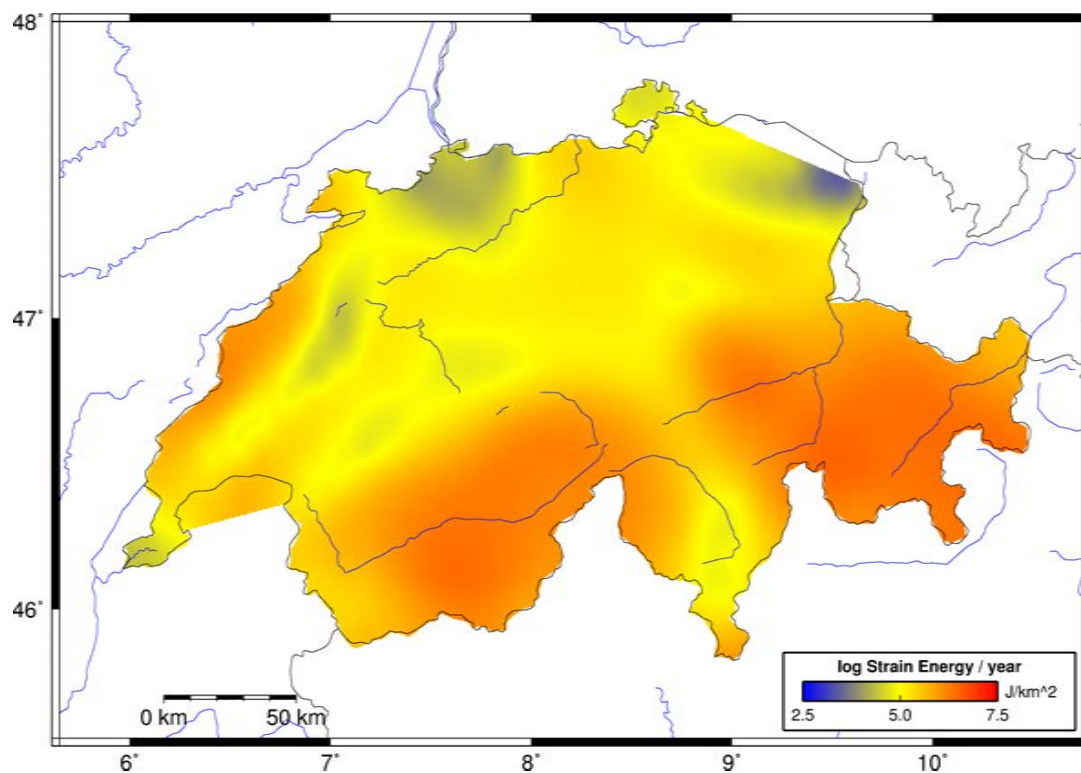
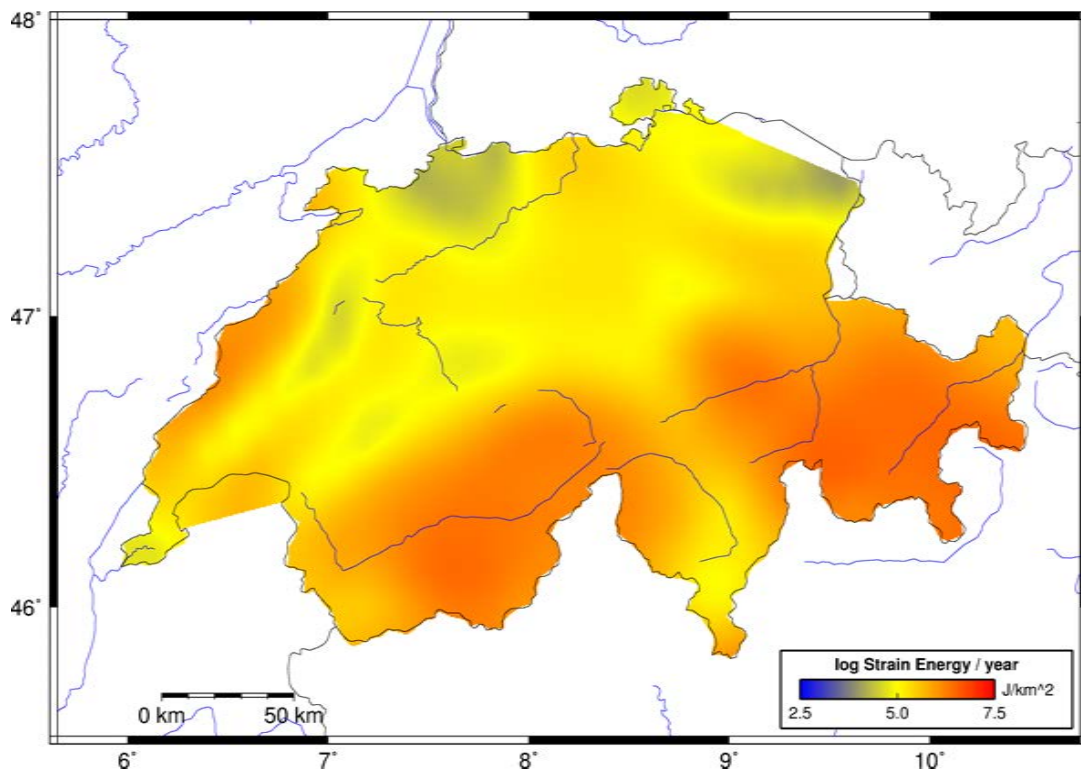


Figure 6.7: 3-D-model: The strain energy caused by the horizontal component remaining constant along the plate thickness.



**Figure 6.8:** 3-D-model: The total strain energy including the horizontal and the bending part. The strain ranges from 0.14 to 3.82 GJ/km<sup>2</sup> per year.

time periods). These estimated energy rates are between  $10^2$  and  $10^{10}$  Joules/a per square kilometre. The earthquake depths have a clear pattern within Switzerland. Over the Swiss Molasse Basin the seismic layer goes down to 25 kilometres. Under the Alps the seismic layer has a thickness of 20 km. The Moho discontinuity is in the Swiss Molasse Basin 30 kilometres below the surface and goes down to 50 kilometres below the Alps. Therefore, the comparison between the seismically released energy and the strain energy might not match due to this fact. Additionally, not all built up energy might be released through earthquakes and the observed time periods are not identical. The solutions from earthquakes goes back to events around 1300 whereas the strain energy only covers the last 20 years. The tectonic deformation is estimated as a linear velocity over time. This assumption might not be correct as the geodynamically driven deformation might have changed in the past.

The 2-D strain energy is lower than the 3-D strain energy as it does not include the vertical strain rates. The maximum energy rates for the 2-D model are  $1.91 \text{ GJ/km}^2$  per year and for the 3-D model  $3.82 \text{ GJ/km}^2$  per year. With the 3-D model the full strain rate tensor is used including the bending energy. The upward strain component leads to a higher energy density as the uplift strain rate is included in the calculations. The bending part adds additional strain energy into the alpine regions as the plate thickness in the bending part equation is cubic.

### 6.3 Strain rate tensor comparison

The resulting strain field based on the ALSC algorithm represents the surface deformation. The impact of the extracted strain rate tensor on existing faults can be derived by mapping the strain rate tensor onto the fault. It can then be represented by the shear force acting onto the fault plane and the force perpendicular to it (extension or compression). The result of the projection is shown in Figure 6.9 (left: compression and extension, right: shear strain). A detailed view on the North-East part is given in Figure 6.10.

The strain projection onto the fault around Fribourg, marked as F in Figure 6.10, with a NNE-SSW direction has a sinistral strike-slip mechanism based on the GNSS measurements. *Kastrup et al.* [2007] studied the faults in this region with geophysical methods and came to the same conclusions.

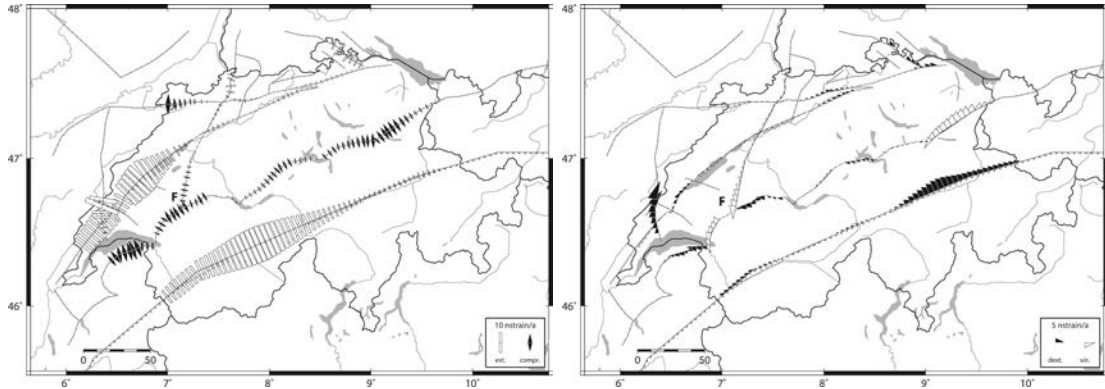


**Figure 6.9:** Strain rate tensor mapped onto known faults. Left: Normal strain perpendicular to the fault orientation. The white bars indicate extension (normal faulting) and the black triangles compression (thrust faulting). Right: Shear strain resulting from the interpolated strain field. Black triangles indicate dextral and the white triangle represent sinistral motion.

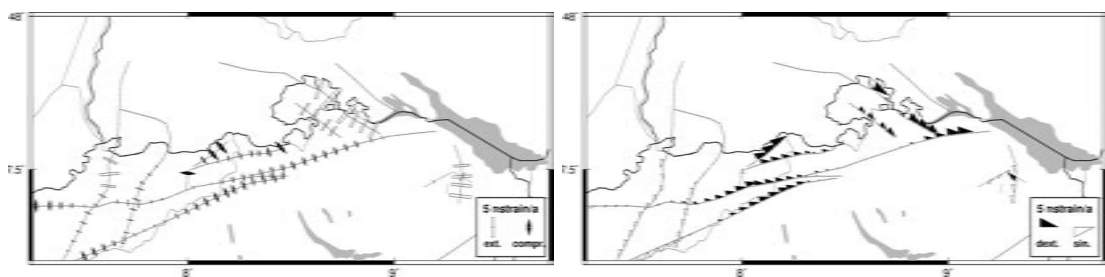


**Figure 6.10:** Strain rate tensor mapped onto known faults. Detailed view of the North-East part of Switzerland.

## 6.4 Comparison with seismic findings

If the strain energy is stored and released by earthquakes, the fault mechanism should correspond to the geodetic strain values. However, as the upward strain component is not well determined by geodetic measurements, disagreement between both methods may occur.

### 6.4.1 Stress regimes

The stress regimes can be extracted from fault plane solutions. This process needs data sets of the earthquake solutions which can be divided into several clusters to obtain their main stress regimes. This work was done by [Kastrup *et al.*, 2004] using events from 1961 to 1998 resulting in several stress regimes for the analysed earthquake clusters. Due to the scattering of the available fault solution it was not possible to determine the stress regimes for the eastern Alps. The publication of [Marschall *et al.*, 2013], which analyses these clusters again using additional earthquake sources (1998–2011), describes the obtained stress regimes for this region. The regimes obtained in these publications can be compared to the strain rate tensors estimated from geodetic measurements.

Figure 6.11 shows the 2-D strain rate tensor overlaid by the retrieved seismic stress regimes. The results have a remarkably good fitting and confirm the reliability of the extracted strain rate tensor. However, the comparison can only be made for the extensional and compressional axis directions as the absolute strain rate value is not known.

### 6.4.2 Comparison of fault plane solutions

The Swiss Seismological Service (SED)<sup>1</sup> releases the fault mechanism for earthquakes on their web-page. The catalog contains earthquakes with a magnitude (M<sub>w</sub>) above 3.4 since 2004. The recorded and reconstructed fault solutions are plotted (black) together with the fault solution described by the 3-D strain rate tensor at the corresponding depth of the event (red) in Figure 6.12 and overlaid onto the geodetic fault plane solutions at the surface in Figure 6.13. The earthquake solutions are mostly in good accordance with the fault plane solutions obtained using the thin plate model.

The fault plane solutions derived from the geodetic strain rate tensors depends on the input parameters used in thin plate model. The thickness of the plate has a major impact on the calculated fault solution and may change the extracted mechanism. This can be seen in the earthquakes located in the Canton of Graubünden. The two earthquakes from 2008 and 2009 have a different mechanism, based on the geodetic strain rate tensor, between their hypocentre and epicentre. The hypocentres indicate a normal faulting mechanism whereas

---

<sup>1</sup>Catalogue obtained from the SED-homepage: [http://www.seismo.ethz.ch/prod/tensors/mt\\_list/index](http://www.seismo.ethz.ch/prod/tensors/mt_list/index), accessed: 2013/12/01

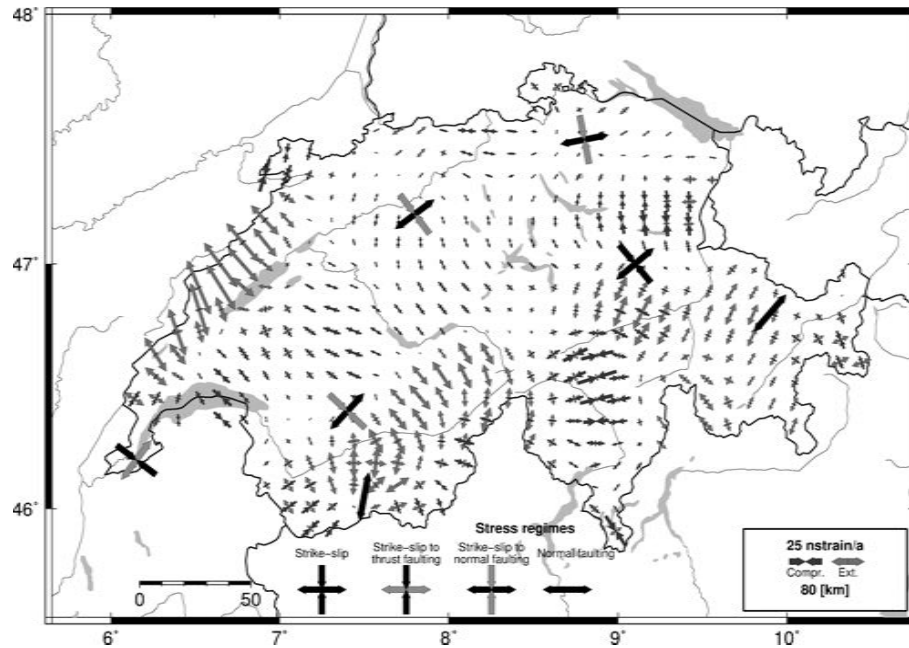


**Figure 6.11:** Comparison of stress regimes [Kastrup *et al.*, 2004; Marschall *et al.*, 2013] and the 2-D strain field.

the epicentre have strike-slip mechanism. The latter mechanism is in good agreement with the seismic fault solution. This phenomena can be observed on various earthquake solutions and is caused by almost identical values for the most compressional and intermediate eigenvalues. A small change of these values might switch their order changing the tension  $t$  and pressure  $p$  axes. This leads then to different fault planes as it is calculated using these two directions only.

### 6.4.3 Comparison with p-axis from earthquake solutions

The most compressional axis can be extracted from the horizontal strain rate field. It shows the direction of the major shortening axis. On order to validate the extracted information it has to be compared to data obtained by other methods. To achieve this, the earthquake catalog published by [Kastrup *et al.*, 2004; Marschall *et al.*, 2013] is used which contains the source mechanism with the corresponding t- and p-axis. The p-axis is the counterpart to the strain shortening axis. If the strain field represents the deformation well, even if it does only cover up to 20 years of data compared to the seismic catalog with over 60 years, both axes should fit. Figure 6.14 shows the strain compression from GNSS (black line) and the p-axis from earthquakes (red line). Figure 6.15 displays the shortening direction for both methods for each earthquake. The colour map represents the angle between the two axes. It can be seen that for most parts the fitting is good. However, there are areas where a clear misfit is visible (e. g. Canton of Valais). This might be caused due to the boundary problems of the strain calculation and an unsatisfactory GNSS point density. In

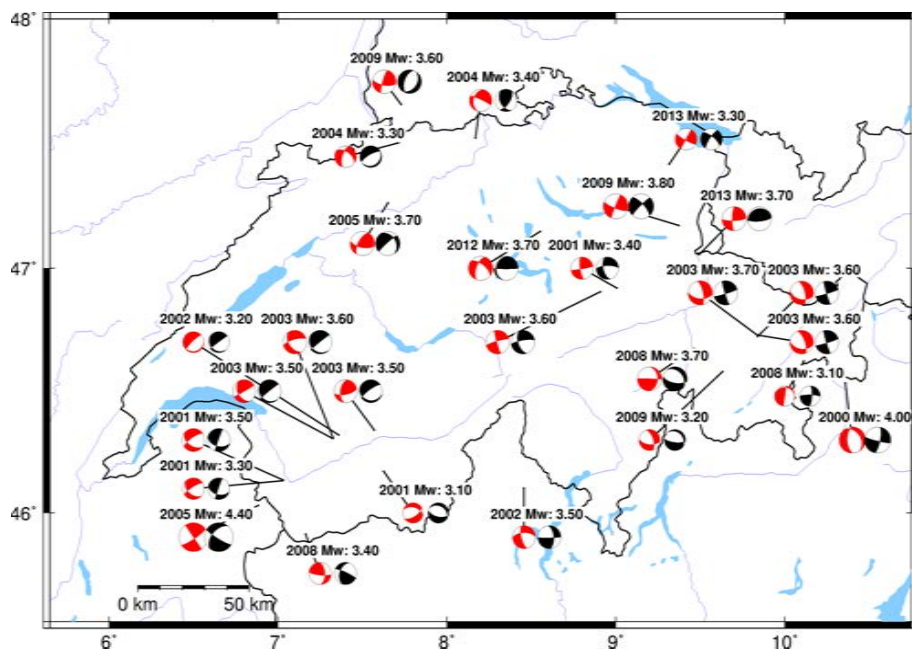


**Figure 6.12:** Beachball solution for earthquakes between 2004 and 2013 above Mw 3.4 from seismic recordings (obtained from the SED, black) and derived from the 3-D strain rate tensor (hypocentre, grey).

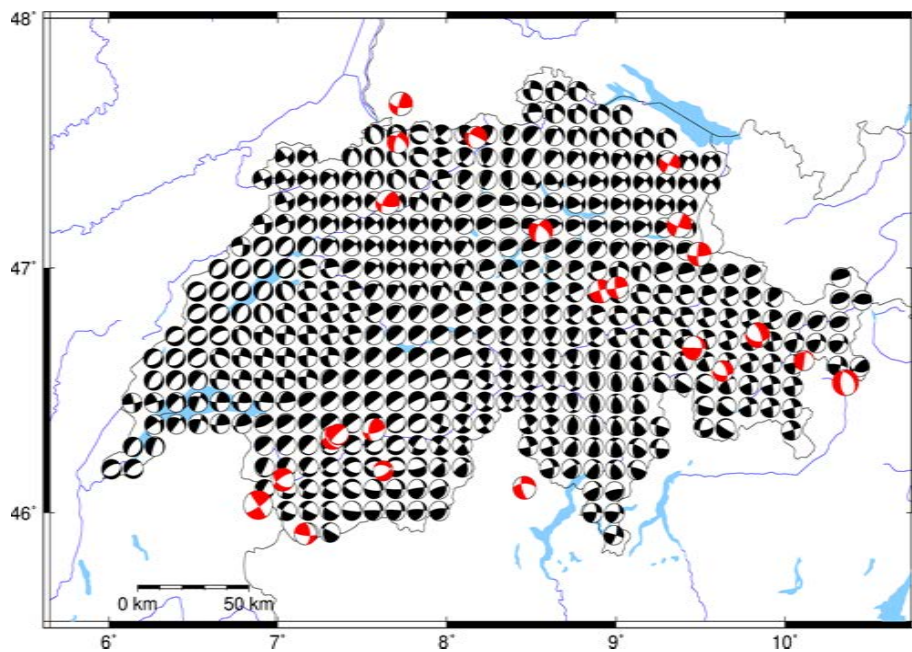


**Figure 6.13:** Earthquake solutions from seismic recordings (SED, red beachballs) overlaid onto the fault mechanism derived from geodetic solutions (epicentre).

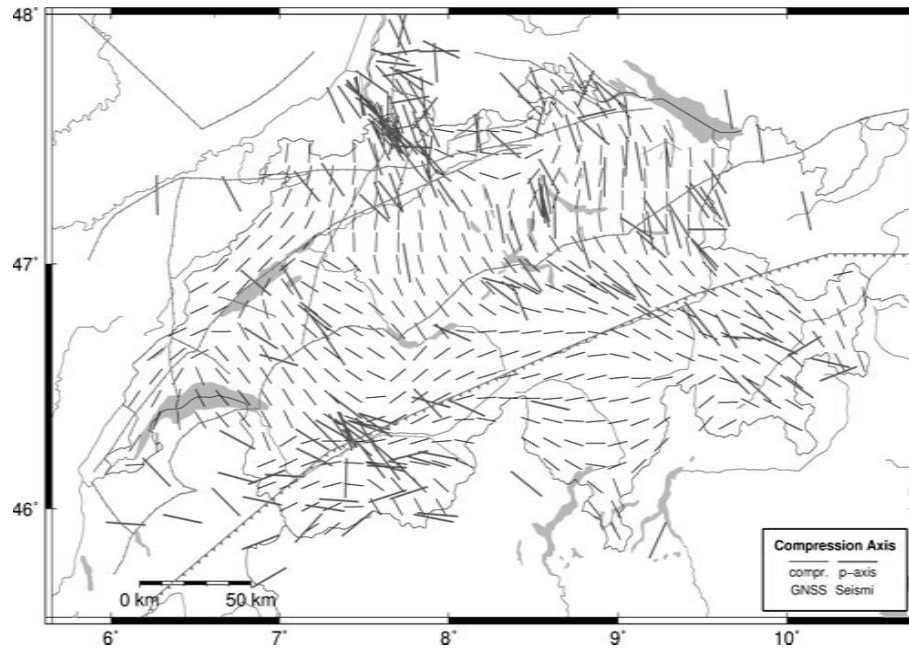


**Figure 6.14:** The short black lines indicate the direction of the main compression resulting from the strain rate tensor. The large red lines are the p-axes from known earthquakes in Switzerland taken from [Kastrup *et al.*, 2004] and [Marschall *et al.*, 2013].

order to investigate the governing geodynamic processes in more detail a permanent GNSS network for the area has been installed leading to a better coverage of the study area (see Chapter 7).

## 6.5 Comparison with world wide models

The world strain rate project [Kreemer *et al.*, 2000, 2003] delivers strain information over the whole world. However, the resolution is not as high as the CHTRF campaigns (which cover only a small area) and does not include strain rates for Switzerland. A comparison cannot be made.

The world stress map project [Heidbach *et al.*, 2008] contains information on the stress regimes and compression axis obtained by various methods. It includes data sets of the earthquake catalog for Switzerland which is displayed in Figure 6.16. The catalog includes most of the earthquakes analysed in Subsection 6.4.3 and leads to the same conclusion. The p-axis fits mostly with the geodetically obtained compression axis.

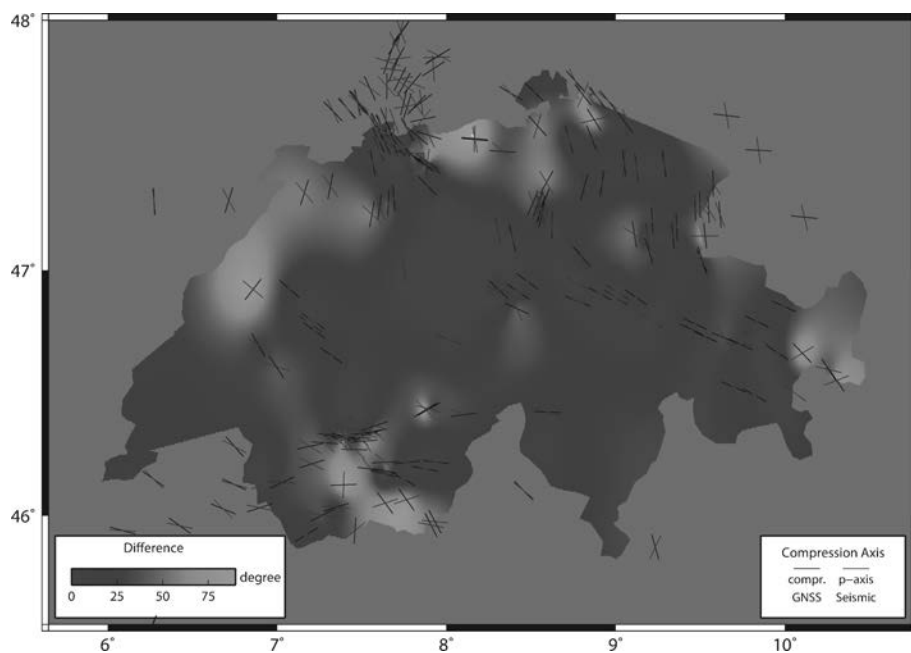


**Figure 6.15:** For each available earthquake the p-axis and their corresponding compression (from GNSS) are plotted. The background is the interpolated field of the angle between seismic and geodetic compression direction. The angle is between 0 and 90 degrees.

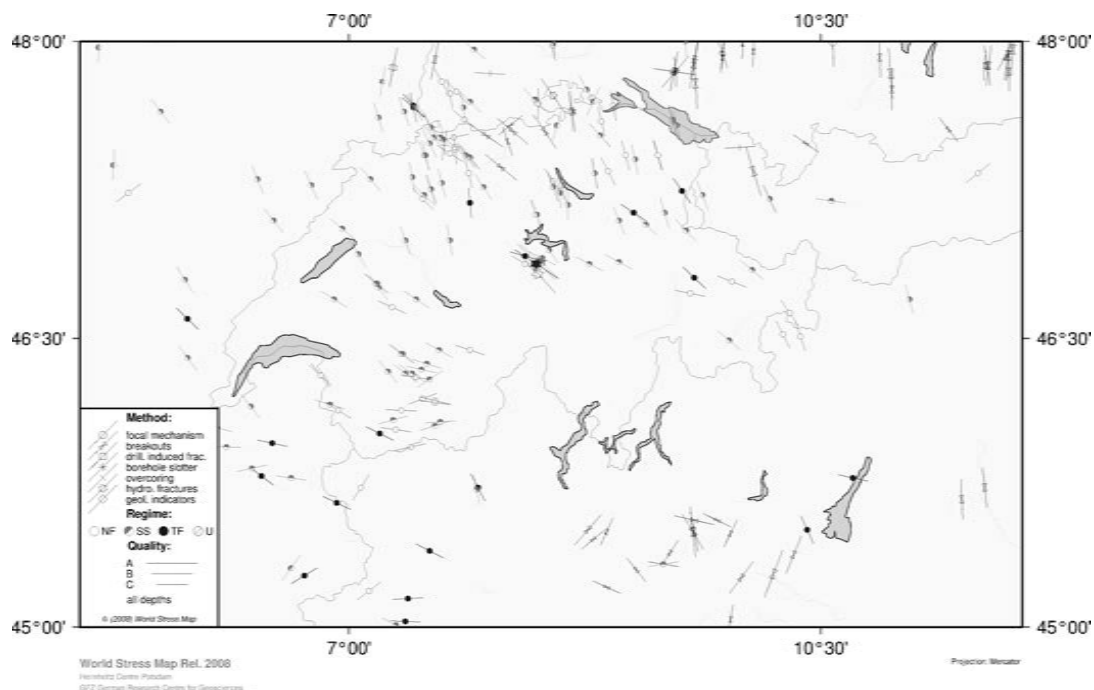


**Figure 6.16:** World stress map (WSM) database; Image created by the WSM project [Heidbach *et al.*, 2008]. NF=normal fault, SS=strike-slip, TF=thrust faulting, U=unknown.

# 7 Dense GNSS network for small scale tectonic analysis in the Canton of Valais

The densification of the GNSS network in the Canton of Valais led to the COGEAR network. It started in 2005 with the project Tectonic in the Valais (TECVAl) and then continued by the project Coupled Seismogenic Geohazards in Alpine Regions (COGEAR). This thesis focused, apart of the kinematic field extraction, also on the maintenance of the existing TECVAL network and its extension during the project COGEAR. This covered among others: replacement of malfunctioning equipment, modernisation of the data transfer, evaluation of possible GNSS site locations, acquisition of new GNSS equipment, and maintain the data transfer from the field to the file server.

## 7.1 Introduction

Switzerland is less at risk concerning seismic hazard compared to other regions. The regions with higher seismicity are located in Basel (Upper Rhinegraben) and in the Canton of Valais (with a maximum in the Wildstrubel area) [Giardini *et al.*, 2004]. Historical earthquakes from the past centuries reveal that several major earthquakes occurred in the latter region: 1755 (Brig), 1855 (Visp), and 1946 (Sierre). These three earthquakes had magnitudes above six according to the ECOS<sup>1</sup> database.

It is known from the GNSS campaigns (CHTRF) that the Canton of Valais has relatively high deformation rates (geodetic strain rates) compared to the rest of the country. The data show extension for this region with a maximum of 25 nano strain. However, the campaign data is not sufficiently dense in this region and, with a repeat period of six years, less accurate than data from permanent stations. The permanent network (AGNES), which is operated by swisstopo, covers the region with five stations: Martigny, Hohtenn, Jungfrauoch, Zermatt, and Sarnen. A deeper look at the situation from 2005 combined with the recorded earthquakes between 1975 and 2009 [Fäh *et al.*, 2011a] (Figure 7.1) reveals that the regions with most events was not covered properly.

---

<sup>1</sup>Earthquake Catalog of Switzerland 2009, <http://www.seismo.ethz.ch>, accessed 2013/06/16

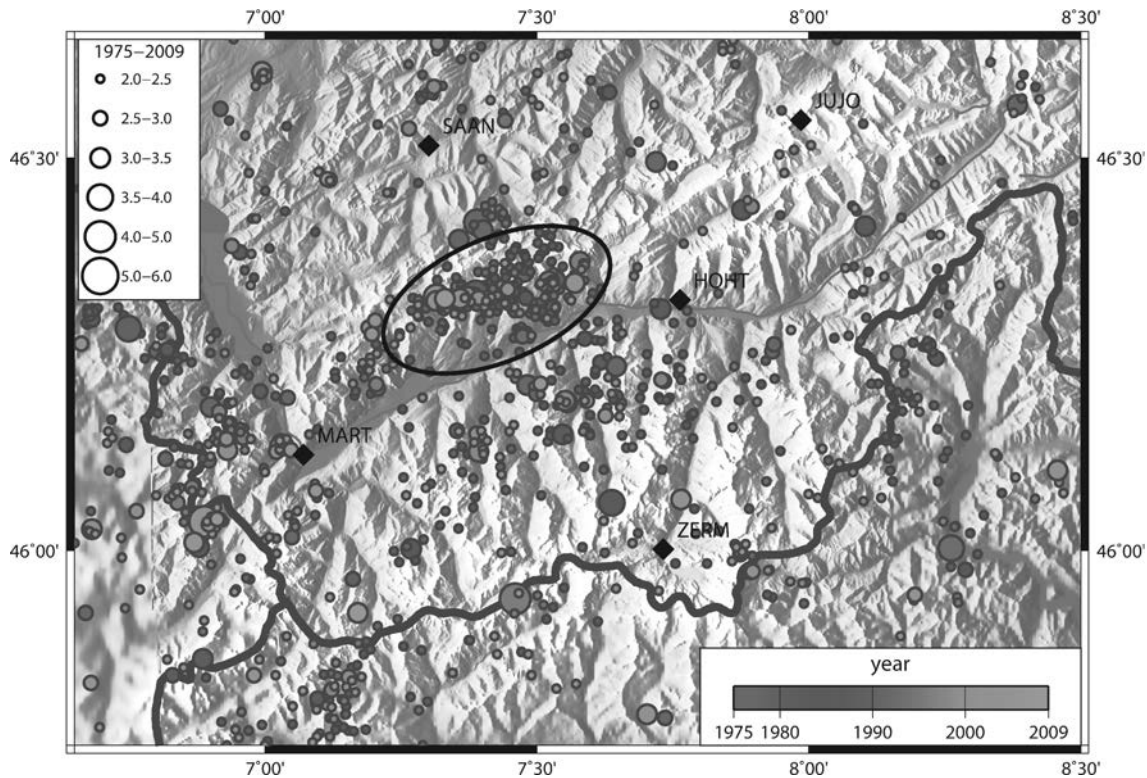


**Figure 7.1:** Earthquakes with a magnitude  $M_w > 2$  from 1975 to 2009 from the ECOS 2009 database. The Wildstrubel area is marked by the black ellipse and the AGNES sites as black diamonds.

### 7.1.1 Tectonic in the Valais (TECVAl)

The Wildstrubel area has a very high density of earthquakes as shown in Figure 7.1. The observation of the ongoing surface deformations using geodetic methods was not possible using the available GNSS sites before in 2005. The campaign data and the AGNES network do not cover the Wildstrubel area properly. Therefore, the project TECVAL was introduced to study the tectonic processes within the Wildstrubel area. It was decided to install five additional permanent GPS sites around the area.

The five new GPS stations were installed between 2005 and 2006. The locations are shown in Figure 7.2. The new setup surrounds the Wildstrubel area to detect the relative deformation within the observed region. The exact locations are listed below:

- ERDE: Located in the village Erde mounted on a savage plant building.
- CRDM: Located on the roof of the mountain station of the cable car connecting the mountain top with the town Vercorin.
- SANE: Located at the bottom of the Sanetsch dam mounted at the machine building.
- VARE: Located in the village Varen mounted on a savage plant building.

**Table 7.1:** TECVAL sites: History (SR=sampling rate and RB=ring buffer).

SITE	Height	Installation	Receiver	Antenna	SR	RB
CRDM	2332 m	2006/03/01	TRIMBLE NETRS	TRM41249.00	30s	-
		2012/08/26	TRIMBLE NETRS	TRM55971.00	30s	-
ERDE	782 m	2005/10/05	TRIMBLE NETRS	TRM41249.00	30s	-
		2011/12/08	TRIMBLE NETR9		30s	1s
SANE	2077m	2005/10/07	TRIMBLE NETRS	TRM41249.00	30s	-
VARE	703m	2005/10/07	TRIMBLE NETRS	TRM41249.00	30s	-
		2012/01/27	TRIMBLE NETR9		30s	1s
WEHO	2967m	2006/09/06	TRIMBLE NETRS	TRM41249.00	30s	-
		2009/03/03	TRIMBLE NETRS			

- WEHO: Located at the top of the Weisshorn mountain in the Canton of Valais (military building).

The station setup consists originally of a Trimble NETRS receiver and a Trimble Zephyr antenna. With time several receivers had technical problems and had to be replaced. CRDM and WEHO were replaced by other Trimble NETRS receivers. CRDM suffered also from a broken antenna which was replaced by a new Zephyr Geodetic 2 antenna. The initially installed receivers in ERDE and VARE broke in 2011; Trimble NETR9 receivers replaced the old ones. The current setups are listed in Table 7.1.

The setup of the TECVAL sites was initially planned to combine a Trimble NETRS receiver with an analogue modem to download data and maintain the sites remotely. However, from the five installed sites only three could be connected by a modem. The remaining two sites (CRDM and SANE) are only accessible on site because the installation of a internet connection was not possible; regular visits to the two sites are needed to collect the recorded data.

The sites have been mounted on existing buildings. The receivers are placed inside of the buildings where electricity and internet connection are available (apart from CRDM and SANE). Figure 7.3 displays the stations ERDE and CRDM. The final network was reached in 2006 with the installation of the Weisshorn site (WEHO) leading to the situation shown in Figure 7.2.

### 7.1.2 Coupled seismogenic geohazards in Alpine regions (COGEAR)

The project COGEAR [Fäh *et al.*, 2011b; Kretz *et al.*, 2011] focuses on the area around Visp and the Matternal. Various disciplines took part in this study applying their methods and research focusing on the given area. The main goal was to understand the ongoing processes and connecting the various researchers to work on the same spot. The geodetic part covers the observation of surface deformations with permanent sites. Placing the

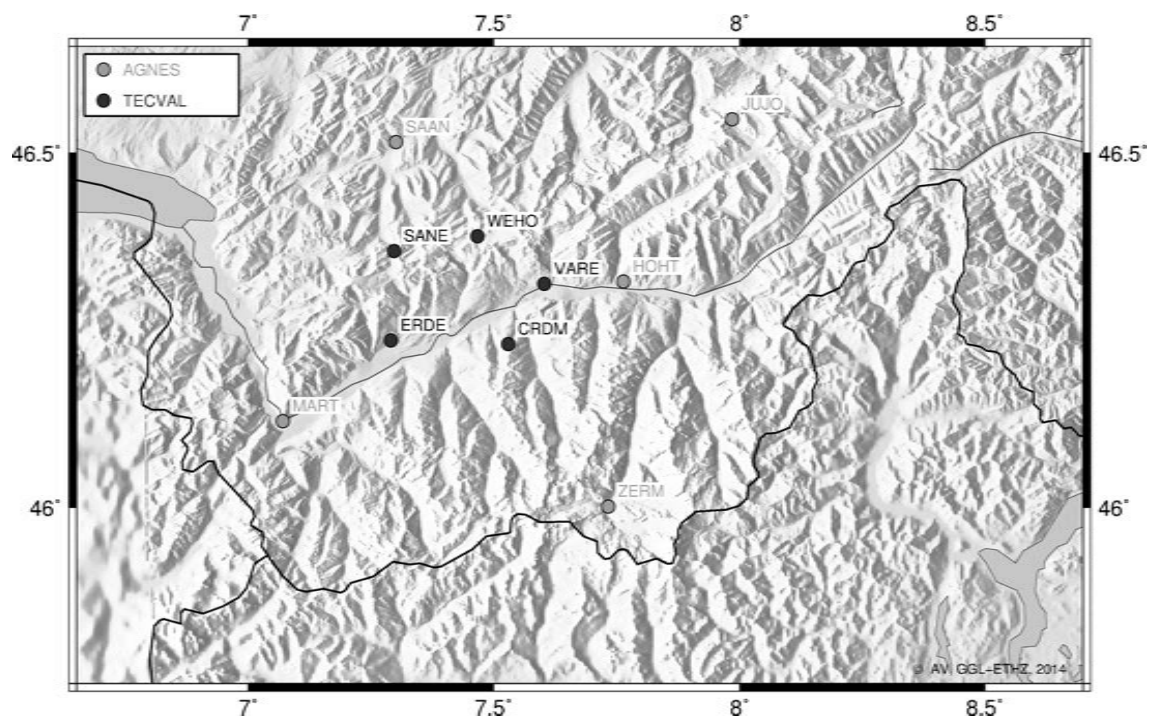
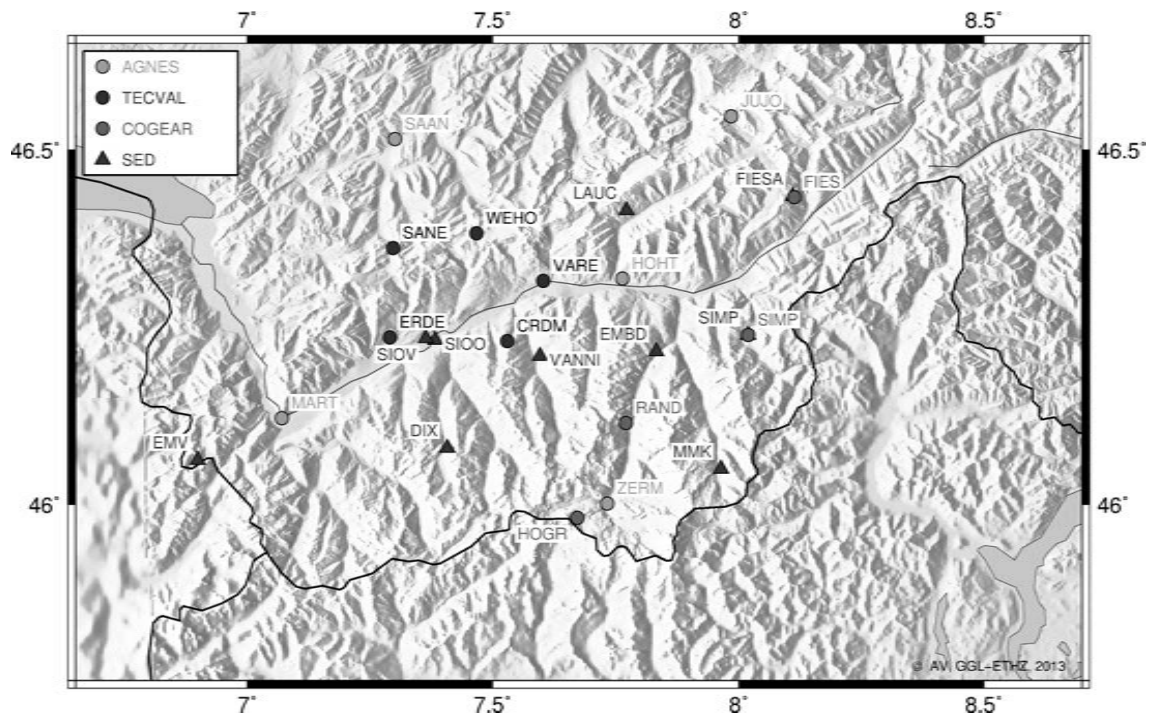


Figure 7.2: Situation in 2006: AGNES and TECVAL sites



Figure 7.3: Station ERDE (left) and CRDM (right).



**Figure 7.4:** Location of seismic (SED) and geodetic instruments.

permanent GNSS sites next to seismic instruments was an important aspect, whenever possible, to co-locate both measurement methods in case of an earthquake. The seismic sites are operated by the Swiss Seismological Service (SED).

The reconnaissance of possible seismic stations for GNSS locations was difficult and finally led to two additional combined sites (FIES and RAND), one site of the TECVAL network is also co-located (SANE). The major reason for not co-locating all new sites is the location of the existing seismic sites. Figure 7.4 shows our installed GNSS network and the analysed seismometer locations; the complete seismic network can be accessed on the SED web page<sup>2</sup>. Several sites have been visited to determine their suitability for the co-location. Most locations have no open sky to track the satellites; some sites are located in the forest, some sites are located in places with high obstacles (e.g. valley located southwards with an open view to the north), or just located near existing GPS sites; in this case the areal distribution was higher weighted than the co-location. The seismometer FIES (Fiescheralp) is located in a tunnel. The GNSS antenna was placed above the tunnel. The antenna of the co-located site in Simplon is installed on top of the bunker where the seismometer is placed. The currently installed sites (August 2013) are shown in Figure 7.4 and listed in Table 7.2. The installations of the stations SIMP and RAND are shown in Figure 7.5.

The installations of the COGEAR sites consist of a Leica GRX1200+ receivers and an AR25 choke ring antenna. The Leica receivers support to measure the GNSS signals with

<sup>2</sup><http://www.seismo.ethz.ch>, accessed 2013/08/08



**Figure 7.5:** Station SIMP (left) and RAND (right).

**Table 7.2:** COGEAR Sites: History (SR=sampling rate and RB=ring buffer).

SITE	Height	Installation	Receiver	Antenna		SR	RB
FIES	2335 m	2011/11/11	LEICA GRX1200+GNSS	LEIAR25.R3	LEIT	30s	20 Hz
HOGR	3463 m	2011/02/02	LEICA GRX1200+GNSS	LEIAR10	NONE	30s	20 Hz
RAND	2407 m	2011/05/25	LEICA GRX1200+GNSS	LEIAR25.R3	LEIT	30s	20 Hz
SIMP	1952 m	2011/06/24	LEICA GRX1200+GNSS	LEIAR25.R3	LEIT	30s	20 Hz

up to 20 Hz. For the long-term aspects a data logging of 30-seconds is enough. Therefore, the 30 second measurements are stored and sent to the processing center. Additionally, a ring buffer has been installed for all Leica receivers storing the 20 Hz data locally. The data can be accessed if an earthquake occurs to analyse the recorded signals and to compare them with the seismometer data.

## 7.2 GNSS network

The GNSS network shown in Figure 7.4 is maintained and processed by the GGL<sup>3</sup>. The processing is done using the Bernese GNSS Software 5.2 [Dach *et al.*, 2007] with HOHT as a fixed reference. The time series shown in Figures 7.6, 7.7, and 7.8 were processed by Dr. Ph. Limpach at GGL (ETH Zürich).

Additionally source sites are included into the nation wide processing of swisstopo<sup>4</sup>. The sites ERDE, VARE, WEHO, HOGR, RAND, and SIMP are transferred from GGL to swisstopo and included into its AGNES processing. The stations CRDM and SANE are not included due to the lack of an internet connection; the daily download is not possible.

<sup>3</sup><http://www.ggl.baug.ethz.ch/research/cogear>, accessed 2014/01/14

<sup>4</sup><http://www.swisstopo.admin.ch/internet/swisstopo/de/home/topics/survey/permet/pnac/series.html>, accessed 2014/01/14

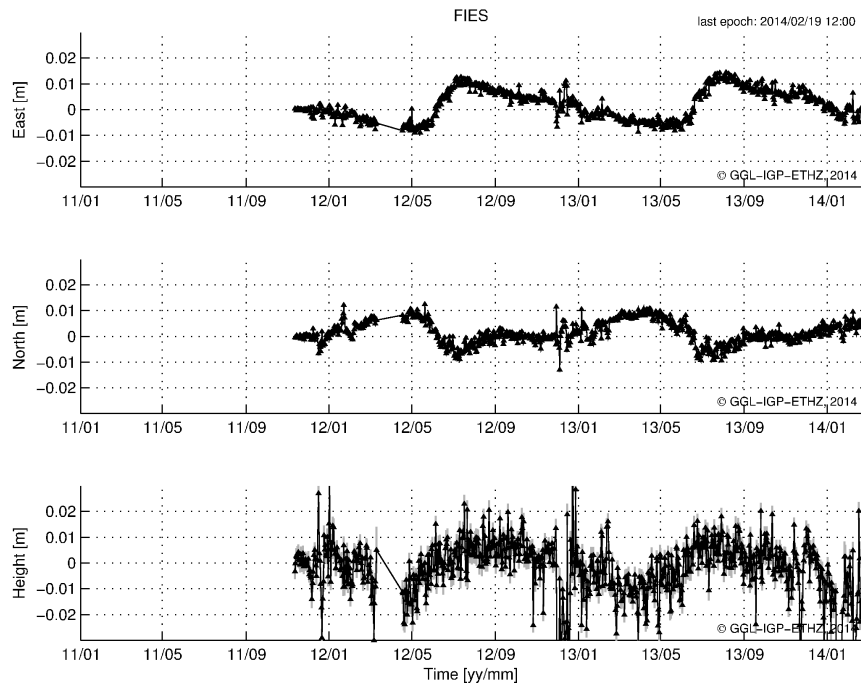


Figure 7.6: Coordinate time series: FIES. The blue line represents the accuracy ( $3\text{-}\sigma$ ).

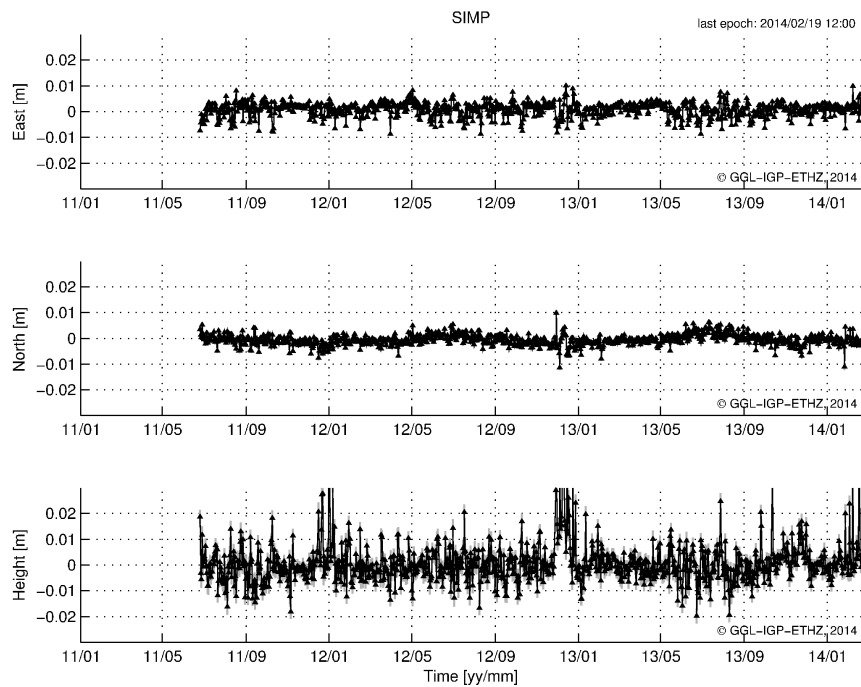
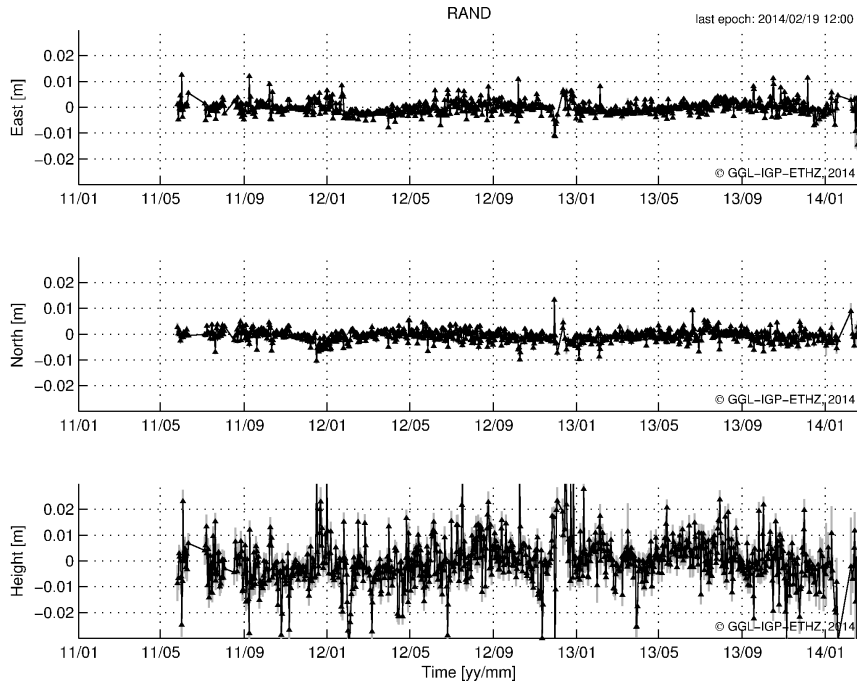
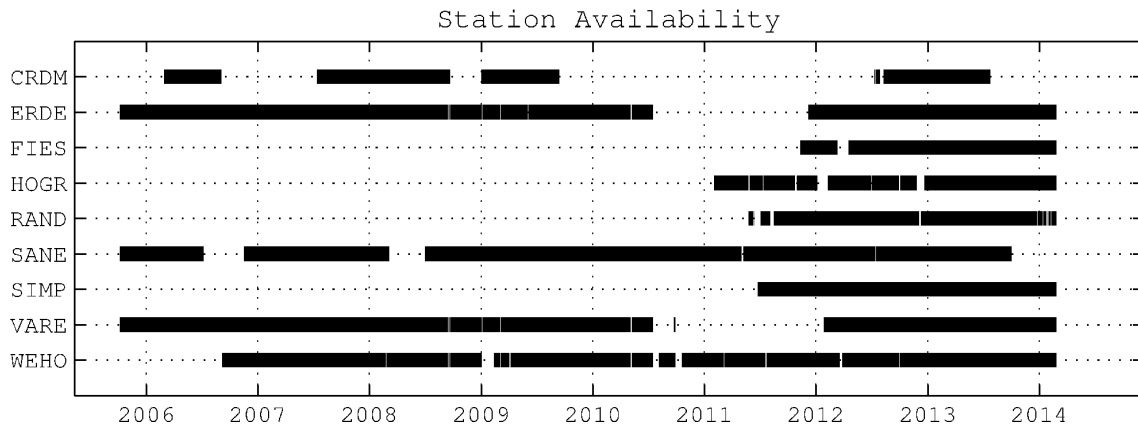


Figure 7.7: Coordinate time series: SIMP. The blue line represents the accuracy ( $3\text{-}\sigma$ ).



**Figure 7.8:** Coordinate time series: RAND. The blue line represents the accuracy ( $3\sigma$ ).

The data time series have discontinuities due to technical issues such as hardware failure. Figure 7.9 lists all GGL sites and their available data (snapshot from 2014/01/14). The sites still need to run for a few years before their velocities are accurate enough for geodynamic interpretations; the expected velocities are below 1 millimetre per year.



**Figure 7.9:** Station availability (2014/02/26).

## 8 Conclusion and outlook

Switzerland is a region with moderate seismicity compared to other continent-continent collision zones. Only from historic earthquakes it is known that events with large magnitudes, above six, have occurred. As deduced from GNSS campaign data the present deformation rates amount to 25 nano strains per year. The major challenge was to extract the tectonically driven velocity field based on GNSS campaign type data (CHTRF 2010 solution) given the fact that the noise level and local influences are of the same order of magnitude as the tectonic deformations. Relative to the reference station Zimmerwald, the velocity field shows the following characteristics:

- The horizontal velocities are between zero and one mm/yr.
- The western part of the Swiss Molasse Basin is moving towards South-West (0.3 mm/yr).
- The southern part of Canton of Graubünden is moving westward (0.5 mm/yr).
- The southern region of the Rhone valley is moving towards South-West (1 mm/yr).
- The uplift rates are zero mm/yr for the Swiss Molasse Basin and increasing to 1.5 mm/yr in the Swiss Alps with peaks in the Cantons of Valais and Graubünden.

The analysis of the time series from the permanent Swiss GNSS network AGNES did not reveal any major correlation between the stations nor a common mode effect. These findings were subsequently used for the processing of the campaign results: no correlation between the measurements had to be introduced to the collocation.

The analysis of the permanent network data revealed that the area can be divided into six rigid blocks. The blocks of the Swiss Molasse Basin and the Alpine region are in state of compression. The major challenge was to define the block boundaries. To avoid the necessity to define rigid blocks, the ALSC approach has been applied successfully in order to map the tectonic pattern based on the measurements themselves.

The improved ALSC approach was able to extract the tectonic deformation from the CHTRF 2010 solution combined with precise levelling data for the vertical component. The output of the collocation reveals similar patterns as these obtained from seismic recordings. The extensional stress regimes in the Cantons of Valais and Graubünden could be reproduced by the collocation technique leading to extensional strain rates of 20 nstrain/yr. Compression in the Swiss Molasse Basin perpendicular to the Alpine chain is detected in both methods. The geodetically obtained compression rates are between 5 and 15 nanos-

train/yr. The deformation field was extracted based on measurements performed on the surface alone. The standard deviations of the velocities are mostly below the value of 0.2 mm/yr. The extracted strain rates, between -25 and 25 nanostrain, are statistically significant. The standard deviations for the strain rates amounts up to 5 nanostrain ( $1-\sigma$ ).

It was possible to extract a fully populated 3-D strain tensor by introducing the bending of a thin plate. This offered the possibility to estimate the upward component of deformation. Even though the assumptions are basic it leads to reasonable results. The comparison between the calculated strain rate tensor and the earthquake fault plane solutions shows good agreement.

The annually accumulated strain energy density is an indicator for strain accumulation which, in turn, can be released in earthquakes. Areas are revealed where, during the time span (about 20 years) covered, the accumulated strain rate energy shows a maximum. They are located in the Cantons of Valais and Graubünden with a strain energy up to 3.8 GJ/km<sup>2</sup>. The strain energy calculations have shown good agreement with energy calculation based on historical and recent earthquakes. Both introduced models, zero and non-zero vertical strain, lead to reasonable results. However, the thin plate model is to be favored since it also maps the vertical strain component.

There are areas where the geodetically determined deformations do not match with the seismological information. This holds true, in particular for the region around the city of Basel, where no geodetic deformation has been found. This is likely to be caused by missing measuring points north of the Swiss boundary.

The Canton of Valais is the seismically most active region within Switzerland. The GNSS-derived deformation energy density reflect very well the seismic hazard as derived from earthquake studies. However, there are still some disagreements, especially when looking at the compression axis of the earthquakes and strain tensor. This has to be further addressed. To this end the COGEAR network has been installed in order to enhance the coverage of the seismogenic region in the Valais by continuous GNSS data.

The strain rate field derived from GNSS campaigns leads to a realistic solution of the ongoing tectonic processes. It is shown, that using a simple thin plate model, it is possible to extract the governing strain regime and to predict possible movements along faults.

During the project several achievements have been made. Nevertheless, for the future there is more work to be done. The additional GNSS campaign of 2010 has brought a major improvement in the velocity estimation. A future campaign (2016) will provide additional stability to the processing leading to an even more reliable velocity estimation. This may reduce regional effects as in case of the westward movements in the North-Eastern part of Switzerland which was no longer seen in the data of the latest campaign.

The downward continuation of the strain field is still a major task. The thin plate model delivered good results for a first approximation. However, it still relies on surface data alone. To improve this deficiency additional information in the crust, such as earthquake

---

focal mechanisms or borehole data, should be included into the analysis. Also, a more sophisticated modeling of the crust, such as finite element modeling might lead to a better understanding of the processes going on.

In the Canton of Valais, an extension of the measuring time is needed to improve the knowledge of tectonic deformation. This holds true in general for all of the long-term deformation measurements. Thus, the recently installed network COGEAR will deliver additional strain information in the Valais within the next years. Today, the covered time span is too short to make more reliable velocity estimations. Three sites have been closely co-located with seismic stations. With the installed 20 Hz ring buffer the network will also be useful for the assessment of hazard of future major earthquakes.



# Bibliography

- Alber, C., R. Ware, C. Rocken, and J. Braun (2000), Obtaining single path phase delays from GPS double differences, *Geophys. Res. Lett.*, *27*, 2661–2664.
- Argus, D. F., and R. G. Gordon (1991), No-net-rotation model of current plate velocities incorporating plate motion model NUVEL-1, *Geophys. Res. Lett.*, *18*, 2039–2042, doi: 10.1029/91GL01532.
- Baarda, W. (1968), A testing procedure for use in geodetic networks, *Neth Geod. Comm.*, *2*(5).
- Battaglia, M., M. H. Murray, E. Serpelloni, and R. Bürgmann (2004), The Adriatic region: An independent microplate within the Africa-Eurasia collision zone, *Geophys. Res. Lett.*, *31*, L09605, doi:1029/2004GL019723.
- Bauchau, O., and J. Craig (2009), *Structural Analysis, Solid Mechanics and Its Applications*, vol. 163, chap. Kirchhoff plate theory, pp. 819–914, Springer Netherland, doi: 10.1007/978-90-481-2516-6\_16, isbn: 978-90-481-2515-9.
- Baumann, M. (1994), Three-dimensional modeling of the crust-mantle boundary in the alpine region, Ph.D. thesis, ETH Zurich, nr. 10772.
- Blewitt, G., and D. Lavallée (2002), Effect of annual signals on geodetic velocity, *J. Geophys. Res.*, *107*(B7), 2145, doi:10.1029/2001JB000570.
- Brockmann, E., and A. Schlatter (2011), 20 years of maintaining the Swiss terrestrial reference frame CHTRF, in *Subcommission for the European Reference Frame (EUREF), Chisinau, May 25–28*.
- Brockmann, E., S. Grünig, R. Hug, D. Schneider, A. Wiget, and U. Wild (2002a), Applications of the real-time Swiss permanent GPS network 'AGNES', in *Proceedings of the EGS conference, Nice*.
- Brockmann, E., R. Hug, and T. Signer (2002b), Geotectonics in the Swiss Alps using GPS, in *Subcommission for the European Reference Frame (EUREF)*, vol. 11, edited by J. Torres and H. Hornik, EUREF Publication.
- Brockmann, E., S. Grünig, D. Ineichen, and S. Schär (2006), Monitoring the Automated GPS Network of Switzerland AGNES, in *Subcommission for the European Reference Frame (EUREF)*, edited by J. Torres and H. Hornik.

- Brockmann, E., D. Ineichen, U. Marti, U. Schär, A. Schlatter, and A. Villiger (2012), Determination of Tectonic Movements in the Swiss Alps using GNSS and Levelling, in *Geodesy for Planet Earth, International Association of Geodesy Symposia*, vol. 136, edited by S. Kenyon, M. C. Pacino, and U. Marti, pp. 689–695, Springer Berlin Heidelberg.
- Brockmann, E., D. Ineichen, U. Marti, S. Schär, and A. Schlatter (2013), Determination of the Swiss Alpine Uplift using GNSS and Levelling, in *International Association of Geodesy Scientific Assembly 2013*.
- Calais, E., J. M. Nocquet, F. Jouanne, and M. Tardy (2002), Current strain regime in the western Alps from continuous global positioning system measurements, 1996–2001, *Geology*, *30*, 651–654, doi:10.1130/0091-7613(2002)030<0651:CSRITW>2.0.CO;2.
- Cardozo, N., and R. Allmendinger (2009), SSPX: A program to compute strain from displacement/velocity data, *Comp. Geosci.*, *35*(6), 1343–1357, doi: 10.1016/j.cageo.2008.05.008.
- Chen, Q., J. T. Freymueller, Q. Wang, Z. Yang, C. Xu, and J. Liu (2004), A deforming block model for the present-day tectonics of Tibet, *J. Geophys. Res.*, *109*, B01403, doi: 10.1029/2002JB002151.
- Dach, R., U. Hugentobler, P. Fridez, and M. Meindl (2007), Bernese GPS software version 5.0, *Astronomical Institute, University of Bern*.
- Danuser, G., A. Geiger, and M. V. Müller (1993), Modellierung von Verschiebungs- und Verzerrungsfeldern, *Bericht 218*, ETH Zurich, Institute of Geodesy and Photogrammetry.
- Egli, R. (2004), Swiss-4D: Geodynamik in der Schweiz, *Tech. rep.*, swisstopo.
- Egli, R., A. Geiger, A. Wiget, and H.-G. Kahle (2007), A modified least-squares collocation method for the determination of crustal deformation: first results in the Swiss Alps, *Geophys. J. Int.*, *168*(1), 1–12, doi:10.1111/j.1365-246X.2006.03138.x.
- Elmiger, A., R. Köchle, A. Ryf, and F. Chaperon (1995), *Geodätische Alpen traverse Gotthard, Geodätisch-geophysikalische Arbeiten in der Schweiz*, vol. 50, Swiss Geodetic Commission.
- Fäh, D., D. Giardini, P. Kästli, N. Deichmann, M. Gisler, G. Schwarz-Zanetti, S. Alvarez-Rubio, S. Sellami, B. Edwards, B. Allmann, F. Bethmann, J. Wössner, G. Gassner-Stamm, S. Fritsche, and D. Eberhard (2011a), ECOS-09 Earthquake Catalogue of Switzerland Release 2011. Report and Database. Public catalogue, Report SED/RISK/R/001/20110417.
- Fäh, D., J. Moore, J. Burjanek, I. Iosifescu, L. Dalguer, F. Dupray, C. Michel, J. Woessner, A. Villiger, J. Laue, I. Marschall, V. Gischig, S. Löw, S. Alvarez, W. Balderer, P. Kästli,

- D. Giardini, C. Iosifescu, L. Hurni, P. Lestuzzi, A. Karbassi, C. Baumann, A. Geiger, A. Ferrari, L. Lalou, J. Clinton, and N. Deichmann (2011b), Coupled seismogenic geohazards in alpine regions, *Bollettino di geofisica teorica ed applicata*.
- Federal Department of Environment, Transport, Energy and Communications (Ed.) (2006), *Earthquakes in Switzerland - the greatest natural hazard*.
- Frisch, W., M. Meschede, and R. Blakey (2011), *Plate tectonics: Continental Drift and Mountain Building*, Springer Berlin Heidelberg, doi:10.1007/978-3-540-76504-2, isbn: 978-3-540-76504-2.
- Geiger, A., H.-G. Kahle, and E. Gubler (1986), Recent crustal movements in the Alpine-Mediterranean region analyzed in the Swiss Alps, *Tectonophysics*, 130, 289–298, doi: 10.1016/0040-1951(86)90119-8, 1st International Symposium on Recent Crustal Movements in Central and South America.
- Giardini, D., S. Wiemer, D. Fäh, and N. Deichmann (2004), *Seismic Hazard Assessment of Switzerland, 2004*, Swiss Seismological Service, ETH Zürich.
- Gubler, E., H.-G. Kahle, E. Kingele, S. Mueller, and R. Olivier (1981), Recent crustal movements in Switzerland and their geophysical interpretation, *Tectonophysics*, 71, 125–152, doi:10.1016/0040-1951(81)90054-8.
- Heidbach, O., and H. Drewes (2003), 3D finite element model of major tectonic processes in the Eastern Mediterranean, *Geological Society*, doi:10.1144/GSL.SP.2003.212.01.17.
- Heidbach, O., M. Tingay, A. Barth, J. Reinecker, D. Kurfes, and B. Müller (2008), The World Stress Map database release 2008, doi:10.1594/GFZ.WSM.Rel2008.
- Hinderer, M. (2001), Late Quaternary denudation of the Alps, valley and lake fillings and modern river loads, *Geodinamica Acta*, 14(4), 231–263, doi:10.1016/S0985-3111(01)01070-1.
- Hollenstein, Ch. (2007), *GPS Deformation Field and Geodynamic Implications for the Hellenic Plate Boundary Region*, vol. 93, Institute of Geodesy and Photogrammetry, ETH Zurich, isbn: 3-906467-64-3.
- Kahle, H.-G., M. V. Müller, A. Geiger, G. Danuser, S. Müller, G. Veis, H. Billiris, and D. Paradissis (1995), The strain field in northwestern Greece and the Ionian Islands: results inferred from GPS measurements, *Tectonophysics*, 249, 41–52, doi:10.1016/0040-1951(95)00042-L.
- Kastrup, U. (2002), Seismotectonics and stress field variations in Switzerland, Ph.D. thesis, ETH Zurich, doi:10.3929/ethz-a-004423062.
- Kastrup, U., M. L. Zoback, N. Deichmann, K. F. Evans, D. Giardini, and A. J. Michael (2004), Stress field variations in the Swiss Alps and the northern Alpine foreland derived from inversion of fault plane solutions, *J. Geophys. Res.*, 109, B01402, doi: 10.1029/2003JB002550.

- Kastrup, U., N. Deichmann, A. Fröhlich, and D. Giardini (2007), Evidence for an active fault below the northwestern Alpine foreland of Switzerland, *Geophys. J. Int.*, *169*(3), 1273–1288.
- Kreemer, C., A. Haines, W. Holt, G. Blewitt, and D. Lavalée (2000), On the determination of a global strain rate model, *Earth Planets Space*, *52*, 765–770.
- Kreemer, C., W. E. Holt, and A. J. Haines (2003), An integrated global model of present-day plate motions and plate boundary deformation, *Geophys. J. Int.*, *154*, 8–34, doi:10.1046/j.1365-246X.2003.01917.x.
- Kretz, A., A. Villiger, P. Limpach, and A. Geiger (2011), GNSS Instrumentation in the Valais: Monitoring System and Documentation, *Project cogear. final report 2011 (del. no.: 2b.1.2)*, ETH Zurich.
- Labhart, T. P. (2009), *Geologie der Schweiz*, 8. Auflage ed., Ott Verlag, isbn: 978-3-7225-0116-1.
- Leddra, M. (2010), *Time Matters: Geology's Legacy to Scientific Thought*, John Wiley & Sons, Ltd, doi:10.1002/9781444323252, isbn: 978-1-4051-9908-7.
- Marschall, I., N. Deichmann, and F. Marone (2013), Earthquake focal mechanisms and stress orientations in the eastern Swiss Alps, *Swiss J Geosci*, *106*, 79–90, doi:0.1007/s00015-013-0129-5.
- Maurer, H. R., M. Burkhard, N. Deichmann, and A. G. Green (1997), Active tectonism in the central Alps: contrasting stress regimes north and south of the Rhone Valley, *Terra Nova*, *9*(2), 91–94, doi:10.1111/j.1365-3121.1997.tb00010.x.
- McClusky, S., S. Bjornstad, B. Hager, R. W. King, B. Maede, M. Miller, F. Monastero, and B. Souter (2001), Present day kinematics of the Eastern California Shear Zone from a geodetically constrained block model, *Geophys. Res. Lett.*, *28*(17), 3369–3372, doi:10.1029/2001GL013091.
- Moritz, H. (1970), Least-Squares Estimation in Physical Geodesy, *Deutsche Geodätische Kommission, Reihe A: Höhere Geodäsie*, *69*, 1–34.
- Moritz, H. (1973), Least-Squares Collocation, *Deutsche Geodätische Kommission, Reihe A: Theoretische Geodäsie*, *75*, 1–91.
- Morrison, F. (1977), Azimuth-dependent statistics for interpolating geodetic data, *J. Geod.*, *51*, 105–118, doi:10.1007/BF02522280.
- Müller, M., A. Geiger, H.-G. Kahle, G. Veis, H. Billiris, D. Paradissis, and S. Felekis (2013), Velocity and deformation fields in the North Aegean domain, Greece, and implications for fault kinematics, derived from GPS data 1993–2009, *Tectonophysics*, *597–598*, 34–49, doi:10.1016/j.tecto.2012.08.003.

- 
- Nocquet, J.-M., and E. Calais (2004), Geodetic Measurements of Crustal Deformation in the Western Mediterranean and Europe, *Pure appl. Geophys.*, *161*(3), 661–681.
- Perler, D., A. Geiger, and F. Hurter (2011), 4D GPS water vapor tomography: new parameterized approaches, *J. Geod.*, *85*, 539–550, doi:10.1007/s00190-011-0454-2.
- Peter, Y. (2000), Present-day crustal dynamics in the Adriatic-Aegean plate boundary zone inferred from continuous GPS-measurements, Ph.D. thesis, ETH Zürich.
- Pfiffner, A., P. Lehner, P. Heitzmann, S. Mueller, and A. Steck (Eds.) (1997), *Deep structure of the Swiss Alps: results of NRP 20*, 460 pp., Birkhauser Verlag, Basel, Switzerland, isbn: 3-7643 5254 X.
- Pfiffner, A., S. Ellis, and C. Beaumont (2000), Collision tectonics in the Swiss Alps: Insight from geodynamic modeling, *Tectonics*, *19*(6), 1065–1094.
- R Development Core Team (2009), *R: A Language and Environment for Statistical Computing*, R Foundation for Statistical Computing, Vienna, Austria, isbn: 3-900051-07-0.
- Reilly, W. I., and E. Gubler (1990), Crustal strain in Switzerland 1870–1970, *Geophys. J. Int.*, *103*(1), 251–256, doi:10.1111/j.1365-246X.1990.tb01766.x.
- Rummel, R., and K. P. Schwarz (1977), On the nonhomogeneity of the global covariance function, *J. Geod.*, *51*(2), doi:10.1007/BF02522279.
- Rüttener, E. (1995), *Earthquake hazard evaluation for Switzerland, Matériaux pour la Géologie de la Suisse, Géophysique No 29 publié par la Commission Suisse de Géophysique*, vol. 29, Schweizerischer Erdbebendienst.
- Schlatter, A. (2005), *Das neue Landeshöhennetz der Schweiz LHN95, Geodätisch-geophysikalische Arbeiten in der Schweiz*, vol. 72, Swiss Geodetic Commission.
- Schmid, S. M., and N. Froitzheim (1993), Oblique slip and block rotation along the Engadine line, *Eclogae geol. Helv.*, *86*/2, 569–593.
- Schmid, S. M., and E. Kissling (2000), The arc of the western Alps in the light of geophysical data on deep crustal structure, *Tectonics*, *19*, 62–85.
- Stein, S., and M. Wysession (2003), *An Introduction to Seismology, Earthquakes, and Earth Structure*, Blackwell Publishing, isbn: 0-86542-078-5.
- Straub, C., and H.-G. Kahle (1994), Global Positioning System (GPS) estimates of crustal deformation in the Marmara Sea region, Northwestern Anatolia, *Earth Planet. Sci. Lett.*, *121*, 495–502, doi:10.1016/0012-821X(94)90086-8.
- Troller, M., A. Geiger, E. Brockmann, J.-M. Bettens, B. Bürki, and H.-G. Kahle (2006), Tomographic determination of the spatial distribution of water vapor using GPS observations, *Adv. Space Res.*, *37*(12), 2211–2217, doi:10.1016/j.asr.2005.07.002.

- van Dam, T., J. Wahr, P. C. D. Milly, A. B. Shmakin, G. Blewitt, D. Lavallée, and K. M. Larson (2001), Crustal displacements due to continental water loading, *Geophys. Res. Lett.*, 28(4), 651–654.
- van der Marel, H., and B. Gündlich (2006), Development of models for use of slant delays slant delay retrieval and multipath mapping software, *Tech. rep.*, Delft University of Technology, Department of Earth Observation and Space Systems (DEOS), Report for WP6100 TOUGH 1 Deliverable D33.
- Vose, M. D. (1999), *The simple genetic algorithm*, vol. 12, The MIT Press, isbn: 0-262-22058-X.
- Waldhauser, F., E. Kissling, J. Ansorge, and S. Mueller (1998), Three-dimensional interface modelling with two-dimensional seismic data: the Alpine crust-mantle boundary, *Geophys. J. Int.*, 135(1), 264–278, doi:10.1046/j.1365-246X.1998.00647.x.
- Wdowinski, S., Y. Bock, J. Zhang, and P. Fang (1997), Southern California Permanent GPS geodetic array: Spatial filtering of daily positions for estimating coseismic and postseismic displacements induced by the 1992 Landers earthquake, *J. Geophys. Res.*, 102, 18 057–18 070.
- Wegener, A. (1912), Die Entstehung der Kontinente, *Geologische Rundschau*, 3(4), 276–292, doi:10.1007/BF02202896.
- Weissert, H., and I. Stössel (2009), *Der Ozean im Gebirge*, vdf Hochschulverlag AG an der ETH Zürich, isbn: 978-3-7281-3221-5.
- Wessel, P., and W. H. F. Smith (1998), New, improved version of Generic Mapping Tools released, *EOS Trans. Amer. Geophys. U.*, 79 (47), 579.
- Wiget, A., U. Marti, R. Egli, A. Geiger, and O. Heller (2007), Deformation of the Swiss Geodetic Reference Network: Project Swiss4D, International Union of Geodesy and Geophysics (IUGG), Perugia, Italy.
- Zhang, J., Y. Bock, H. Johnson, P. Fang, S. Williams, J. Genrich, S. Wdowinski, and J. Behr (1997), Southern California Permanent GPS Geodetic Array: Error analysis of daily position estimates and site velocities, *J. Geophys. Res.*, 102(B8), 18 038–18 055, doi:10.1029/97JB01380.

# A Data analysis

## A.1 Common mode results

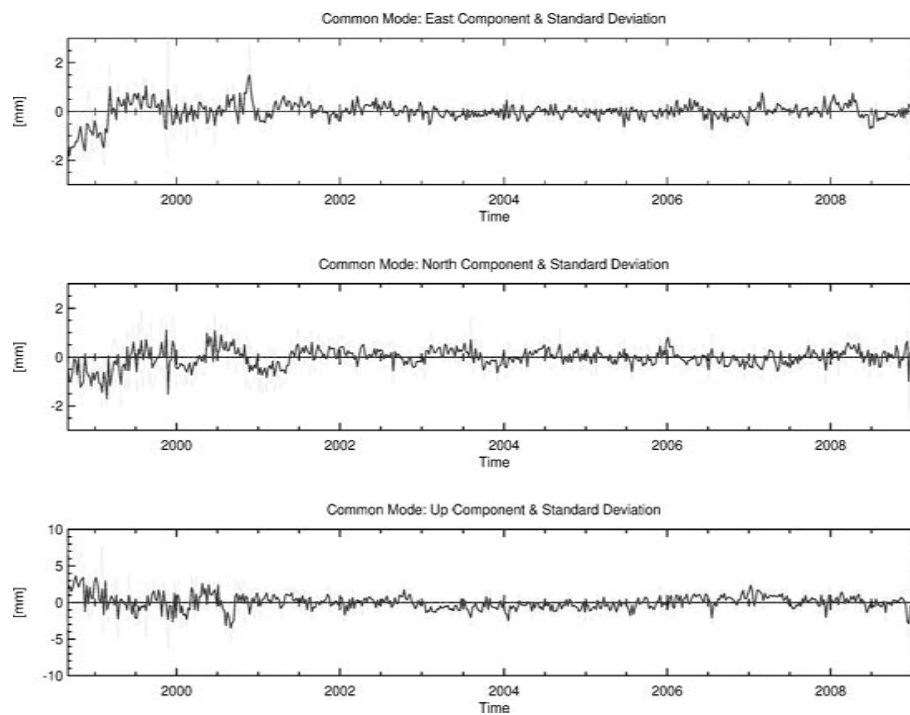


**Figure A.1:** Common Mode Estimation (variant 2): Location and quality criteria: Increase of the quality by eliminating sites with large data gaps and several antenna changes. The green lines represent the one  $\sigma$  interval.

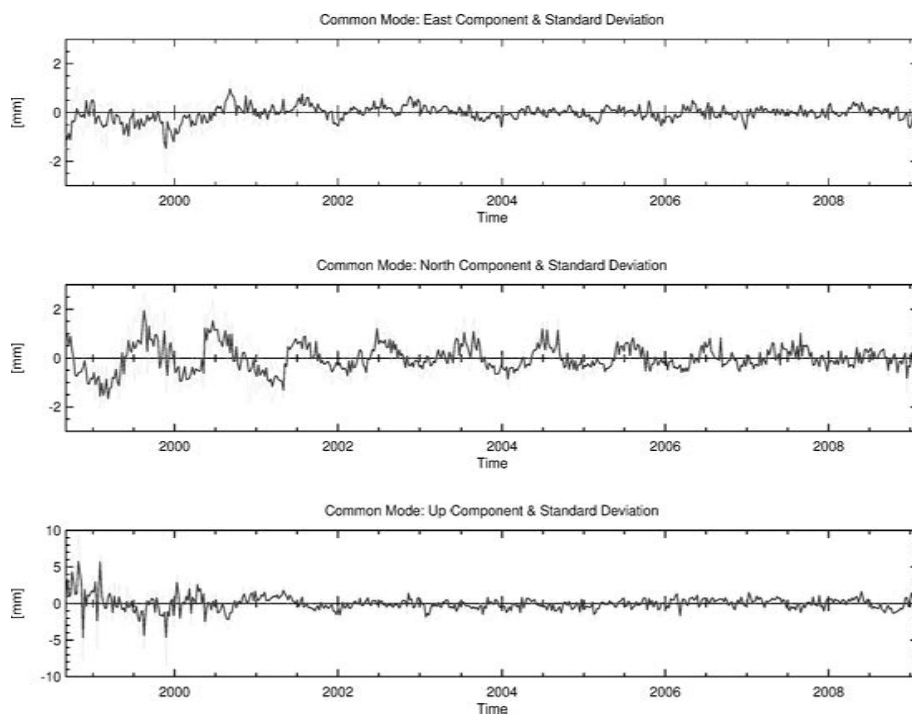


**Figure A.2:** Common Mode Estimation (variant 3): Sites North of the Alps: Detect possible regional effects only affecting the Swiss plateau. The green lines represent the one  $\sigma$  interval.

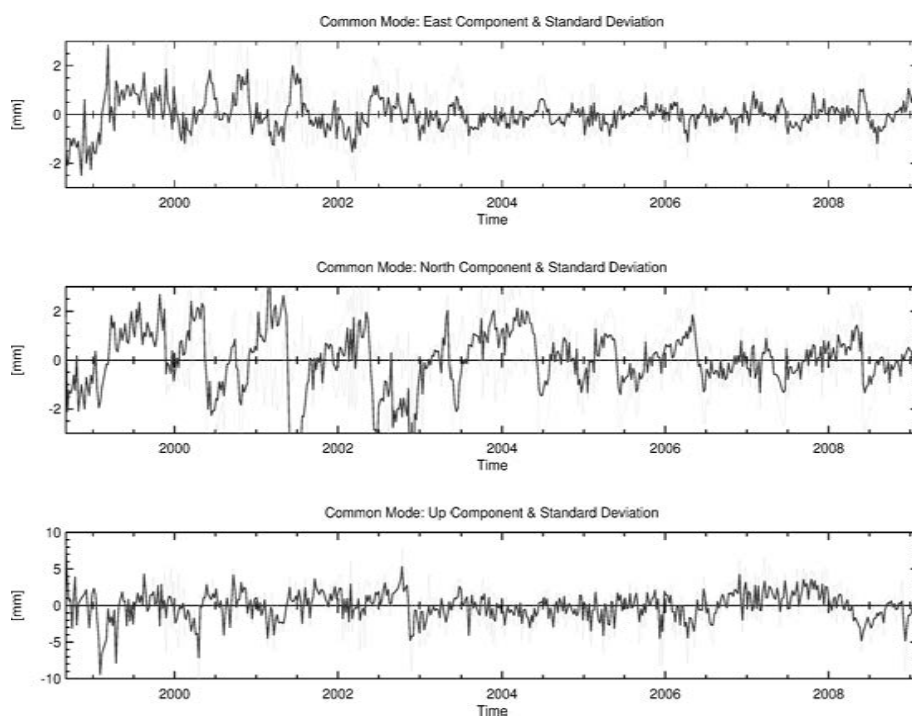


**Figure A.3:** Common Mode Estimation (variant 4): Sites with high altitude (above 1500 meters): Search for altitude depending signals. The green lines represent the one  $\sigma$  interval.

**Table A.1:** Common Mode Estimation (variant 2): Location and quality criteria: Increase the quality by eliminating sites with large data gaps and several antenna changes. RMS of the original velocity estimation ( $\sigma_{O_E}$ ,  $\sigma_{O_N}$ , and  $\sigma_{O_U}$ ), the common mode freed velocity estimation ( $\sigma_{CM_E}$ ,  $\sigma_{CM_N}$ , and  $\sigma_{CM_U}$ ), and the per cent improvement of the precision ( $\%_{CM_E}$ ,  $\%_{CM_N}$ , and  $\%_{CM_U}$ ) are listed in the table.

Station	$\sigma_{O_E}$	$\sigma_{O_N}$	$\sigma_{O_U}$	$\sigma_{CM_E}$	$\sigma_{CM_N}$	$\sigma_{CM_U}$	$\%_{CM_E}$	$\%_{CM_N}$	$\%_{CM_U}$
BSCN	0.58	1.02	1.54	0.55	1.01	1.56	4.6	0.5	-1.2
BOUR	0.82	0.92	2.38	0.76	0.90	2.18	7.6	1.7	8.6
ETHZ	0.82	0.85	1.86	0.82	0.87	2.01	-0.2	-3.0	-7.9
SCHA	0.98	1.06	1.70	0.95	1.09	1.78	3.3	-2.6	-4.9
LUZE	0.63	1.44	2.09	0.64	1.32	1.96	-2.5	8.0	6.2
ZIMM	0.79	0.85	2.54	0.68	0.73	2.19	13.1	13.7	13.8
GENE	0.81	1.22	2.15	0.75	1.18	1.92	7.7	3.4	10.5
HOHT	0.79	1.33	2.84	0.73	1.27	2.60	7.6	4.6	8.3
STAB	0.89	0.80	2.54	0.86	0.78	2.55	3.6	3.1	-0.2
SANB	0.85	1.12	3.97	0.80	1.10	3.64	4.9	1.0	8.4
DAVO	0.75	0.79	2.17	0.65	0.71	2.10	13.7	11.1	3.0

**Table A.2:** Common Mode Estimation (variant 3): Sites North of the Alps: Detect possible regional effects only affecting the Swiss plateau. RMS of the original velocity estimation ( $\sigma_{O_E}, \sigma_{O_N}$ , and  $\sigma_{O_U}$ ), the common mode freed velocity estimation ( $\sigma_{CM_E}, \sigma_{CM_N}$ , and  $\sigma_{CM_U}$ ), and the per cent improvement of the precision ( $\%_{CM_E}, \%_{CM_N}$ , and  $\%_{CM_U}$ ) are listed in the table.

Station	$\sigma_{O_E}$	$\sigma_{O_N}$	$\sigma_{O_U}$	$\sigma_{CM_E}$	$\sigma_{CM_N}$	$\sigma_{CM_U}$	$\%_{CM_E}$	$\%_{CM_N}$	$\%_{CM_U}$
BSCN	0.58	1.02	1.54	0.64	1.26	1.48	-11.8	-24.0	4.3
GENE	0.81	1.22	2.15	0.71	1.07	1.91	12.2	12.2	11.1
EPFL	1.26	3.11	2.04	1.14	2.80	1.88	9.4	9.9	7.9
STCX	1.27	2.15	2.30	1.20	1.90	2.22	5.2	11.6	3.6
PAYE	1.38	1.36	1.56	1.29	1.62	1.39	6.6	-19.5	10.5
NEUC	0.87	1.61	2.21	0.77	1.75	1.96	10.8	-8.8	11.3
BOUR	0.82	0.92	2.38	0.85	0.90	2.35	-3.4	2.1	1.5
FHBB	0.88	0.91	1.78	0.91	0.77	1.75	-2.7	15.2	1.7
FRIC	0.65	1.29	3.00	0.65	1.38	2.89	0.5	-7.5	3.5
SCHA	0.98	1.06	1.70	0.89	1.27	1.60	8.8	-19.8	6.1
KREU	0.67	0.68	1.88	0.68	0.60	1.69	-2.5	11.9	10.0
RAVE	0.64	0.63	1.65	0.63	0.55	1.59	2.3	12.4	3.5
LIND	0.74	0.80	1.97	0.79	0.59	1.89	-7.9	26.4	4.2
PFAN	1.05	1.01	3.36	1.03	0.92	3.11	1.6	9.5	7.5
STGA	1.03	0.85	2.15	0.97	0.67	2.03	5.8	21.0	5.8
UZNA	0.63	1.11	2.29	0.68	0.83	2.13	-8.5	25.4	7.0
KALT	0.62	1.01	1.58	0.61	0.92	1.40	2.6	8.6	11.5
ETHZ	0.82	0.85	1.86	0.79	1.04	1.91	3.7	-23.1	-2.7
LUZE	0.63	1.44	2.09	0.64	1.16	1.99	-2.2	19.3	5.2
HUTT	0.86	0.61	2.04	0.77	0.49	1.93	9.8	19.2	5.4
EXWI	0.45	1.24	1.81	0.39	0.99	1.91	12.4	19.8	-5.4
ZIMM	0.79	0.85	2.54	0.76	0.70	2.27	2.9	18.3	10.6
WAB1	0.75	0.86	1.35	0.74	0.66	1.26	1.1	23.8	7.1
WAB2	0.44	0.82	1.49	0.41	0.63	1.44	5.5	23.6	3.6

**Table A.3:** Common Mode Estimation (variant 4): Sites with high altitude (above 1500 meters): Search for altitude depending signals. RMS of the original velocity estimation ( $\sigma_{O_E}, \sigma_{O_N}$ , and  $\sigma_{O_U}$ ), the common mode freed velocity estimation ( $\sigma_{CM_E}, \sigma_{CM_N}$ , and  $\sigma_{CM_U}$ ), and the per cent improvement of the precision ( $\%_{CM_E}, \%_{CM_N}$ , and  $\%_{CM_U}$ ) are listed in the table.

Station	$\sigma_{O_E}$	$\sigma_{O_N}$	$\sigma_{O_U}$	$\sigma_{CM_E}$	$\sigma_{CM_N}$	$\sigma_{CM_U}$	$\%_{CM_E}$	$\%_{CM_N}$	$\%_{CM_U}$
ANDE	1.33	3.63	2.53	1.10	2.69	2.14	17.6	25.9	15.5
DAVO	0.75	0.79	2.17	0.69	1.22	1.94	8.1	-54.2	10.4
LECH	0.58	0.82	1.69	0.58	1.23	2.00	0.7	-50.4	-18.3
SANB	0.85	1.12	3.97	0.77	1.32	3.03	9.4	-18.1	23.6
WEHO	1.56	0.83	2.19	1.32	0.93	2.20	15.5	-11.2	-0.6
ZERM	1.03	1.14	7.13	0.79	1.15	5.71	22.5	-0.7	19.9

## A.2 Monumentation stability

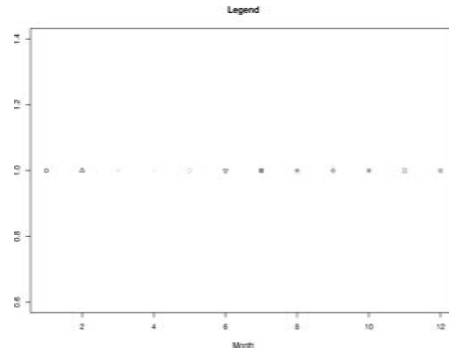


Figure A.4: Monumentation stability: Legend

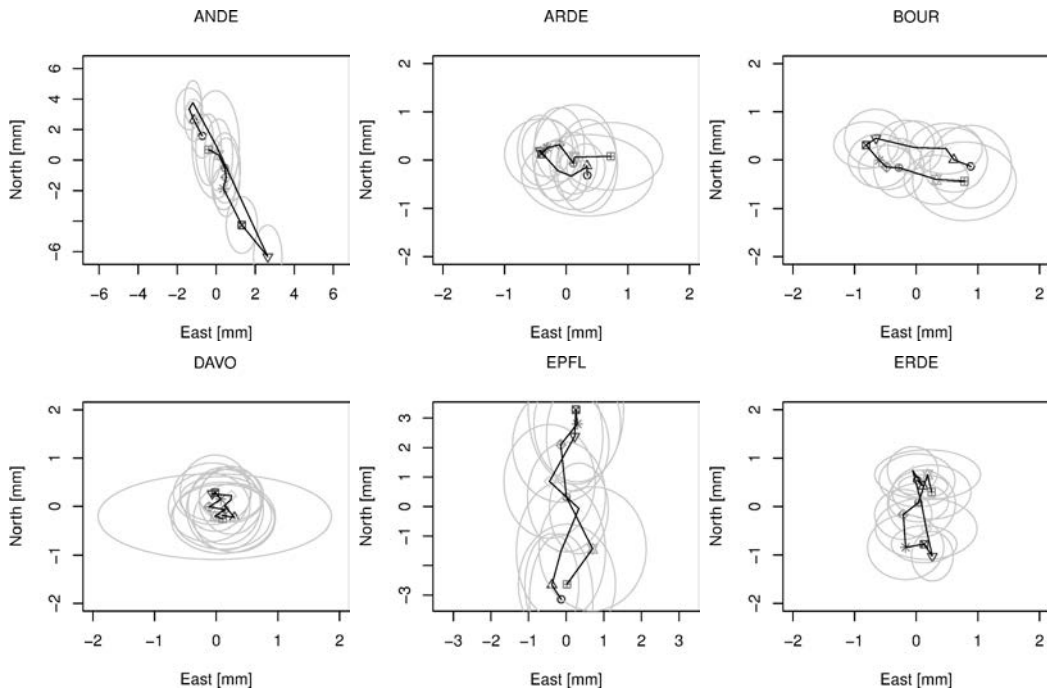


Figure A.5: Monumentation stability: Stacking method for the horizontal component

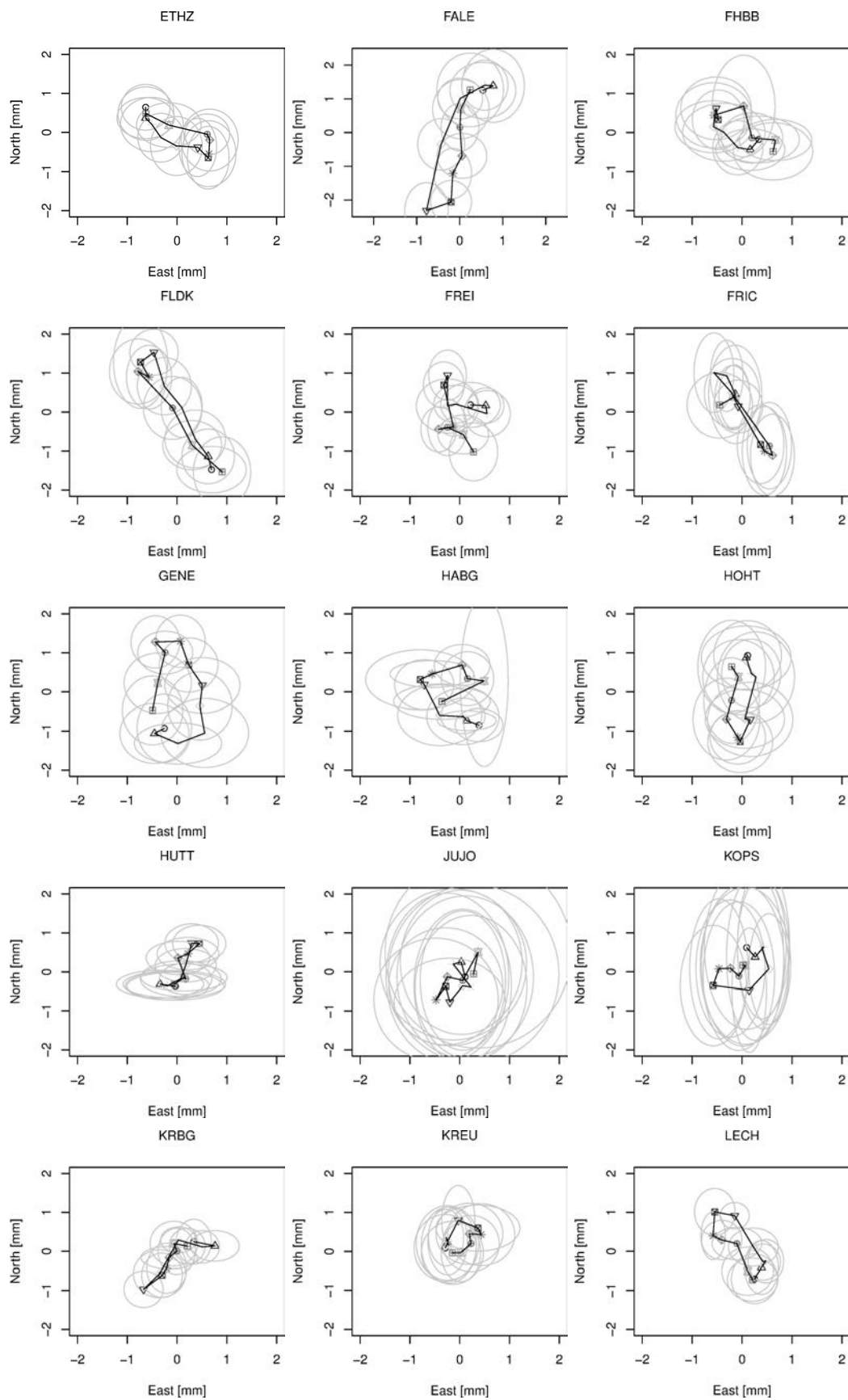


Figure A.6: Monumentation stability: Stacking method for the horizontal component

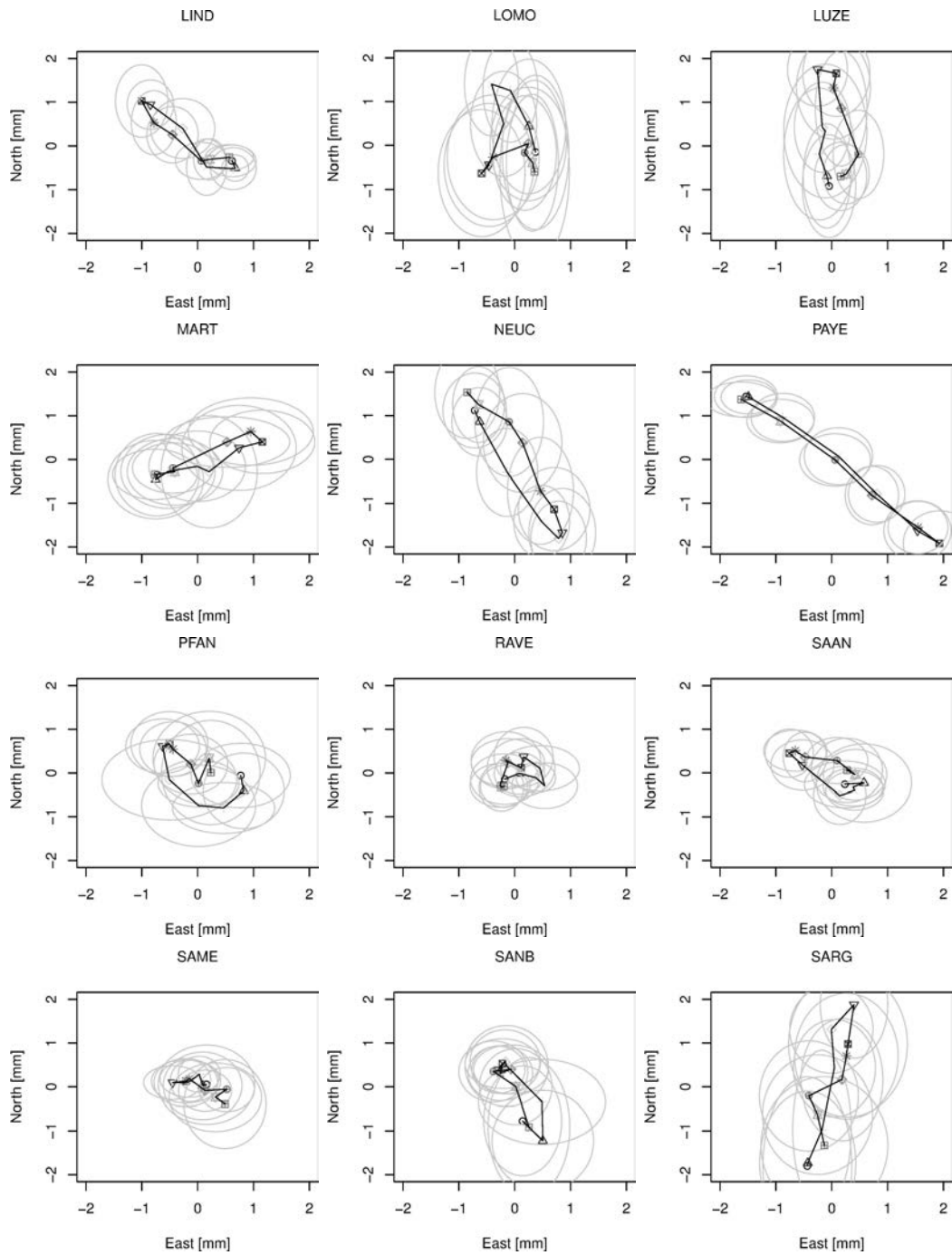


Figure A.7: Monumentation stability: Stacking method for the horizontal component

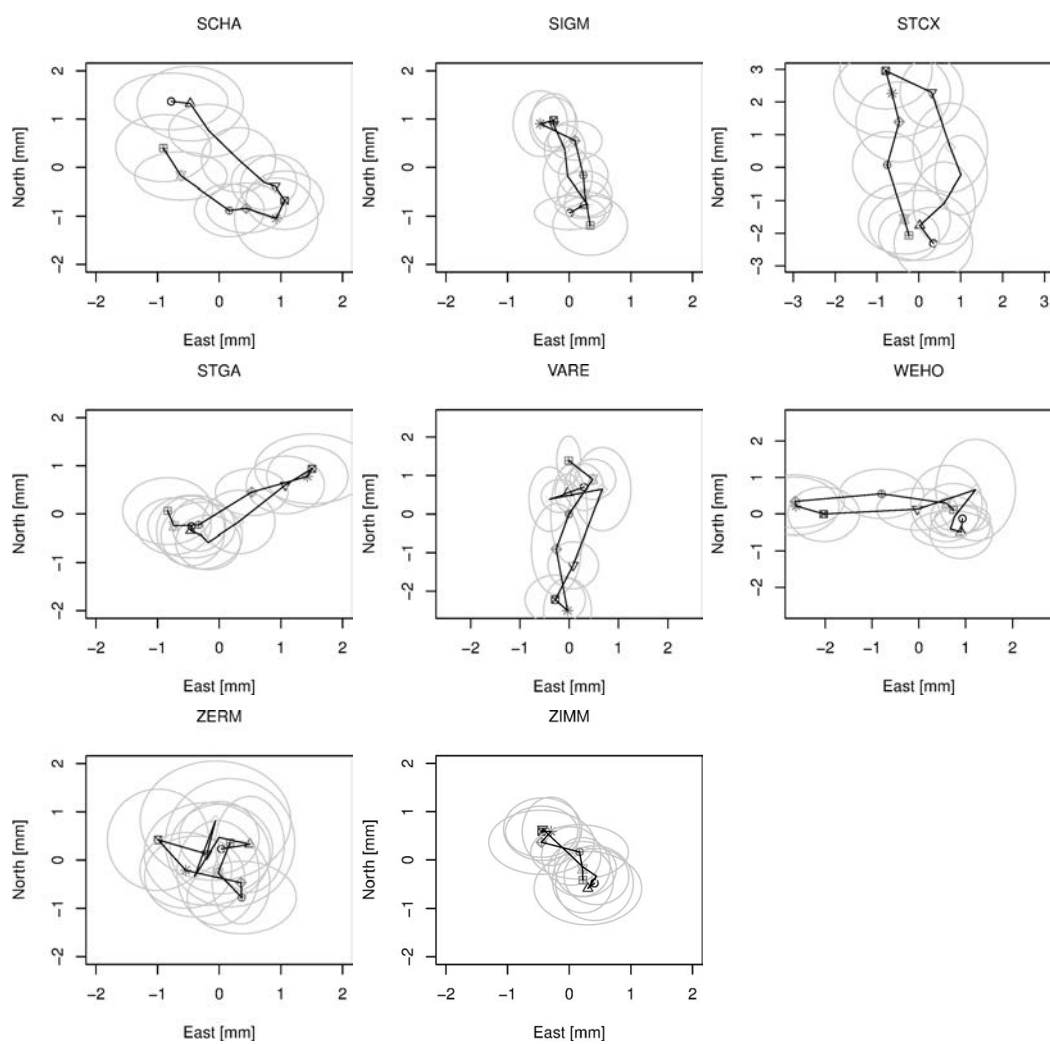


Figure A.8: Monumentation stability: Stacking method for the horizontal component

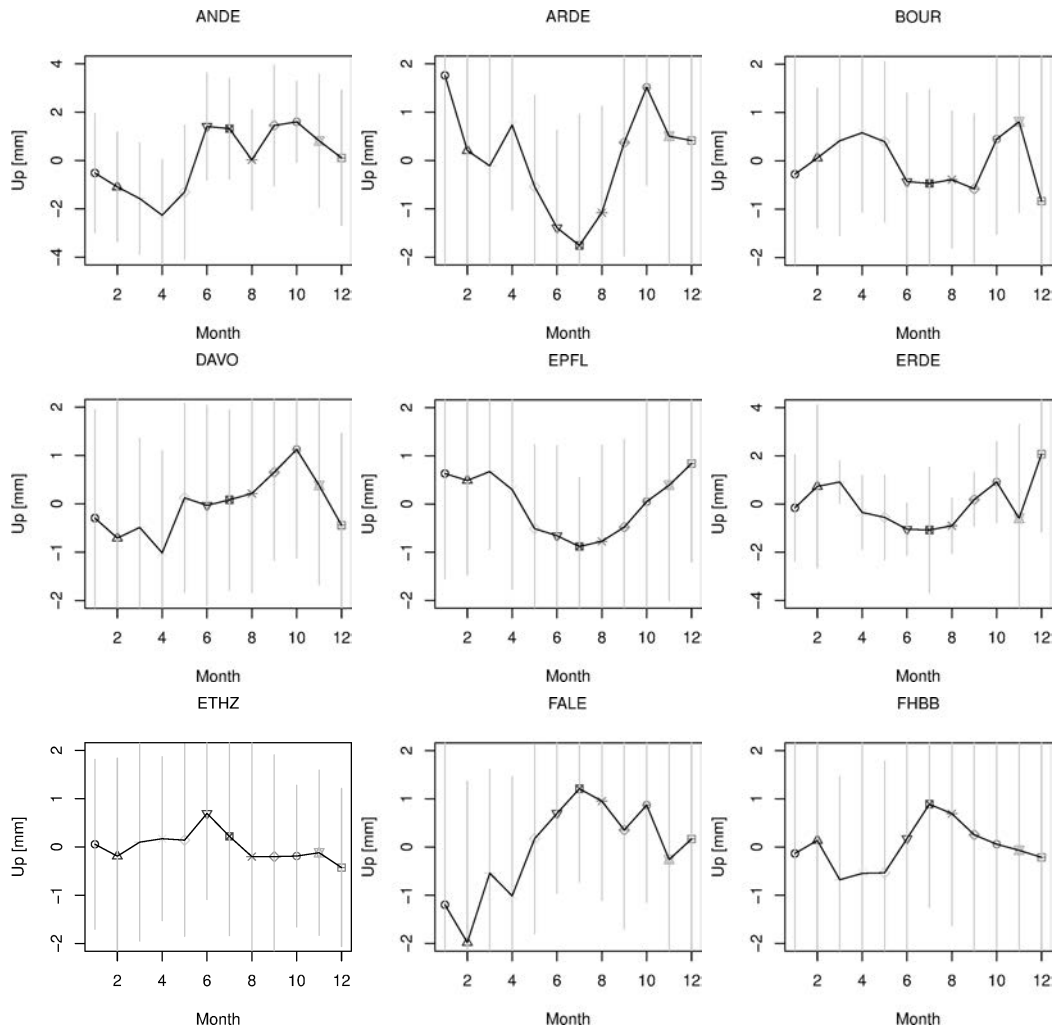


Figure A.9: Monumentation stability: Stacking method for the vertical component

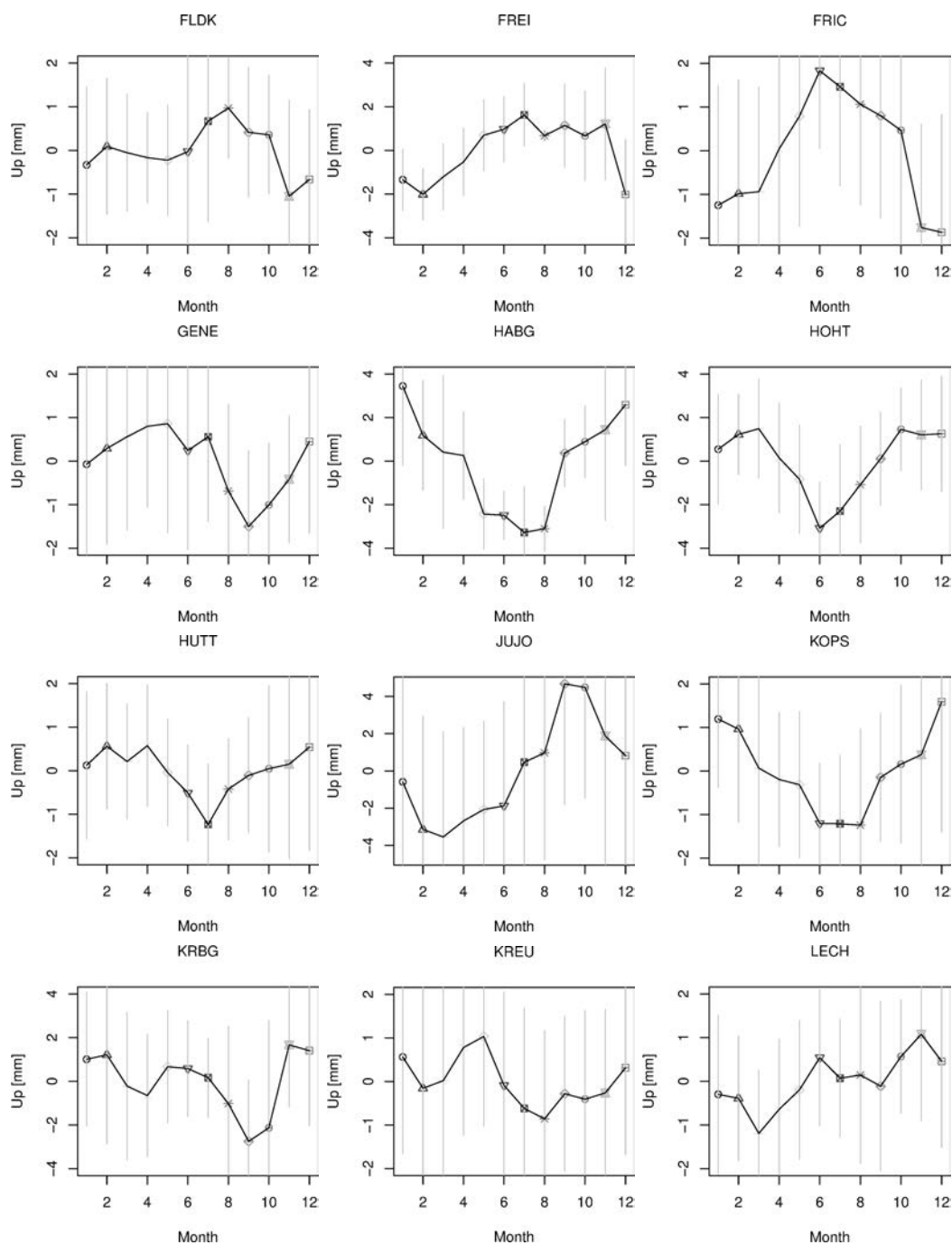


Figure A.10: Monumentation stability: Stacking method for the vertical component

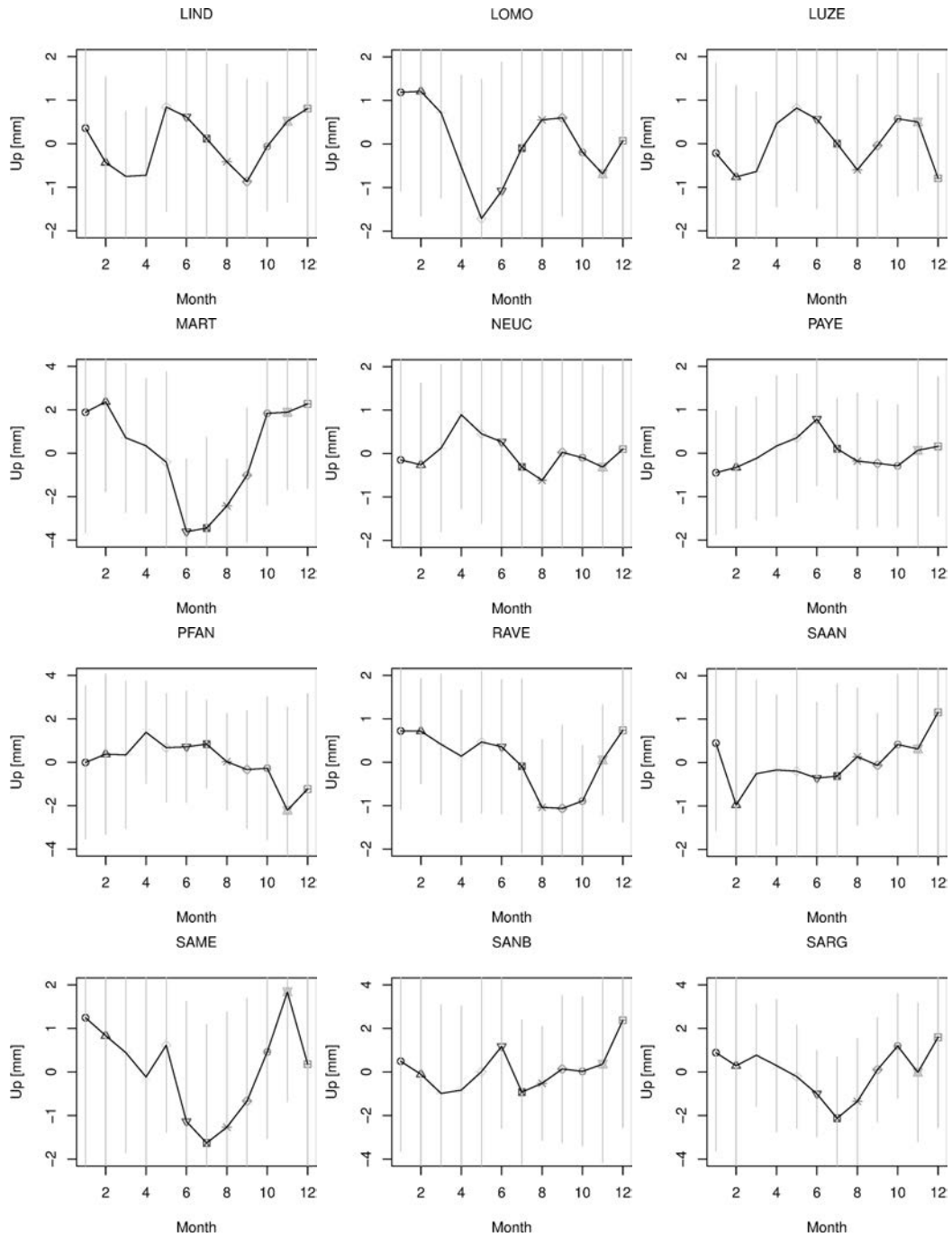


Figure A.11: Monumentation stability: Stacking method for the vertical component

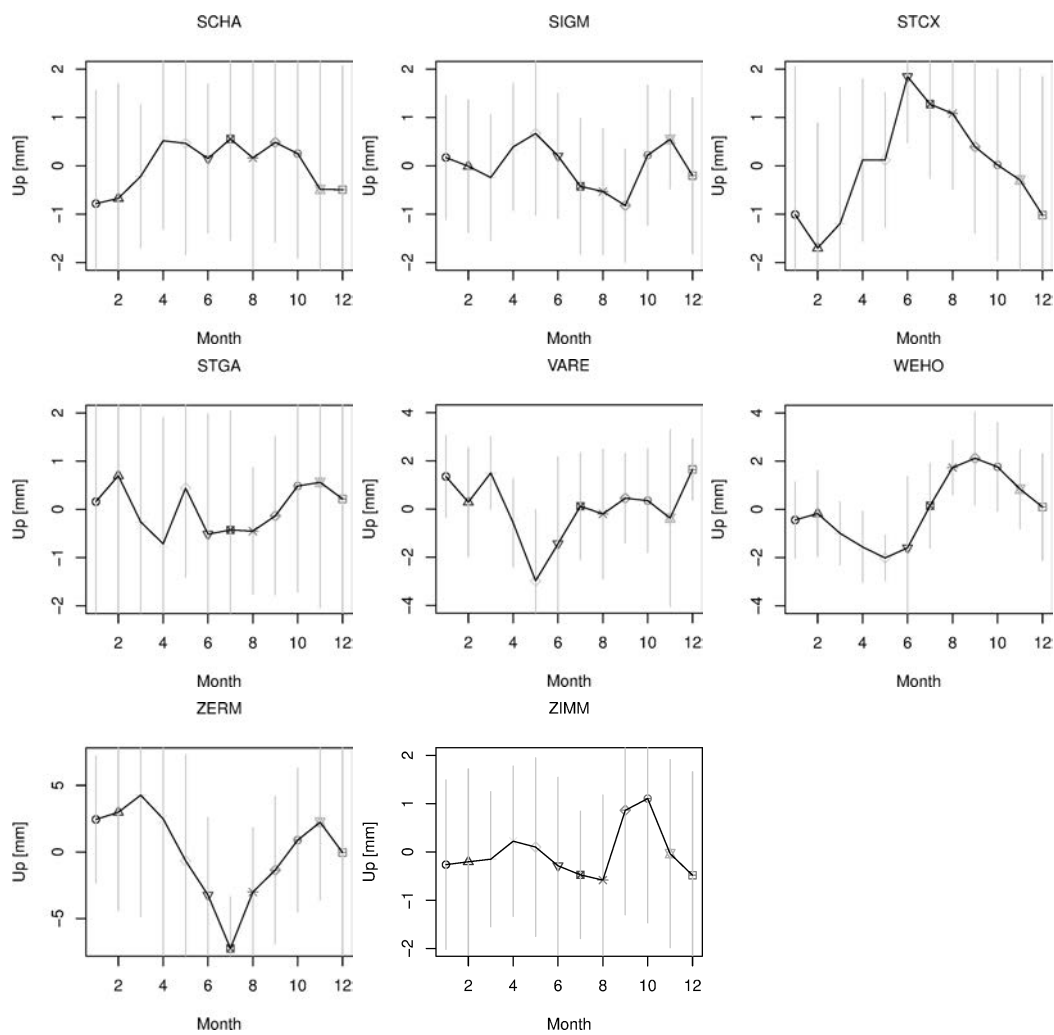


Figure A.12: Monumentation stability: Stacking method for the vertical component